Energy analysis and discretization of nonlinear impedance boundary conditions for the time-domain linearized Euler equations

Florian Monteghetti, Denis Matignon, Estelle Piot

Energy analysis and discretization of nonlinear impedance boundary conditions for the time-domain linearized Euler equations

Florian Monteghetti [a,*], Denis Matignon [b], Estelle Piot [a]

[a] ONERA/DMPE, Université de Toulouse, 31055 Toulouse, France
[b] ISAE-SUPAERO, Université de Toulouse, 31055 Toulouse, France

A B S T R A C T

Time-domain impedance boundary conditions (TDIBCs) can be enforced using the impedance, the admittance, or the scattering operator. This article demonstrates the computational advantage of the last, even for nonlinear TDIBCs, with the linearized Euler equations. This is achieved by a systematic semi-discrete energy analysis of the weak enforcement of a generic nonlinear TDIBC in a discontinuous Galerkin finite element method. In particular, the analysis highlights that the sole definition of a discrete model is not enough to fully define a TDIBC. To support the analysis, an elementary physical nonlinear scattering operator is derived and its computational properties are investigated in an impedance tube. Then, the derivation of time-delayed broadband TDIBCs from physical reflection coefficient models is carried out for single degree of freedom acoustical liners. A high-order discretization of the derived time-local formulation, which consists in composing a set of ordinary differential equations with a transport equation, is applied to two flow ducts.

Keywords:
Time-domain impedance boundary condition
Time-delay systems
Fractional calculus
Diffusive representation
Discontinuous Galerkin

1. Introduction

Across various industries, stringent regulations on sound pollution have led to a growing usage of sound absorbing materials, the design of which requires suitable computational tools. An accurate computation of the acoustic field inside an industrial sound absorbing material is costly by contemporary computing standard, and is thus the realm of specific studies that focus on the material in isolation. Practical computations of sound absorption are typically done by abstracting the geometrical features of the material using a so-called impedance boundary condition (IBC). The computation of sound absorption using an IBC is one aspect of computational aeroacoustics (CAA) [1]. Broadly, this paper deals with the discretization of IBCs in the time domain for the linearized Euler equations. This introduction is split into two parts: Sec. 1.1 covers impedance modeling and its applications, while Sec. 1.2 focuses on the time-domain discretization of IBCs and presents the article objectives and outline.

1.1. Modeling and applications of impedance boundary conditions

Many sound absorbing materials are variations of the acoustical (Helmholtz) resonator. Assumed locally reacting, they can be modeled using a (continuous) single-input single-output time-invariant operator known as the impedance operator

* Corresponding author.
E-mail addresses: florian.monteghetti@onera.fr (F. Monteghetti), denis.matignon@isae.fr (D. Matignon), estelle.piot@onera.fr (E. Piot).

https://doi.org/10.1016/j.jcp.2018.08.037

[2, § 6.3] [3, Chap. 10]. At low incident sound pressure level (SPL), the impedance is linear and thus reduces to a time-domain convolution [4, § III.3]; it is a hereditary (i.e. non time-local) operator whose kernel exhibits a long memory behavior linked to viscous and thermal effects within both the neck and the cavity. (See [5, § III] and references therein for common linear models.) Above a SPL threshold, a turbulent dissipation mechanism that occurs at the resonator neck, known as vortex shedding, results in the addition of a nonlinearity [6, § 4] [7, § I] [8, § 2] [9, § 5]. The influence of a subsonic grazing flow can be modeled through an additional parametric dependence that does not change the mathematical nature of the impedance operator [10, § 3] [11, § 7].

The effect of a locally reacting absorbing material on the sound field is accurately described, after a homogenization distance [12], by using its impedance operator as a boundary condition. The effectiveness of this modeling and the advent of acoustically treated jet engines has led to IBCs becoming a staple part of aeroacoustics [13, Chaps. 13 & 14]. Early works focused on the prediction of sound absorption in a duct with flow: Cremer [14] derived an approximation of the optimal impedance and Pridmore-Brown [15] established his celebrated equation, widely used to compute duct modes. The identification of unstable surface modes by Tester [16] lead to a wealth of investigations focused on the hydrodynamic stability of a base flow with an IBC [17]. Inverse methodologies have been developed to identify the IBC and provide an alternative to more intrusive measurement techniques [18]. In all of these studies, the IBC is linear and the Cauchy problem is formulated in the frequency domain. Although less popular than their time-harmonic counterparts, time-domain IBCs (TDIBCs) have been used in wave propagation problems including duct aeroacoustics [19–22], room acoustics [23], as well as outdoor sound propagation [24]. Richter et al. [25,26] and Troian et al. [27] identified an IBC in the time domain. Gabard & Brambley [28] used a time-domain formulation to investigate the (in)stability of the Ingard–Myers boundary condition.

The use of a time-domain IBC may merely be more convenient than a time-harmonic one, for instance when a broadband source is considered. However, it is indispensable when the harmonic problem *cannot* be formulated, such as in the presence of time-dependent domains, moving sources, or nonlinearities. Typically, the nonlinearity comes from the impedance operator, as mentioned above, or from the considered partial differential equation (PDE). Nonlinear PDEs are of particular interest when hydrodynamic phenomena cannot be neglected, such as close to a supersonic fan tip where shocks occur [29, § 5.3], or for flow control. Scalo et al. [30] and Olivetti et al. [31] performed a Navier–Stokes simulation (large eddy simulation and direct numerical simulation, respectively) with a linear TDIBC to investigate the interaction between a turbulent boundary layer and an impedance wall.

It is worth noting that IBCs have other uses and denominations. In simulations of combustion chambers, IBCs are used to truncate a part of the chamber [32,33] or model injectors [32,34] for instance. In mathematical control, TDIBCs (also known as Dirichlet to Neumann maps) are commonly used to stabilize the wave equation since they modify the underlying semigroup generator and can yield asymptotic or even exponential stability. Both finite-dimensional [35] and infinite-dimensional TDIBCs, involving for example fractional derivative [36] and time delay [37], have been studied. Surface or generalized IBCs [38] are employed in electromagnetism to model non-perfect electric conductors. The first and most widely used model is that of Leontovich, which is a fractional operator identical to that encountered in the acoustic impedance of perforated plates [5]. See [39,40] for two applications in the time domain.

1.2. Time-domain discretization of impedance boundary conditions

A *discrete* TDIBC consists of three components. First, the discrete impedance model, i.e. the finite-dimensional operator (in the sense of systems theory [41,42]) that one wishes to apply at the boundary. Second, the numerical algorithm used to evaluate the said operator; in the case of linear continuous time-invariant operators (i.e. of linear TDIBCs) this amounts to computing a time-domain convolution. Practically these first two elements go hand in hand since the expression of the convolution kernel dictates how the convolution can be efficiently computed. The third and last component is the (semi-)discrete formulation, i.e. how the TDIBC is enforced at the (semi-)discrete level.

The first two components are well-documented for linear TDIBCs. First, broadband discrete impedance models can be built from the so-called oscillatory-diffusive representation of physical models [5]. Second, a convenient way to compute a causal convolution is to recast it into a set of ordinary differential equations (ODEs) (or, in the sense of systems theory, to *realize* the corresponding LTI operator [41, § 17] [42, § 1.2]), a method sometimes named “auxiliary differential equations” [20,43], “canonical form implementation” [21,22], or “state-space model” [32] in the acoustics or fluid dynamics literature. In this way, the computation of a (in)finite-dimensional hereditary operator is reduced to the integration of a (in)finite set of time-local differential equations, which can be done with arbitrary accuracy. If the impedance operator models a reflection phenomenon (e.g. a wave reflection in the cavity of a Helmholtz resonator), its realization involves not only ODEs but also *time-delayed* ODEs [5]. Alternatively, when a realization of the impedance operator is beyond reach, more general algorithms can be used, such as convolution quadrature or multistep methods [44,40,45]. The key feature of these methods is that they only require the knowledge of the Laplace transform of the convolution kernel, which is always known in the case of linear impedance models (impedance modeling, be it theoretical or empirical, is often carried out in the frequency domain).

The third component of a TDIBC is seldom discussed. For instance, there does not seem to be a consensus on whether a TDIBC should be based on the impedance z [19,46,20,28,31], the admittance y [21,22], or the reflection coefficient β [47,30,32]. This topic has been mentioned by Gabard & Brambley [28] who warned that some instabilities reported in the literature may be due to an unsuitable implementation and showed the benefit of a characteristic-based implementation in their study, which is echoed in works that focus on large eddy simulations and direct numerical simulations [30,32,34,33].

Another scarcely mentioned aspect is the impact of the TDIBC on the maximum admissible time step. Although this aspect is of secondary concern for stability studies, it is of crucial importance for large-scale applications like those that involve hydrodynamics or for inverse methods that need to explore the impedance parameter space. To the best of the authors' knowledge, the only known result is that for a proportional impedance (i.e. $z(t) \propto \delta(t)$), using the reflection coefficient yields a CFL stability condition independent of the impedance coefficient [48, § 3.3] [49, 2.3].

The objective of this paper is to contribute to addressing these gaps by establishing the computational advantage of the reflection coefficient, even for nonlinear TDIBCs, with the linearized Euler equations. This is achieved by a systematic investigation of the weak enforcement of a generic nonlinear TDIBC in a discontinuous Galerkin finite element method. To support the analysis, an elementary physical nonlinear scattering operator is derived and its computational properties are investigated in an impedance tube. Then, for application to two flow ducts, the derivation of broadband TDIBCs *from* physical reflection coefficient models is carried out for single degree of freedom acoustical liners. The derived formulation is purely time-local and consists in composing a set of ODEs with a transport equation.

This paper is organized as follows. Sec. 2 gathers preliminaries including a rigorous statement of impedance admissibility conditions. Two of three components of a TDIBC, namely the discrete model and the time discretization algorithm, are covered in Sec. 3, which derives both linear and nonlinear discrete models from the analysis of physical impedance models. The third component, namely the (semi-)discrete formulation, is addressed *independently* in Sec. 4 with an investigation of the weak enforcement of a generic nonlinear impedance boundary condition within a discontinuous Galerkin finite element method. The last two sections gather numerical validations and applications of the presented analysis. Sec. 5 validates the proposed linear and nonlinear TDIBCs by comparison with the impedance tube analytical solution. Sec. 6 presents an application to two flow ducts.

2. Preliminaries on the continuous formulation

The purpose of this section is to introduce the physical problem considered in this paper, as well as to gather definitions and notations for later use (such as the analysis of Sec. 4). The linearized Euler equations are briefly recalled in Sec. 2.1. Sec. 2.2 gives the three equivalent formulations of an IBC and rigorously states the admissibility conditions. Lastly, Sec. 2.3 presents the assumption made on the base flow and discusses its mathematical and physical implications.

2.1. Linearized Euler equations

In this work the hydrodynamic field is split between a steady base flow and an unsteady perturbation. The perturbations of pressure p, velocity $\boldsymbol{u}$, and density ρ are governed by the homentropic linearized Euler equations (LEEs), defined on $(0,\infty)\times\Omega$ with $\Omega\subset\mathbb{R}^n$ a bounded open subset,

$$\begin{cases} \partial_t \boldsymbol{u} + (\boldsymbol{u_0}\cdot\nabla)\boldsymbol{u} + z_0^{-1}c_0\nabla p + (\boldsymbol{u}\cdot\nabla)\boldsymbol{u_0} + z_0^{-1}c_0^{-1}p(\boldsymbol{u_0}\cdot\nabla)\boldsymbol{u_0} = 0 \\ \partial_t p + (\boldsymbol{u_0}\cdot\nabla)p + z_0c_0\nabla\cdot\boldsymbol{u} + \gamma p\nabla\cdot\boldsymbol{u_0} = 0 \\ p = c_0^2\rho. \end{cases} \tag{1}$$

The specific heat ratio is denoted $\gamma > 1$. Quantities related to the base flow are designated by the subscript "0": $\boldsymbol{u_0}$ is the base flow velocity, ρ_0 the base flow density, c_0 the speed of sound, and $z_0 := \rho_0 c_0$ the characteristic impedance of the propagation medium. All quantities are dimensional. Column vectors are denoted in bold and the symbol $(\boldsymbol{u}\cdot\nabla)$ denotes the convective derivative defined as $(\boldsymbol{u}\cdot\nabla)f := \sum_i u_i\partial_i f$ and $(\boldsymbol{u}\cdot\nabla)\boldsymbol{f} := \nabla\boldsymbol{f}\cdot\boldsymbol{u} = (\sum_j u_j\partial_j f_i)_i$ when applied to scalar-valued and vector-valued functions, respectively. The symbol ":=" is used to denote a definition. The LEEs (1) entail hypotheses on both the base flow and the perturbations. The base flow is a perfect gas, so that $c_0^2 = \gamma r T_0 = \gamma p_0/\rho_0$, and can solve either the steady Euler or Navier–Stokes equations. The perturbations are "small", inviscid, and homentropic. The rather strong homentropicity assumption enables to replace the energy equation by the algebraic relation $p = c_0^2\rho$ and implies that c_0 must be constant in Ω. As a result, the LEEs (1) do not include an entropy mode, but only hydrodynamic and acoustic ones. In spite of its simplicity, this model is commonly used in duct aeroacoustics, see Sec. 6. For the detailed derivation of the LEEs and additional physical insights, the reader is referred to [25, Chap. 2] and references therein.

2.2. Formulations and admissibility conditions of impedance boundary conditions

On a subset Γ_z of the boundary $\Gamma := \partial\Omega$, an IBC is applied, defined as

$$p(t,\boldsymbol{x}) = \mathcal{Z}[\boldsymbol{u}(\cdot,\boldsymbol{x})\cdot\boldsymbol{n}(\boldsymbol{x})](t) \quad (t\in(0,\infty),\ \boldsymbol{x}\in\Gamma_z), \tag{2}$$

where $\boldsymbol{n}$ is the outward unit normal and $\mathcal{Z}$ is the (single-input single-output) impedance operator. If the impedance operator is linear continuous time-invariant (LTI), the IBC (2) reduces to

$$p(t,\boldsymbol{x}) = [z\star\boldsymbol{u}(\cdot,\boldsymbol{x})\cdot\boldsymbol{n}(\boldsymbol{x})](t), \tag{3}$$

where z is the impedance kernel and "$\star$" denotes the time-domain convolution of distributions [4, Chap. III]. Since the LEEs (1) are linear, the LTI IBC (3) can also be formulated in the Laplace domain, provided that z is causal, as

$$\hat{p}(s,\boldsymbol{x}) = \hat{z}(s)\hat{\boldsymbol{u}}(s,\boldsymbol{x})\cdot\boldsymbol{n}(\boldsymbol{x}) \quad (\Re(s) > c), \tag{4}$$

where the Laplace transform is defined as $\hat{f}(s) = \int_0^\infty f(t)e^{-st}\,\mathrm{d}t$ for a locally integrable function with finite exponential growth, i.e. $f \in L^1_{\mathrm{loc}}([0,\infty))$ with $|f(t)| \le Me^{ct}$. If f is a causal distribution, as encountered with physical impedance models, the distributional extension $\hat{f}(s) = \langle f, e^{-st}\rangle$ is employed [4, Chap. 6] [50, Chap. 2]. As long as the problem is linear, (3) and (4) are equivalent. The Laplace formulation is particularly useful for stability studies (using a Briggs–Bers analysis for instance) or when deriving representations of physical impedance models, as is done in Sec. 3.2. Formally $s = \mathrm{j}\omega$ (with $\mathrm{j}^2 = -1$) yields the Fourier transform but such a mere formal substitution is error-prone, especially when dealing with admissibility conditions, which justifies the present use of the Laplace transform; a discussion on this topic is provided in Appendix A. In the remainder of this paper, "impedance" can designate the single-input single-output operator $\mathcal{Z}$, the convolution kernel z, or its Laplace transform $\hat{z}$. The impedance can have a spatial dependency (i.e. $\mathcal{Z}(\boldsymbol{x},\cdot)$, $z(\boldsymbol{x},t)$, or $\hat{z}(\boldsymbol{x},s)$), although it is not explicitly written for the sake of clarity. In this study, the IBC (2) is meant to model a passive sound absorbing material so that it obeys the admissibility conditions given below.

Definition 1 *(Admissibility conditions).* Let $\mathcal{Z}$ be a single-input single-output operator. It is said to be an *admissible* impedance operator if it enjoys the following properties: causality; reality (real-valued inputs are mapped to real-valued outputs); passivity, i.e. for every smooth and compactly supported input $u \in \mathcal{C}_0^\infty(\mathbb{R})$ and for every time instant $t > 0$,

$$\Re\left(\int_{-\infty}^{t} \overline{\mathcal{Z}(u)(\tau)}u(\tau)\,\mathrm{d}\tau\right) \ge 0, \tag{5}$$

where the overline denotes the complex conjugate.

Physically, the left-hand side of (5) is the energy supplied to the system over $(-\infty, t)$. The passivity condition (5), which applies to every passive system encountered in physics, means that the system does not produce energy [51, p. 301] [52, p. 12]. If $\mathcal{Z}$ is LTI, then it is interesting to note that this definition could be restricted to reality and passivity. Indeed, for real LTI systems, passivity *implies* causality [51, Lemma 10.3] [50, Note 8]. A consequence of this result is that a real anticausal LTI system cannot be passive: intuitively, for such a system the supplied energy over $(-\infty, t)$ can be made arbitrarily negative by modifying the input u in the future. A key fact in practice is that the admissibility of an LTI impedance can be readily read on its Laplace transform $\hat{z}$, as summarized in Proposition 3 below, which could be interpreted as a rigorous statement of [46, Thm. 1].

Definition 2 *(Positive-real function).* Let $\mathbb{C}_0^+ := \{s \in \mathbb{C} \,|\, \Re(s) > 0\}$ be the open right half-plane. A function $f : \mathbb{C}_0^+ \to \mathbb{C}$ is *positive-real* if f is analytic in $\mathbb{C}_0^+$, $f(s) \in \mathbb{R}$ for $s \in (0,\infty)$, and $\Re[f(s)] \ge 0$ for $\Re(s) > 0$.

Proposition 3. *An LTI operator $\mathcal{Z}$ is an admissible impedance operator if and only if its Laplace transform $\hat{z}(s)$ is a positive-real function.*

Proof. This is a standard fact of Systems Theory. See [52, § 2.11] for the case where the kernel $z \in L^1(\mathbb{R})$ is a function and [50, § 3.5] for the general case where $z \in \mathcal{D}'_+(\mathbb{R})$ is a causal distribution. □

Remark 4. The growth at infinity of positive-real functions is at most polynomial. More specifically, from the integral representation of positive-real functions [50, Eq. (3.21)], it follows that for $\Re(s) \ge a > 0$, $|\hat{z}(s)| \le C(a)P(|s|)$ where P is a second degree polynomial.

Example 5. Let us give some practical examples of admissible impedance models, encountered in Sec. 3: the multiplication $z = \delta$ ($\hat{z}(s) = 1$) with δ denoting the Dirac distribution; the derivative $z = \delta'$ ($\hat{z}(s) = s$); the half-order fractional integration $z(t) = {}^{H(t)}/_{\sqrt{\pi t}}$ where $H(t)$ is the Heaviside function ($\hat{z}(s) = {}^1/_{\sqrt{s}}$); the fractional derivative $z(t) = {}^{H(t)}/_{\sqrt{\pi t}} \star \delta'(t)$ ($\hat{z}(s) = \sqrt{s}$); the time-delay system $z(t) = a\delta(t) + b\delta(t-\tau)$ with $a \ge b \ge 0$ and $\tau \ge 0$ ($\hat{z}(s) = a + be^{-s\tau}$). The following impedance kernels are *not* admissible: $\hat{z}(s) = \sqrt{s/\mathrm{j}}$, which fails the reality condition $\hat{z}(s) \in \mathbb{R}$ for $s \in (0,\infty)$; $\hat{z}(s) = a + be^{-s\tau}$ with $a < b$ and $\tau \ge 0$, which is not passive; $z(t) = \delta(t+\tau)$ with $\tau \ge 0$ ($\hat{z}(s) = e^{s\tau}$), which is not causal; $z(t) = e^t H(t)$ ($\hat{z}(s) = (s-1)^{-1}$), which is not passive ($\hat{z}(s)$ is not analytic in $\mathbb{C}_0^+$ since it admits 1 as a pole).

As mentioned in the introduction and covered further below, it can be beneficial to consider other forms of the IBC (2). When possible, it may be written using the admittance operator $\mathcal{Y}$ as

$$\boldsymbol{u}(t,\boldsymbol{x})\cdot\boldsymbol{n}(\boldsymbol{x}) = \mathcal{Y}[p(\cdot,\boldsymbol{x})](t). \tag{6}$$

If the impedance operator $\mathcal{Z}$ is LTI and admissible, then the admittance operator $\mathcal{Y}$ exists, is unique, and is also LTI and admissible so that (6) reduces to

$$\boldsymbol{u}(t,\boldsymbol{x})\cdot\boldsymbol{n}(\boldsymbol{x}) = [y \star p(\cdot,\boldsymbol{x})](t), \tag{7}$$

where the admittance kernel y is the convolution inverse of z, i.e. $y \star z = \delta$ or $\hat{y}(s)\hat{z}(s) = 1$. The admissibility conditions on $\mathcal{Y}$ are strictly identical to that of $\mathcal{Z}$, so that Proposition 3 with "admittance" substituted for "impedance" holds true.

The third and last considered formulation of the IBC (2) is the so-called scattering formulation

$$\tilde{p}(t,\boldsymbol{x}) - \boldsymbol{u}(t,\boldsymbol{x})\cdot\boldsymbol{n}(\boldsymbol{x}) = \mathcal{B}[\tilde{p}(\cdot,\boldsymbol{x}) + \boldsymbol{u}(\cdot,\boldsymbol{x})\cdot\boldsymbol{n}(\boldsymbol{x})](t), \tag{8}$$

where $\tilde{p} := z_0^{-1} p$ and $\mathcal{B}$ is known as the scattering operator. The expression (8) has an elementary physical interpretation based on the characteristics of the LEEs (1): the incident wave $\tilde{p} + \boldsymbol{u}\cdot\boldsymbol{n}$ is reflected back as $\tilde{p} - \boldsymbol{u}\cdot\boldsymbol{n}$. Admissibility conditions can also be formulated on the scattering operator, see the definition below.

Definition 6 *(Admissibility conditions).* Let $\mathcal{B}$ be a single-input single-output operator. It is said to be an *admissible* scattering operator if it enjoys the following properties: causality; reality (real-valued inputs are mapped to real-valued outputs); passivity, i.e. for every smooth and compactly supported input $v \in \mathcal{C}_0^\infty(\mathbb{R})$ and for every time instant $t > 0$,

$$\int_{-\infty}^{t} |\mathcal{B}(v)(\tau)|^2 \,\mathrm{d}\tau \leq \int_{-\infty}^{t} |v(\tau)|^2 \,\mathrm{d}\tau. \tag{9}$$

The equivalence between the passivity properties (5) and (9) follows from the identity $4\tilde{p}u = (\tilde{p}+u)^2 - (\tilde{p}-u)^2$. The potential computational benefit of $\mathcal{B}$ over $\mathcal{Z}$ and $\mathcal{Y}$ can be guessed by comparing (5) and (9) and is demonstrated on an elementary example in Sec. 5. When possible, the scattering operator $\mathcal{B}$ can be deduced from the (nonlinear) impedance operator $\mathcal{Z}$ through

$$\mathcal{B} := (z_0^{-1}\mathcal{Z} - \mathcal{I}) \circ (z_0^{-1}\mathcal{Z} + \mathcal{I})^{-1} = \mathcal{I} - 2(z_0^{-1}\mathcal{Z} + \mathcal{I})^{-1}, \tag{10}$$

where $\mathcal{I}$ denotes the identity operator. An example of physical nonlinear scattering operator derived using this expression is given in Sec. 3.1. If $\mathcal{Z}$ is LTI and admissible, then $\mathcal{B}$ can be uniquely defined and is an admissible LTI scattering operator with kernel β, whose Laplace transform $\hat{\beta}(s)$, known as the reflection coefficient in acoustics, is given by

$$\hat{\beta}(s) = \frac{z_0^{-1}\hat{z}(s) - 1}{z_0^{-1}\hat{z}(s) + 1} = 1 - \frac{2}{z_0^{-1}\hat{z}(s) + 1} \quad (\Re(s) > 0). \tag{11}$$

Intuitively, $z = \infty$, $y = 0$, and $\mathcal{B} = \mathcal{I}$ (kernel $\beta = \delta$) yield a hard wall while $z = 0$, $y = \infty$, and $\mathcal{B} = -\mathcal{I}$ (kernel $\beta = -\delta$) yield a pressure-release wall. Similarly to the impedance case, the admissibility of an LTI scattering operator can be conveniently characterized using its Laplace transform. The result, given in Proposition 8, is identical to that of Proposition 3 with "bounded-real" substituted for "positive-real".

Definition 7 *(Bounded-real function).* A function $f : \mathbb{C}_0^+ \to \mathbb{C}$ is *bounded-real* if f is analytic in $\mathbb{C}_0^+$, $f(s) \in \mathbb{R}$ for $s \in (0, \infty)$, and $|f(s)| \leq 1$ for $\Re(s) > 0$.

Proposition 8. *An LTI operator $\mathcal{B}$ is an admissible scattering operator if and only if its Laplace transform $\hat{\beta}(s)$ is a bounded-real function.*

Proof. See the references quoted in the proof of Proposition 3. Note that the conformal map from $\{s \in \mathbb{C} \,|\, \Re(s) > 0\}$ onto $\{s \in \mathbb{C} \,|\, |s| < 1\}$ defined by $s \mapsto {}^{(s-1)}/_{(s+1)}$ transforms a positive-real function into a bounded-real one. □

Remark 9 *(IBC for wave equation).* Without base flow, i.e. $\boldsymbol{u_0} = \boldsymbol{0}$, both p and $\boldsymbol{u}$ obey the wave equation, and the IBC (2) reduces to $\partial_t p = Z(-c_0 z_0^{-1}\partial_n p)$. Hence, a hard (resp. pressure-release) wall corresponds to a Neumann (resp. Dirichlet) boundary condition on p, while a proportional impedance $Z \propto I$ yields a Robin boundary condition. Studies focused on the wave equation typically use the linear admittance formulation $\partial_n p = -c_0^{-1} z_0\, y \star \partial_t p$ [37, Eq. 1.1] [36, Eqs. 5, 6] [35, Eq. 2] [45, Eq. 1].

2.3. Assumption on the base flow and well-posedness

In preparation for the analysis of Sec. 4, it is convenient to rewrite the LEEs (1) as a Friedrichs-symmetric system

$$\partial_t \boldsymbol{v}(t,\boldsymbol{x}) + \mathcal{A}\boldsymbol{v}(t,\boldsymbol{x}) = 0 \quad (t \in (0,\infty),\ \boldsymbol{x} \in \Omega), \tag{12}$$

where $\boldsymbol{v} := (\boldsymbol{u}^\intercal, \tilde{p})^\intercal \in \mathbb{R}^{n+1}$ is the perturbation vector, homogeneous to a velocity, and the spatial operator $\mathcal{A}$ is defined as $\mathcal{A}\boldsymbol{v} := A(\nabla)\boldsymbol{v} + B\boldsymbol{v}$ with ($\mathbb{I}_n$ denotes the $n \times n$ identity matrix)

$$A(\boldsymbol{n}) = \begin{pmatrix} (\boldsymbol{u_0}\cdot\boldsymbol{n})\mathbb{I}_n & c_0\boldsymbol{n} \\ c_0\boldsymbol{n}^\intercal & \boldsymbol{u_0}\cdot\boldsymbol{n} \end{pmatrix},\ B = \begin{pmatrix} \nabla\boldsymbol{u_0} & \frac{1}{c_0}\nabla\boldsymbol{u_0}\cdot\boldsymbol{u_0} \\ \boldsymbol{0_n}^\intercal & \gamma\nabla\cdot\boldsymbol{u_0} \end{pmatrix}.$$

The boundary matrix $A(\boldsymbol{n})$ is symmetric, with eigenvalues $\boldsymbol{u_0}\cdot\boldsymbol{n}$ of multiplicity $(n-1)$ and $\boldsymbol{u_0}\cdot\boldsymbol{n} \pm c_0|\boldsymbol{n}|$ of multiplicity 2. (Due to the homentropicity assumption, the entropy mode is absent.) The absolute value $|A(\boldsymbol{n})|$, the positive part $A(\boldsymbol{n})^\oplus$, and the negative part $A(\boldsymbol{n})^\ominus$ are defined using the diagonal form of $A(\boldsymbol{n})$ through

$$|A(\boldsymbol{n})| := P(\boldsymbol{n})\,|\Lambda(\boldsymbol{n})|\,P(\boldsymbol{n})^{-1},\ 2A(\boldsymbol{n})^\oplus := |A(\boldsymbol{n})| + A(\boldsymbol{n}),\ 2A(\boldsymbol{n})^\ominus := |A(\boldsymbol{n})| - A(\boldsymbol{n}),$$

where $|\Lambda(\boldsymbol{n})| := \mathrm{diag}([|\Lambda_i|]_{i\in[\![1,n+1]\!]})$. The symmetry of $A(\boldsymbol{n})$ implies, by definition, that the operator $\partial_t + A(\nabla)$ is a Friedrichs-symmetric operator; equivalently, (12) is a symmetric hyperbolic system [53, Def. 1.2]. Using an integration by parts, this symmetry property yields

$$(\mathcal{A}\boldsymbol{v},\boldsymbol{v})_{L^2(\Omega)} = \frac{1}{2}(C(\boldsymbol{u_0})\boldsymbol{v},\boldsymbol{v})_{L^2(\Omega)} + \frac{1}{2}(A(\boldsymbol{n})\boldsymbol{v},\boldsymbol{v})_{L^2(\partial\Omega)}, \tag{13}$$

where the symmetric amplification matrix $C(\boldsymbol{u_0})$ and the L^2 scalar products are given by

$$C(\boldsymbol{u_0}) = \begin{pmatrix} \nabla\boldsymbol{u_0} + \nabla^\intercal\boldsymbol{u_0} - (\nabla\cdot\boldsymbol{u_0})\mathbb{I}_n & \frac{1}{c_0}\nabla\boldsymbol{u_0}\cdot\boldsymbol{u_0} \\ \frac{1}{c_0}\boldsymbol{u_0}\cdot\nabla^\intercal\boldsymbol{u_0} & (2\gamma-1)\nabla\cdot\boldsymbol{u_0} \end{pmatrix}$$

and

$$(\boldsymbol{v},\boldsymbol{w})_{L^2(\Omega)} := \int_\Omega (\boldsymbol{v},\boldsymbol{w})_{\mathbb{R}^{n+1}}\,\mathrm{d}\boldsymbol{x},\ (\boldsymbol{v},\boldsymbol{w})_{L^2(\partial\Omega)} := \int_{\partial\Omega} (\boldsymbol{v},\boldsymbol{w})_{\mathbb{R}^{n+1}}\,\mathrm{d}\boldsymbol{x}.$$

In this paper, the energy analysis is carried out with the standard acoustic energy defined as [2, § 6.2] [3, § 5.6]

$$\|\boldsymbol{v}(t)\|^2_{L^2(\Omega)} := (\boldsymbol{v},\boldsymbol{v})_{L^2(\Omega)} = \int_\Omega |\tilde{p}(t,\boldsymbol{x})|^2\,\mathrm{d}\boldsymbol{x} + \int_\Omega |\boldsymbol{u}(t,\boldsymbol{x})|^2\,\mathrm{d}\boldsymbol{x}, \tag{14}$$

so that the continuous energy balance, which expresses the evolution of acoustic energy in the domain Ω, reads

$$\frac{1}{2}\frac{\mathrm{d}}{\mathrm{d}t}\|\boldsymbol{v}(t)\|^2_{L^2(\Omega)} = -(\mathcal{A}\boldsymbol{v},\boldsymbol{v})_{L^2(\Omega)} = -\frac{1}{2}(C(\boldsymbol{u_0})\boldsymbol{v},\boldsymbol{v})_{L^2(\Omega)} - \frac{1}{2}(A(\boldsymbol{n})\boldsymbol{v},\boldsymbol{v})_{L^2(\partial\Omega)}, \tag{15}$$

where the right-hand side is given by

$$\begin{aligned} (C(\boldsymbol{u_0})\boldsymbol{v},\boldsymbol{v})_{\mathbb{R}^{n+1}} &= (\nabla\cdot\boldsymbol{u_0})\left[(2\gamma-1)\tilde{p}^2 - |\boldsymbol{u}|^2\right] + 2\boldsymbol{u}\cdot\nabla\boldsymbol{u_0}\cdot\left(\boldsymbol{u} + \frac{1}{c_0}\tilde{p}\,\boldsymbol{u_0}\right) \\ (A(\boldsymbol{n})\boldsymbol{v},\boldsymbol{v})_{\mathbb{R}^{n+1}} &= (\boldsymbol{u_0}\cdot\boldsymbol{n})\left[\tilde{p}^2 + |\boldsymbol{u}|^2\right] + 2c_0\,\tilde{p}(\boldsymbol{u}\cdot\boldsymbol{n}). \end{aligned} \tag{16}$$

The expression of $(A(\boldsymbol{n})\boldsymbol{v},\boldsymbol{v})_{\mathbb{R}^{n+1}}$ suggests the following assumption.

Assumption 10. The base flow $\boldsymbol{u_0}$ obeys (at least) a slip condition $\boldsymbol{u_0}\cdot\boldsymbol{n} = 0$ at the impedance boundary Γ_z.

Thanks to this assumption, an admissible impedance yields $\int_0^t (A(\boldsymbol{n})\boldsymbol{v},\boldsymbol{v})_{L^2(\Gamma_z)}\,\mathrm{d}\tau \geq 0$ and there is energy dissipation at the impedance boundary Γ_z. Therefore, in the absence of other boundary sources, the presence of an instability is linked to the spectrum of the amplification matrix $C(\boldsymbol{u_0})$. Intuitively, this a priori energy estimate yields uniqueness of the solution, and is the stepping stone to obtain well-posedness in $e^{-\kappa t}\mathcal{C}((0,\infty);H^1(\Omega)^{n+1})$ with κ finite [53]. It also follows from the energy estimate that $\kappa \geq \min_{x\in\Omega}\lambda_{\min}(\boldsymbol{u_0})$, where $\lambda_{\min}(\boldsymbol{u_0})$ is the minimum eigenvalue of $C(\boldsymbol{u_0})$. A sufficient condition for stability is that $\min_{x\in\Omega}\lambda_{\min}(\boldsymbol{u_0}) \geq 0$, which is a stringent condition on the base flow $\boldsymbol{u_0}(\boldsymbol{x})$. This assumption is typically not verified in applications: it holds for a constant flow but fails for a Poiseuille flow for instance.

Remark 11. Although Assumption 10 is mathematically sufficient for (1), (3) to be well-posed, it is interesting to note that, physically, a no-slip condition $\boldsymbol{u_0} = 0$ is *required* at the impedance wall. Indeed, if $\boldsymbol{u_0} \neq 0$ the effect of the hydrodynamic boundary layer (refraction of sound waves [15]) must be explicitly modeled, which leads to a non-locally reacting impedance, out of the scope of this paper. For example, the standard Ingard–Myers boundary condition reads $u_n = Y(p, \nabla p)$, and has been shown by Brambley using a Briggs–Bers analysis to prevent well-posedness, in the sense that there is no finite value for κ [54]. A corrected impedance that accounts for both the acoustic and hydrodynamic boundary layers has been derived by Khamis & Brambley [17]. The computational interest of such non-local boundary conditions is that the boundary layer need not be discretized, see [28] for a use in the time domain.

Remark 12. If $\boldsymbol{u_0}$ is uniform, the acoustical energy (14) satisfies a conservation law, namely (15). A wider class of base flows can be covered using the aeroacoustical energy introduced by Cantrell and Hart, which reads [55, Eq. (16)]

$$\|\boldsymbol{v}\|_{\mathrm{CH}}^2 := \|\tilde{p}\|_{L^2(\Omega)}^2 + \|\boldsymbol{u}\|_{L^2(\Omega)}^2 + 2(\tilde{p}, \boldsymbol{M_0}\cdot\boldsymbol{u})_{L^2(\Omega)} = \int_\Omega \left|\boldsymbol{u} + \tilde{p}\boldsymbol{M_0}\right|^2 \mathrm{d}\boldsymbol{x} + \int_\Omega \left(1 - |\boldsymbol{M_0}|^2\right)|\tilde{p}|^2 \,\mathrm{d}\boldsymbol{x},$$

and defines a norm if and only if $\|\boldsymbol{M_0}\|_{L^\infty(\Omega)} < 1$ where $\boldsymbol{M_0} := \boldsymbol{u_0}/c_0$. Under Assumption 10, using $\|\cdot\|_{\mathrm{CH}}$ instead of $\|\cdot\|_{L^2(\Omega)}$ in (15) yields the boundary term $(A_{\mathrm{CH}}(\boldsymbol{n})\boldsymbol{v}, \boldsymbol{v})_{\mathbb{R}^{n+1}} := 2c_0\left[\tilde{p} + \boldsymbol{M}_{0,\parallel}\cdot\boldsymbol{u}_\parallel\right](\boldsymbol{u}\cdot\boldsymbol{n})$, where the subscript "$\parallel$" denotes the tangential component. The boundary term (16) is recovered if $\boldsymbol{u_0}$ obeys a no-slip condition.

3. Physical reflection coefficient models in the time domain

As mentioned in the introduction, a discrete TDIBC consists of three components: a discrete time-domain impedance model, an algorithm to compute said discrete model, and a coupling method with the considered PDE. This section tackles the first two components, while the last one is covered *independently* in Sec. 4, so that Secs. 3 and 4 can be read independently. This section is purely focused on the impedance models and does not rely on $(\boldsymbol{u}, \tilde{p})$ satisfying a particular equation in Ω. The broad purpose of this section is to derive time-local discrete models from the analysis of physical models, for later use in Secs. 5 and 6. The presented analysis focuses on models suitable for acoustical liners, recalled in Sec. 3.1, which include an example of nonlinear scattering operator. The last two sections focus on the two linear models. Sec. 3.2 gives the oscillatory-diffusive representation of their reflection coefficients, which yield a formulation with an infinite number of *delayed* ODEs. Its practical discretization is then tackled in Sec. 3.3, where the time delay is recast using a transport equation, thus yielding a purely time-local formulation.

3.1. Physical models for acoustical liners

The numerical application presented in Sec. 6 involves two so-called single degree of freedom acoustical liners: a ceramic tubular (CT) liner made from a ceramic tubular core (channel of length l_c, diameter d_c, and porosity $\sigma_c \in (0, 1]$) and a rigid backplate; a micro-perforated (MP) liner made from a honeycomb core (cell of length l_c, diameter d_c, and porosity $\sigma_c \in (0, 1]$) sandwiched between a perforated facesheet (thickness l_p, hole diameter d_p, and porosity $\sigma_p \in (0, 1]$) and a rigid backplate. CT liners are mostly used in academic and benchmark experiments, while MP liners are widely used in industrial applications. The standard linear impedance model for these liners reads

$$\hat{z}_{\mathrm{phys}}(s) = \sigma_p^{-1}\hat{z}_p(s) + \sigma_c^{-1}\hat{z}_c(s) \tag{17}$$

where $\hat{z}_p$ (resp. $\hat{z}_c$) is the impedance of a perforation (resp. cavity). The CT liner model $\hat{z}_{\mathrm{CT}}$ is obtained with $\hat{z}_p = 0$, while $\sigma_c = 1$ yields the MP liner model $\hat{z}_{\mathrm{MP}}$. (See [5] and references therein for a wider panel of linear impedance models.) The expression (17) separates the contribution of the perforated plate from that of the cavity, a feature that assumes the conservation of $\boldsymbol{u}\cdot\boldsymbol{n}$ across the perforation, which is verified as long as the perforation thickness l_p is much shorter than the considered wavelengths.

The chosen perforation model is given by a fractional polynomial

$$\frac{\hat{z}_p}{z_0}(s) = a_0 + a_{1/2}\sqrt{s} + a_1 s, \tag{18}$$

where each of the non-negative coefficients has a physical interpretation: a_0 models frequency-independent losses, $a_{1/2}$ frequency-dependent losses coming from visco-thermal effects, and a_1 is known as the mass reactance and does not incur any loss. Note that if $a_{1/2} \neq 0$, $\hat{z}_p$ is *multivalued*: in this work the cut is always defined as $(-\infty, 0]$ and $\sqrt{\cdot}$ denotes the branch that coincides with the real-valued square root on $(0, \infty)$ [56, § I.4]. Values for the three coefficients can be obtained through various theoretical or empirical models; the high-frequency approximation of a model derived by Crandall, based on the axisymmetric Stokes equations, yields [5, Eq. 7]

$$a_0 = \frac{3l_p\nu}{c_0\,(d_p/2)^2},\quad a_{1/2} = \frac{2l_p\sqrt{\nu}}{c_0 d_p/2},\quad a_1 = \frac{l_p}{c_0}, \tag{19}$$

where ν denotes the kinematic viscosity. For the cavity, the adopted model is a monodimensional wave equation with a fractional wavenumber $k_c(s)$

$$\frac{\hat{z}_c}{z_0}(s) = \coth(\mathrm{j}k_c(s)l_c),\ \mathrm{j}k_c(s)l_c = b_0 + b_{1/2}\sqrt{s} + b_1 s. \tag{20}$$

The non-negative coefficients b have a physical interpretation similar to those of (18): b_0 models frequency-independent losses, $b_{1/2}$ frequency-dependent losses, and b_1 is half the back-and-forth traveling time in the cavity. The high-frequency approximation of a wavenumber derived by Bruneau gives [5, Eq. 26]

$$b_0 = 0,\ b_{1/2} = \frac{\sqrt{\nu}}{c_0 d_c/2}\left(\frac{\gamma-1}{\sqrt{\mathrm{Pr}}}+1\right)l_c,\ b_1 = \frac{l_c}{c_0}, \tag{21}$$

where Pr is the Prandtl number. From Proposition 3, to check the admissibility of these linear models it is sufficient to check that $\hat{z}(s)$ is a positive-real function, which is straightforward.

By contrast with the CT liner, the MP liner is sensitive to the incident sound pressure level: above a given threshold, nonlinear effects occur in the perforation. The prevailing nonlinear term for a perforated plate with porosity σ_p is based on the incompressible Bernoulli equation, and has been derived by Cummings [7, Eq. 1]

$$\frac{\mathcal{Z}_{\mathrm{nl}}}{z_0}(\boldsymbol{u}\cdot\boldsymbol{n}) = \frac{C_{\mathrm{nl}}}{c_0}|\boldsymbol{u}\cdot\boldsymbol{n}|\boldsymbol{u}\cdot\boldsymbol{n},\ C_{\mathrm{nl}} = \frac{1-C_c^2}{2\sigma_p^2 C_c^2}, \tag{22}$$

where the nondimensional coefficient $C_c \in (0,1]$ is known as the contraction coefficient. Evidence for the relevance of this model has been provided by Singh & Rienstra [57]. Since the model is nonlinear, it is naturally expressed in the time domain. It is straightforward to check that this single-input single-output operator is real-valued, causal and passive (since $(|u|u)u \geq 0$, the passivity condition (5) is verified): therefore, it defines an admissible impedance model. By contrast with linear models, expressing the admittance and scattering operators of a nonlinear impedance model is more intricate. Let us give an elementary *algebraic* example by studying the impedance model

$$\frac{\mathcal{Z}}{z_0}(\boldsymbol{u}\cdot\boldsymbol{n}) = a_0\boldsymbol{u}\cdot\boldsymbol{n} + \frac{C_{\mathrm{nl}}}{c_0}|\boldsymbol{u}\cdot\boldsymbol{n}|\boldsymbol{u}\cdot\boldsymbol{n}. \tag{23}$$

A somewhat tedious but straightforward computation shows that the admittance and scattering operators are given by

$$\mathcal{Y}(p) = \frac{2\tilde{p}}{a_0 + \sqrt{a_0^2 + 4\frac{C_{\mathrm{nl}}}{c_0}|\tilde{p}|}} \tag{24}$$

$$\mathcal{B}(\tilde{p}+\boldsymbol{u}\cdot\boldsymbol{n}) = \beta_0\frac{2(\tilde{p}+\boldsymbol{u}\cdot\boldsymbol{n})}{1+\sqrt{1+\frac{4C_{\mathrm{nl}}}{(1+a_0)^2}\frac{|\tilde{p}+\boldsymbol{u}\cdot\boldsymbol{n}|}{c_0}}} + \frac{1}{c_0}\frac{C_{\mathrm{nl}}}{(1+a_0)^2}\frac{4|\tilde{p}+\boldsymbol{u}\cdot\boldsymbol{n}|(\tilde{p}+\boldsymbol{u}\cdot\boldsymbol{n})}{\left(1+\sqrt{1+\frac{4C_{\mathrm{nl}}}{(1+a_0)^2}\frac{|\tilde{p}+\boldsymbol{u}\cdot\boldsymbol{n}|}{c_0}}\right)^2}, \tag{25}$$

where $\beta_0 = (a_0-1)/(a_0+1)$ is the reflection coefficient associated with a_0. To the best of the authors' knowledge, the nonlinear admittance and scattering operators (24), (25) have never been considered. The expression (25) is used in Sec. 5 to illustrate the computational interest of nonlinear scattering operators.

Remark 13. In [34], a nonlinear model is used to model injectors of a combustion chamber in a LES simulation. The corresponding scattering operator is $\mathcal{B}(v)(t) = \chi_a(v)(t-\tau)$ where $\tau > 0$ is a time delay and χ_a is an algebraic function of the incoming characteristic [34, Eq. (2.15)].

The effect of a grazing flow on the impedance of a sound absorbing material has been studied both experimentally [10] and numerically [11] using direct numerical simulations. For a perforated plate backed by an air-filled cavity, a grazing flow is usually associated with a resistance increase that degrades the material performance. Kirby and Cummings proposed an experimental correlation between the impedance and the wall friction velocity, namely [10, Eqs. (12)–(13)]. This result suggests that the grazing flow can be *empirically* modeled as an additional parametric dependence, which preserves the locally-reacting nature of the IBC.

3.2. Oscillatory-diffusive representation of physical reflection coefficient models

In [5], it is shown that the time-domain convolution $z_{\mathrm{phys}} \star u$ can be expressed without any approximation using an infinite number of ODEs, some of which may be delayed. This result is obtained by deriving the so-called oscillatory-diffusive representation of the physical model z_{phys} using complex calculus. However, as shown in Sec. 4, it is computationally advantageous to enforce the IBC through the scattering formulation (8) rather than the impedance or admittance formulations

(2), (6). This section shows that, fortunately, the reflection coefficient $\hat{\beta}_{\text{phys}}$ does also enjoy an oscillatory-diffusive representation, given by (29). (As a matter of fact, this is also the case for the admittance $\hat{y}_{\text{phys}}$.) Since the computations are similar to that carried out in [5], only the key steps are provided; the reader is referred to [5,58] and references therein for background on oscillatory-diffusive representations.

The starting point of the analysis is the identity $\coth(s) = 1 + 2e^{-2s}(1 - e^{-2s})^{-1}$ that enables to rewrite the reflection coefficient ((11), (17)) as

$$\hat{\beta}_{\text{phys}}(s) = 1 + \hat{h}_1(s) + e^{-s\tau}\hat{h}_2(s), \tag{26}$$

where the time delay $\tau := 2b_1 > 0$ is the cavity back-and-forth traveling time and the functions $\hat{h}_1$ and $\hat{h}_2$, which induce deviations from the rigid wall $\hat{\beta}_{\text{phys}}(s) = 1$, are given by

$$\hat{h}_1(s) = -\frac{2}{R(s)},\ \hat{h}_2(s) = -\hat{h}_1(s)e^{-2(b_0+b_{1/2}\sqrt{s})},\ R(s) = 1 + \frac{1}{\sigma_c} + \frac{1}{\sigma_p}\hat{z}_p(s) + \left(-1 + \frac{1}{\sigma_c} - \frac{1}{\sigma_p}\hat{z}_p(s)\right)e^{-2\mathrm{j}k_c(s)l_c}.$$

The interest of the apparently gratuitous expression (26) is that both $\hat{h}_1$ and $\hat{h}_2$ admit an oscillatory-diffusive representation ((27), (28)). The analytical expression of these two functions is used in the discretization methodology presented in Sec. 3.3.1. The representation of $\hat{h}_i$ ($i \in \{1, 2\}$) is derived by inverting the Laplace transform using the residue theorem [56, Chap. VII] on a "keyhole-shaped" Bromwich contour $\mathcal{C}_{R,\epsilon}$. Among the sufficient hypotheses needed to carry out the computations, $\hat{h}_i$ must decay uniformly on $\{|s| = R\}$ as $R \to \infty$ and admit finite residues at every pole and branch points (the only possible branch point of $\hat{h}_i$ is 0).

If $a_{1/2}$ or a_1 are positive (which is the case for an MP liner), the oscillatory-diffusive representation of $\hat{h}_i$ is

$$\hat{h}_i(s) = \sum_{n\in I}\frac{r_{i,n}}{s - s_n} + \int_0^\infty \frac{\mu_i(\xi)}{s + \xi}\mathrm{d}\xi, \tag{27}$$

where $(s_n)_n$ with $n \in I \subset \mathbb{Z}$ is the sequence of poles of $\hat{h}_i$, each one solving $R(s_n) = 0$, $r_{i,n}$ is the associated residue $r_{i,n} := \text{Res}(\hat{h}_i, s_n)$, and μ_i is the so-called diffusive weight (or measure), linked to the jump of $\hat{h}_i$ across its cut $(-\infty, 0]$ by $\mu_i(\xi) := (\mathrm{j}2\pi)^{-1}[\hat{h}_i(\xi e^{-\mathrm{j}\pi}) - \hat{h}_i(\xi e^{+\mathrm{j}\pi})]$. These quantities can be readily computed numerically (the poles s_n are not always known analytically), which enables to verify (27). The first (resp. second) term on the right-hand side of (27) is the oscillatory (resp. diffusive) part of $\hat{h}_i$. The oscillatory part is associated with the resonances, by contrast with the diffusive part that stems from visco-thermal losses. Indeed, without the multivalued fractional term $\sqrt{s}$ (physically, if $\nu = 0$, see (19)) the diffusive part vanishes, i.e. $\mu_i = 0$. The admissibility conditions given by Proposition 8 imply that $\mu(\xi) \in \mathbb{R}$ and that if s_n is a pole of $\hat{h}_i$ with residue $r_{i,n}$, then $\overline{s_n}$ is a pole of $\hat{h}_i$ with residue $\overline{r_{i,n}}$ (hermitian symmetry). The desired representation of $\hat{\beta}_{\text{MP}}$ is then obtained by combining (26) and (27).

However, for the CT liner $\hat{z}_p(s) = 0$ so that $\hat{h}_1$ (and $\hat{h}_2$ if $b_{1/2} = 0$) fails the decay condition on $\{|s| = R\}$ as $R \to \infty$. By considering instead $\hat{h}_1(s)/s$, the following representation can be derived, assuming $\sigma_c \neq 1$,

$$\hat{h}_1(s) = C + \sum_{n\in I}\frac{r_{1,n}}{s - s_n} + \int_0^\infty \frac{\mu_1(\xi)}{s + \xi}\mathrm{d}\xi,\ C \simeq -\frac{1}{1 + \sigma_c^{-1}}, \tag{28}$$

which differs from (27) by a real constant C. The representation of $\hat{\beta}_{\text{CT}}$ is then obtained by combining (26), (27) with $i = 2$, and (28). Overall, for both liners, the physical reflection coefficient has the causal representation

$$\beta_{\text{phys}}(t) = \beta_1\,\delta(t) + \sum_{n\in I} r_{1,n}e^{s_n t_+} + \int_0^\infty \mu_1(\xi)e^{-\xi t_+}\mathrm{d}\xi + \sum_{n\in I} r_{2,n}e^{s_n(t-\tau)_+} + \int_0^\infty \mu_2(\xi)e^{-\xi(t-\tau)_+}\mathrm{d}\xi, \tag{29}$$

where $e^{st_+} := e^{st}H(t)$ denotes the causal exponential function and $\beta_1 \in \mathbb{R}$. The importance of (29) lies in the fact that it provides a structural information on β_{phys}, namely that it "reduces" to an infinite number of first-order systems with delay

$$\beta_{\text{phys}} \star v(t) = \beta_1 v(t) + \sum_{n\in I} r_{1,n}\varphi(t, s_n) + \int_0^\infty \mu_1(\xi)\varphi(t, -\xi)\mathrm{d}\xi + \sum_{n\in I} r_{2,n}\varphi(t-\tau, s_n) + \int_0^\infty \mu_2(\xi)\varphi(t-\tau, -\xi)\mathrm{d}\xi, \tag{30}$$

where $\varphi(t, s) := (e^{st_+} \star v)(t)$ and v is a shorthand for "$\tilde{p} + \boldsymbol{u}\cdot\boldsymbol{n}$". The computational interest of (30) stems from the ability to compute φ through the first-order ODEs $\partial_t\varphi(t, s) = s\varphi(t, s) + v(t)$ with null initial condition $\varphi(t = 0, s) = 0$. As a result, (30) is a time-local (but infinite-dimensional) representation of the hereditary convolution operator $\mathcal{B}(v) = \beta_{\text{phys}} \star v$. Theoretically, this representation enjoys an energy balance, useful for stability analyses (see Sec. 4 and Appendix C). The above analysis informs the discrete model proposed in the next section.

3.3. Discrete reflection coefficient model

The identity (30) naturally suggests to define the discrete reflection coefficient model $\tilde{\beta}$ as

$$\begin{aligned}\hat{\tilde{\beta}}(s) &= \tilde{\beta}_\infty + \sum_{n=1}^{N_s} \frac{\tilde{r}_{1,n}}{s-\tilde{s}_n} + \sum_{k=1}^{N_\xi} \frac{\tilde{\mu}_{1,k}}{s+\tilde{\xi}_k} + e^{-s\tilde{\tau}} \left(\sum_{n=1}^{N_s} \frac{\tilde{r}_{2,n}}{s-\tilde{s}_n} + \sum_{k=1}^{N_\xi} \frac{\tilde{\mu}_{2,k}}{s+\tilde{\xi}_k} \right) \\ \tilde{\beta} \star v(t) &= \tilde{\beta}_\infty v(t) + \sum_{n=1}^{N_s} \tilde{r}_{1,n} \varphi(t, \tilde{s}_n) + \sum_{k=1}^{N_\xi} \tilde{\mu}_{1,k} \varphi(t, -\tilde{\xi}_k) + \sum_{n=1}^{N_s} \tilde{r}_{2,n} \varphi(t-\tilde{\tau}, \tilde{s}_n) + \sum_{k=1}^{N_\xi} \tilde{\mu}_{2,k} \varphi(t-\tilde{\tau}, -\tilde{\xi}_k),\end{aligned} \tag{31}$$

where $\varphi(t,\cdot)$ follows the first-order ODE defined above. It involves $N_\varphi := N_s + N_\xi$ additional variables, where N_ξ (resp. N_s) variables come from the diffusive (resp. oscillatory) part of β_{phys}. Note that $\tilde{\beta}_\infty = \hat{\tilde{\beta}}(+\infty) \in [-1,1]$ from Proposition 8. In summary, the analysis of the physical model (17) has led to the discrete model (31), which requires the computation and delay of N_φ ODEs. Without the delay $\tilde{\tau} = 0$, the derived model $\tilde{\beta}$ can be interpreted as a so-called multipole model, postulated in [47] for instance [5, § I]. In preparation for the application of (31) presented in Secs. 5 and 6, Sec. 3.3.1 discusses the computation of the poles $(\tilde{s}_n, \tilde{\xi}_k)_{n,k}$ and weights $(\tilde{r}_{i,n}, \tilde{\mu}_{i,k})_{n,k}$, while Sec. 3.3.2 covers the time delay discretization.

3.3.1. Poles and weights computation

The discrete model $\tilde{\beta}$ is fully determined by the constant $\tilde{\beta}_\infty$, N_φ poles $(\tilde{s}_n, \tilde{\xi}_k)_{n,k}$, $2N_\varphi$ weights $(\tilde{r}_{i,n}, \tilde{\mu}_{i,k})_{n,k}$, and time delay $\tilde{\tau}$. These parameters should be such that $\tilde{\beta}$ is a satisfactory representation of the considered sound absorbing material, typically known by its physical characteristics and possibly some experimental data $(\hat{\beta}_{\text{exp}}(\mathrm{j}2\pi f_m))_m$. Criteria for a satisfactory approximation include: $\hat{\tilde{\beta}}$ is a bounded real function (see Proposition 8); N_φ is as low as possible; $\omega \mapsto \hat{\tilde{\beta}}(\mathrm{j}\omega)$ has a physical behavior at frequencies not covered by the experimental data (usually low and high frequencies); the maximum frequency $(2\pi)^{-1} \max_{n,k}(|\tilde{s}_n|, \tilde{\xi}_k)_{n,k}$ is consistent with the stability region of the time discretization scheme (otherwise the IBC could reduce the timestep of an explicit integration). In Sec. 6, the three-step methodology given below is followed. The principle of the approach is to use as much as possible the information obtained on the physical model in Sec. 3.2 to ease the optimization process.

1. (Physical model) Compute the coefficients a and b from the liner dimensions using the models (19), (21). In particular, this provides a value for the constant β_1 and the time delay τ. These coefficients can then serve as an initial point for a nonlinear least squares optimization on $\omega \mapsto \|\hat{z}_{\text{phys}}(\mathrm{j}\omega) - \hat{z}_{\text{exp}}(\mathrm{j}\omega)\|$. This optimization can be interpreted as computing the various physical impedance corrections [6,7].
   Inputs: material characteristics (l_p, d_p, σ_c, etc.), experimental data $(\hat{z}_{\text{exp}}(\mathrm{j}2\pi f_m))_m$.
   Outputs: coefficients $(\sigma_p^{-1}a_0, \sigma_p^{-1}a_{1/2}, \sigma_p^{-1}a_1, \sigma_c, b_0, b_{1/2}, b_1)$, time delay $\tau = 2b_1$, constant $\beta_1 = 1 - (1+\sigma_c^{-1})^{-1}$.
2. (Discrete model – Linear least squares) *Choose* N_ξ diffusive poles along the cut $(-\infty, 0]$ (typically, a logarithmic repartition is satisfactory). *Compute* N_s oscillatory poles $\tilde{s}_n$ by solving $R(\tilde{s}_n) = 0$. Compute the weights $(\tilde{r}_{n,i})_n$ and $(\tilde{\mu}_{k,i})_k$ by minimizing $\omega \mapsto \| \sum_{k=1}^{N_\xi} \frac{\tilde{\mu}_{k,i}}{\mathrm{j}\omega + \tilde{\xi}_k} + \sum_{n=1}^{N_s} \frac{\tilde{r}_{n,i}}{\mathrm{j}\omega - \tilde{s}_n} - \hat{h}_i(\mathrm{j}\omega) \|$ if (27) holds (add the constant if (28) holds). This is an overdetermined *linear* least squares optimization that is solved instantaneously by pseudo-inverse. See [5, § IV.D,VI.A] for additional details. Note that the time delay $\tilde{\tau}$ has no role whatsoever during this step.
   Inputs: $\hat{h}_i$ (from output of step 1), number of poles N_s, diffusive poles $(\xi_k)_{k \in [\![1, N_\xi]\!]}$.
   Outputs: oscillatory poles $(\tilde{s}_n)_{n \in [\![1, N_s]\!]}$, weights $(\tilde{r}_{n,i})_{n \in [\![1, N_s]\!]}$ and $(\tilde{\mu}_{k,i})_{k \in [\![1, N_\xi]\!]}$ $(i \in \{1,2\})$.
3. (Discrete model – Nonlinear least squares) Compute new poles and weights with a nonlinear least squares optimization on $\omega \mapsto \|\hat{\tilde{\beta}}(\mathrm{j}\omega) - \hat{\beta}_{\text{exp}}(\mathrm{j}\omega)\|$ with initial poles and weights given by step 2, $\tilde{\beta}_\infty = \beta_1$ and $\tilde{\tau} = \tau$ from step 1. The constant $\tilde{\beta}_\infty$ and delay $\tilde{\tau}$ can also be optimized along the poles and weights.
   Inputs: $(\tilde{s}_n, \tilde{\xi}_k)_{n,k}$, $(\tilde{r}_{n,i}, \tilde{\mu}_{k,i})_{n,k}$, $\tilde{\tau} = \tau$, $\tilde{\beta}_\infty = \beta_1$, $(\hat{\beta}_{\text{exp}}(\mathrm{j}2\pi f_m))_m$.
   Outputs: $(\tilde{s}_n, \tilde{\xi}_k)_{n,k}$, $(\tilde{r}_{n,i}, \tilde{\mu}_{k,i})_{n,k}$, (optional) $\tilde{\tau}$, (optional) $\tilde{\beta}_\infty$.

When the physical model is satisfactory, as is the case for the MP and CT liners considered herein, the first two steps deliver a discrete model $\tilde{\beta}$ that may be sufficient for some engineering applications. If step 3 is used, its role is to adjust the poles and weights to improve the fit against experimental data. The first two steps can then be interpreted as using a physical model to help finding an initial guess for the poles and weights. When faced with a mismatch between the physical model and experimental data, tuning the former may be required, but this is not a computationally intensive task since there are few parameters and they have a physical interpretation. The third stage can be performed using any nonlinear least squares method: in Sec. 6, we simply relied on the trust region optimization method [59] implemented in MATLAB® `lsqnonlin`, whose execution takes a few seconds on a contemporary computer, but the more tailored vector fitting algorithm [60] can also be used, as in [27].

However, note that step 3 comes with the following caveat. There is a trade-off between the fit quality against the experimental data, which is usually narrowband, and the broadband behavior of $\hat{\tilde{\beta}}$. This trade-off is especially acute when

using impedance identified with base flow, as these can be associated with significant uncertainties that ideally should be accounted for in the optimization process. This is exemplified by the question of whether to optimize the time delay $\tilde{\tau}$. Physically, it is linked to the anti-resonant frequencies f_n given by $f_n = n/\tilde{\tau}$ for (17) with a lossless cavity $b_0 = b_{1/2} = 0$ (i.e. a canonical Helmholtz resonator). Therefore, although $\tilde{\tau} \neq \tau$ may enable a better fit, it may not be worth altering the broadband behavior. Eventually, knowledge about both the model and experimental data is helpful to inform the optimization process.

3.3.2. Time delay discretization

The discretization of the time delay is done independently of the choice of weights and poles described in Sec. 3.3.1. Theoretically, the delay can be recast into $\varphi(t - \tilde{\tau}, s) = \psi(t, s, -l_{\tilde{\tau}})$ where the additional function $\psi(\cdot, s, \cdot)$ obeys the following transport equation on $(-l_{\tilde{\tau}}, 0)$ with $l_{\tilde{\tau}} = c_{\tilde{\tau}}\tilde{\tau} > 0$

$$\begin{aligned} &\partial_t \psi(t, s, \theta) = c_{\tilde{\tau}} \partial_\theta \psi(t, s, \theta) \quad (t \in (0, \infty),\ \theta \in (-l_{\tilde{\tau}}, 0)) \\ &\psi(t, s, 0) = \varphi(t, s),\ \psi(0, s, \theta) = 0. \end{aligned} \tag{32}$$

This device is commonly used in theoretical and numerical studies of delay differential equations, see the references in [61] and [62, § 1]. Although not needed herein, several delays $\tilde{\tau}_i$ can also be tackled by defining $\tilde{\tau} := \max_i \tilde{\tau}_i$. The monodimensional PDE (32) is discretized using a discontinuous Galerkin method with N_K elements and $N_p \geq 2$ nodes per element (order N_p). The discretization accuracy is measured by the number of points per wavelength

$$\mathrm{PPW}_{\tilde{\tau}}(f_{\max}) := \frac{N_\psi}{\tilde{\tau} f_{\max}}, \tag{33}$$

where $N_\psi := N_K N_p$ is the total number of nodes and $f_{\max}$ is the maximum frequency of interest. Target values for $\mathrm{PPW}_{\tilde{\tau}}$ as a function of N_p can be found in [63, Tab. 1], which shows that it is advantageous to choose $N_K = 1$ so that N_p is the sole discretization parameter. The impact of $\mathrm{PPW}_{\tilde{\tau}}$ is illustrated in Sec. 6. Herein, the main argument in favor of delaying through a transport equation, compared to continuous Runge–Kutta methods [64], is the meaningfulness of (33) for wave propagation problems, which makes the discretization straightforward to set up a priori.

In summary, the discrete impedance model (31) is computed through

$$\tilde{\beta} \star v(t) = \tilde{\beta}_\infty v(t) + \sum_{n=1}^{N_s} \tilde{r}_{1,n} \varphi(t, \tilde{s}_n) + \sum_{k=1}^{N_\xi} \tilde{\mu}_{1,k} \varphi(t, -\tilde{\xi}_k) + \sum_{n=1}^{N_s} \tilde{r}_{2,n} \psi(t, \tilde{s}_n, -l_{\tilde{\tau}}) + \sum_{k=1}^{N_\xi} \tilde{\mu}_{2,k} \psi(t, -\tilde{\xi}_k, -l_{\tilde{\tau}}), \tag{34}$$

which implies the use of $(N_\psi + 1)N_\varphi$ additional variables. The two parameters to control are $\max_{k,n}(\xi_k, |s_n|)$, which is to be chosen in accordance with the spatial discretization scheme, and $\mathrm{PPW}_{\tilde{\tau}}(f_{\max})$, for which values are given in [63, Tab. 1]. This covers the first two components of the TDIBC. The next section deals with the third, necessary for the numerical applications of Secs. 5 and 6.

Remark 14. The discrete model (34) has been derived from a mathematical analysis that emphasizes the distinct components of the model (26): an oscillatory-diffusive part that models both oscillatory and diffusion phenomena (the latter of parabolic nature), and a hyperbolic part associated with the time delay that models a wave reflection phenomenon. In [32, § 4.1.1], a first-order finite-difference discretization of the monodimensional LEEs is used to truncate a combustion chamber. An alternative discretization strategy is to perform a rational approximation of the time delay, see [61] and references therein. For a pure time delay, i.e. $\hat{\beta}(s) \propto e^{-\tau s}$, a multipole approximation method is presented in [33].

4. Numerical fluxes for nonlinear time-domain impedance boundary conditions

This section deals with the third component of a TDIBC, namely its (semi-)discrete formulation, *independently* of Sec. 3. It analyzes the weak enforcement of an admissible IBC within a discontinuous Galerkin (DG) finite element method, but the numerical flux formalism is employed to enable a straightforward transition to other methods popular in fluid mechanics. For the analysis, the IBC is only assumed admissible and need not be given by one of the models covered in Sec. 3, so that both sections are independent. The analysis shows the computational interest of a numerical flux based on the scattering operator $\mathcal{B}$ (10), the so-called $\mathcal{B}$-flux ((39), (63)), over fluxes based on the impedance and admittance, namely the $\mathcal{Z}$-flux ((39), (59)) and the $\mathcal{Y}$-flux ((39), (61)). This justifies a posteriori the interest in $\mathcal{B}$ displayed in Sec. 3 and prepare the numerical applications of Secs. 5 and 6. The section starts with a brief introduction of the standard DG method in Sec. 4.1. Sec. 4.2 then defines admissibility conditions for an impedance numerical flux, upon which the analyses of Secs. 4.3 and 4.4 rely.

4.1. Discontinuous Galerkin method

Let $(\mathcal{T}_h)_h$ be a quasi-uniform sequence of meshes indexed by $h := \max_{T \in \mathcal{T}_h} h_T$, where h_T denotes the diameter of the element $T \in \mathcal{T}_h$. For simplicity, each mesh $\mathcal{T}_h$ is assumed to be simplicial, geometrically conformal, and shape-regular. Let $\mathbb{P}_n^k$

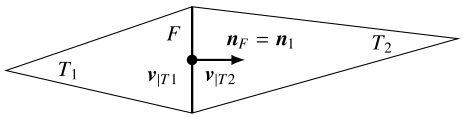

Fig. 1. Notations for an interior face $F \in \mathcal{F}_h^i$.

be the space of polynomials of n variables and total degree at most k. The approximation space is taken as $V_h := \mathbb{P}_n^k(\mathcal{T}_h)^{n+1}$, where $\mathbb{P}_n^k(\mathcal{T}_h)$ is the broken polynomial space defined as $\mathbb{P}_n^k(\mathcal{T}_h) := \{v \in L^2(\Omega) \,|\, \forall T \in \mathcal{T}_h,\ v_{|T} \in \mathbb{P}_n^k(T)\}$. The domain Ω is assumed to be a polyhedron, so that it can be exactly covered by each mesh. See [65, Chap. 1] and [66, Chap. 1] for definitions of the mentioned properties (more detailed citations are available in Appendix B). The semi-discrete formulation of (12) reads: find $\boldsymbol{v}_h \in \mathcal{C}^1([0,\infty), V_h)$ such that

$$\partial_t \boldsymbol{v}_h + \mathcal{A}_h \boldsymbol{v}_h = 0, \tag{35}$$

where the spatial discretization is embodied by the finite-dimensional operator $\mathcal{A}_h : V_h \to V_h$ defined by

$$\forall \boldsymbol{w}_h \in V_h,\ (\mathcal{A}_h \boldsymbol{v}_h, \boldsymbol{w}_h)_{L^2(\Omega)} := \sum_{T\in\mathcal{T}_h} (\mathcal{A}\boldsymbol{v}_h, \boldsymbol{w}_h)_{L^2(T)} + ((A(\boldsymbol{n})\boldsymbol{v}_h)^* - A(\boldsymbol{n})\boldsymbol{v}_h, \boldsymbol{w}_h)_{L^2(\partial T)},$$

where the quantity $(A(\boldsymbol{n})\boldsymbol{v}_h)^*$ is the so-called numerical flux function, uniquely defined at each face. Intuitively, this definition can be viewed as resulting from two integration by parts. At an interior face $F \in \mathcal{F}_h^i$ we use the upwind flux $(A(\boldsymbol{n}_F)\boldsymbol{v})^* := A(\boldsymbol{n}_F)^{\oplus}\boldsymbol{v}_{|T_1} - A(\boldsymbol{n}_F)^{\ominus}\boldsymbol{v}_{|T_2} = A(\boldsymbol{n}_F)\{\boldsymbol{v}\} + \frac{1}{2}|A(\boldsymbol{n}_F)|[\![\boldsymbol{v}]\!]$ where $\{\boldsymbol{v}\} := (\boldsymbol{v}_{|T_1} + \boldsymbol{v}_{|T_2})/2$ is the face average and $[\![\boldsymbol{v}]\!] := \boldsymbol{v}_{|T_1} - \boldsymbol{v}_{|T_2}$ is the face jump, see Fig. 1 for the face-specific notations. This leads to

$$\begin{aligned}(\mathcal{A}_h \boldsymbol{v}_h, \boldsymbol{w}_h)_{L^2(\Omega)} = &\sum_{T\in\mathcal{T}_h} (\mathcal{A}\boldsymbol{v}_h, \boldsymbol{w}_h)_{L^2(T)} + ((A(\boldsymbol{n})\boldsymbol{v}_h)^* - A(\boldsymbol{n})\boldsymbol{v}_h, \boldsymbol{w}_h)_{L^2(\partial\Omega)} \\ &- \sum_{F\in\mathcal{F}_h^i} (A(\boldsymbol{n}_F)[\![\boldsymbol{v}_h]\!], \{\boldsymbol{w}_h\})_{L^2(F)} + \frac{1}{2}\sum_{F\in\mathcal{F}_h^i} (|A(\boldsymbol{n}_F)|[\![\boldsymbol{v}_h]\!], [\![\boldsymbol{w}_h]\!])_{L^2(F)}.\end{aligned} \tag{36}$$

At a boundary face $F \in \mathcal{F}_h^b$, the IBC is weakly enforced through a numerical flux introduced in Sec. 4.2 and analyzed in Secs. 4.3 and 4.4. In the applications of Secs. 5 and 6, the numerical fluxes $(A(\boldsymbol{n}_F)\boldsymbol{v})_s^* := A(\boldsymbol{n}_F)^{\oplus}\boldsymbol{v}_{|T_1} - A(\boldsymbol{n}_F)^{\ominus}\boldsymbol{v}_s$ (source $\boldsymbol{v}_s$) and $(A(\boldsymbol{n}_F)\boldsymbol{v})_{\text{out}}^* := A(\boldsymbol{n}_F)^{\oplus}\boldsymbol{v}_{|T_1}$ (approximate non-reflecting outlet) are also used. The bilinear form (36) is standard and fits within the framework proposed by Ern & Guermond [67] for the DG discretization of Friedrichs systems, and notations have been kept as close as possible to that employed in this seminal work. The reader interested in an error analysis with the standard boundary condition "$A(\boldsymbol{n})\boldsymbol{v} = M(\boldsymbol{n})\boldsymbol{v}$" is referred to [67] and [66, Chap. 3 & 7]. The well-posedness of the semi-discrete formulation (35) follows from the Cauchy–Lipschitz–Picard theorem [68, Thm. 7.3] since it is a finite-dimensional ODE.

Using the identity (13) on each element T enables to get

$$(\mathcal{A}_h \boldsymbol{v}_h, \boldsymbol{v}_h)_{L^2(\Omega)} = \frac{1}{2}(C(\boldsymbol{u_0})\boldsymbol{v}_h, \boldsymbol{v}_h)_{L^2(\Omega)} + \frac{1}{2}|\boldsymbol{v}_h|_{\text{upw}}^2 + \left((A(\boldsymbol{n})\boldsymbol{v}_h)^* - \frac{1}{2}A(\boldsymbol{n})\boldsymbol{v}_h, \boldsymbol{v}_h\right)_{L^2(\partial\Omega)}, \tag{37}$$

where the upwind seminorm is defined as

$$|\boldsymbol{v}_h|_{\text{upw}}^2 := \sum_{F\in\mathcal{F}_h^i} (|A(\boldsymbol{n}_F)|[\![\boldsymbol{v}_h]\!], [\![\boldsymbol{v}_h]\!])_{L^2(F)}.$$

This leads to the following semi-discrete energy balance

$$\frac{1}{2}\frac{\mathrm{d}}{\mathrm{d}t}\|\boldsymbol{v}_h\|_{L^2(\Omega)}^2 = -(\mathcal{A}_h\boldsymbol{v}_h, \boldsymbol{v}_h)_{L^2(\Omega)} = -\frac{1}{2}(C(\boldsymbol{u_0})\boldsymbol{v}_h, \boldsymbol{v}_h)_{L^2(\Omega)} - \frac{1}{2}|\boldsymbol{v}_h|_{\text{upw}}^2 - \left((A(\boldsymbol{n})\boldsymbol{v}_h)^* - \frac{1}{2}(A(\boldsymbol{n})\boldsymbol{v}_h), \boldsymbol{v}_h\right)_{L^2(\partial\Omega)}, \tag{38}$$

which is to be contrasted with its continuous counterpart (15). The term $|\boldsymbol{v}_h|_{\text{upw}}^2$ is the energy dissipation due to the use of an upwind flux (it would be null had a centered flux been used) while the boundary term $((A(\boldsymbol{n})\boldsymbol{v}_h)^* - \frac{1}{2}A(\boldsymbol{n})\boldsymbol{v}_h, \boldsymbol{v}_h)_{L^2(\partial\Omega)}$ includes the contribution of the weakly enforced IBC, studied below.

4.2. Admissibility conditions for an impedance numerical flux

On a part of the boundary $\Gamma := \partial\Omega$ denoted Γ_z, the IBC is weakly enforced through a centered flux

$$(A(\boldsymbol{n})\boldsymbol{v})^* := \frac{1}{2}A(\boldsymbol{n})(\boldsymbol{v} + \boldsymbol{v}^g), \tag{39}$$

where $\boldsymbol{v}^g$ is the so-called ghost state that needs to be suitably defined as a function of $\boldsymbol{v}$ and $\mathcal{Z}$, $\mathcal{Y}$, or $\mathcal{B}$. A systematic derivation of the possible expressions for $A(\boldsymbol{n})\boldsymbol{v}^g$ is carried out in Sec. 4.4 with an energy analysis formalized through the so-called admissibility and continuity conditions defined below. Recall that the spatial discretization is said to be consistent if for $\boldsymbol{v}(t) \in V$ the exact solution, $(\mathcal{A}_h\boldsymbol{v}, \boldsymbol{w}_h)_{L^2(\Omega)} = (\mathcal{A}\boldsymbol{v}, \boldsymbol{w}_h)_{L^2(\Omega)}$ for all $\boldsymbol{w}_h \in V_h$.

Remark 15. The ghost state $\boldsymbol{v}^g$ is a function known in closed-form and in this paper the numerical flux (39) is enforced without adding computational nodes outside of Ω: the terminology "ghost state" is chosen for its intuitive nature, and does not imply that "ghost nodes" or "ghost cells" are used whatsoever.

Definition 16 *(Admissibility).* The impedance numerical flux (39), uniquely determined by the expression of $A(\boldsymbol{n})\boldsymbol{v}^g$, is said to be *admissible* if it is both consistent and passive.

- (Consistency) Let $\boldsymbol{v}(t) \in V$ be the exact solution (in particular, it does obey the IBC). The consistency condition reads $(A(\boldsymbol{n})\boldsymbol{v})^* = A(\boldsymbol{n})\boldsymbol{v}$ or equivalently

$$A(\boldsymbol{n})\boldsymbol{v}^g = A(\boldsymbol{n})\boldsymbol{v}. \tag{40}$$

- (Passivity) Let $\boldsymbol{v}_h(t) \in V_h$ (in particular, it does *not* obey the IBC). The passivity condition reads

$$\forall t > 0,\ \int_0^t \left((A(\boldsymbol{n})\boldsymbol{v}_h)^* - \frac{1}{2}A(\boldsymbol{n})\boldsymbol{v}_h, \boldsymbol{v}_h\right)_{L^2(\Gamma_z)} \mathrm{d}\tau = \frac{1}{2}\int_0^t (A(\boldsymbol{n})\boldsymbol{v}_h^g, \boldsymbol{v}_h)_{L^2(\Gamma_z)}\,\mathrm{d}\tau \geq 0. \tag{41}$$

The passivity condition is to be understood in light of the semi-discrete energy balance (38), see Example 24 for a numerical illustration of its necessity. In addition to these two admissibility conditions, the two following continuity properties are also computationally desirable.

- (Hard-wall continuity) As "$\mathcal{Z} \to \infty$" (or "$\mathcal{Y} \to 0$", or "$\mathcal{B} \to \mathcal{I}$"), a hard wall ($\boldsymbol{u}\cdot\boldsymbol{n} = 0$) is recovered without singularity, which can be written formally as

$$\lim_{\mathcal{Z}\to\infty} A(\boldsymbol{n})\boldsymbol{v}^g = M_{\mathrm{hw}}(\boldsymbol{n})\boldsymbol{v},\ M_{\mathrm{hw}}(\boldsymbol{n}) := c_0\begin{bmatrix} 2\zeta\boldsymbol{n}\otimes\boldsymbol{n} & \boldsymbol{n} \\ -\boldsymbol{n}^\intercal & 0 \end{bmatrix} \tag{42}$$

  and ζ is an arbitrary non-negative parameter.
- (Pressure-release continuity) As "$\mathcal{Z} \to 0$" (or "$\mathcal{Y} \to \infty$", or "$\mathcal{B} \to -\mathcal{I}$"), a pressure-release boundary ($\tilde{p} = 0$) is recovered without singularity, i.e.

$$\lim_{\mathcal{Z}\to 0} A(\boldsymbol{n})\boldsymbol{v}^g = M_{\mathrm{pr}}(\boldsymbol{n})\boldsymbol{v},\ M_{\mathrm{pr}}(\boldsymbol{n}) := c_0\begin{bmatrix} 0_{n,n} & -\boldsymbol{n} \\ \boldsymbol{n}^\intercal & 2\zeta \end{bmatrix} \tag{43}$$

  and ζ is an arbitrary non-negative parameter.

It is straightforward to verify that $A(\boldsymbol{n})\boldsymbol{v}^g := M_{\mathrm{hw/pr}}(\boldsymbol{n})\boldsymbol{v}$ respects the consistency (40) and passivity (41) conditions stated in Definition 16. The given expressions $M_{\mathrm{hw}}(\boldsymbol{n})$ and $M_{\mathrm{pr}}(\boldsymbol{n})$, or variations thereof, are common in the literature [67, § 5.3] [66, § 7.1.2] [69, § 7.1]. The ability to recover both the hard-wall and pressure-release cases is of particular interest when performing an inverse method on the IBC where the parameter space needs to be explored.

Remark 17. Note that at this stage no assumption is made regarding the time-domain discretization of the IBC: Definition 16 is purely semi-discrete.

The application of the energy analysis to generic nonlinear IBCs, which leads to the derivation of the $\mathcal{Z}$, $\mathcal{Y}$, and $\mathcal{B}$ fluxes, is done in Sec. 4.4. For the sake of clarity, the elementary case of a proportional impedance $\mathcal{Z}(\boldsymbol{u}\cdot\boldsymbol{n}) \propto \boldsymbol{u}\cdot\boldsymbol{n}$ is first fully worked out in Sec. 4.3. In spite of its simplicity, this example provides an intuitive understanding of the computational advantage of the scattering operator $\mathcal{B}$.

4.3. Weak enforcement of proportional impedance boundary conditions

This section focuses on the computational properties of numerical fluxes for the so-called proportional impedance $z_0^{-1}z(t) = a_0\delta(t)$ with $a_0 > 0$ ($\tilde{p} = a_0\boldsymbol{u}\cdot\boldsymbol{n}$). (From Proposition 3 it is admissible.) To weakly enforce the IBC (2) using the numerical flux (39), the ghost state $\boldsymbol{v}^g$ is sought as linearly dependent upon $\boldsymbol{v}$

$$\boldsymbol{v}^g := \begin{bmatrix} \alpha_3\boldsymbol{n}\otimes\boldsymbol{n} & \alpha_4\boldsymbol{n} \\ \alpha_1\boldsymbol{n}^\intercal & \alpha_2 \end{bmatrix}\boldsymbol{v},\ A(\boldsymbol{n})\boldsymbol{v}^g = c_0\begin{bmatrix} \tilde{p}^g\boldsymbol{n} \\ \boldsymbol{u}^g\cdot\boldsymbol{n} \end{bmatrix} = M_0(\boldsymbol{n})\boldsymbol{v}, \tag{44}$$

where

$$M_0(\boldsymbol{n}) = c_0\begin{bmatrix} \alpha_1\boldsymbol{n}\otimes\boldsymbol{n} & \alpha_2\boldsymbol{n} \\ \alpha_3\boldsymbol{n}^\intercal & \alpha_4 \end{bmatrix}. \tag{45}$$

To obtain an admissible flux from this generic expression, two of the four degrees of freedom (DoF) must be removed, as summarized in the proposition below.

Proposition 18. *The numerical flux function given by (39), (44) is admissible if and only if $\alpha_1 = (1-\alpha_2)a_0$ and $\alpha_4 = (1-\alpha_3)/a_0$, with $\alpha_2 \le 1$, $\alpha_3 \le 1$, and $(\alpha_2+\alpha_3)^2 \le 4(1-\alpha_2)(1-\alpha_3)$.*

Proof. The proof is elementary and consists in using the admissibility conditions. (Consistency) Let $\boldsymbol{v} = [\boldsymbol{u}^\intercal, \tilde{p}]^\intercal$ be the exact solution. The consistency condition (40) reads

$$\begin{bmatrix} \alpha_1\boldsymbol{n}\otimes\boldsymbol{n} & (\alpha_2-1)\boldsymbol{n} \\ (\alpha_3-1)\boldsymbol{n}^\intercal & \alpha_4 \end{bmatrix}\boldsymbol{v} = 0.$$

The fact that $\boldsymbol{v}$ obeys the IBC $\tilde{p} = a_0\boldsymbol{u}\cdot\boldsymbol{n}$ readily leads to $\alpha_1 = (1-\alpha_2)a_0$ and $\alpha_4 = (1-\alpha_3)/a_0$, so that the two DoF left are α_2 and α_3. (Passivity) Let $\boldsymbol{v}_h \in V_h$. Since $(M_0(\boldsymbol{n})\boldsymbol{v}_h, \boldsymbol{v}_h)_{\mathbb{R}^{n+1}} = (\check{M}_0\check{\boldsymbol{v}}_h, \check{\boldsymbol{v}}_h)_{\mathbb{R}^2}$ with $\check{\boldsymbol{v}}_h = [\,\boldsymbol{u}_h\cdot\boldsymbol{n}\ \ \tilde{p}_h\,]^\intercal$ and

$$\check{M}_0 := \begin{bmatrix} \alpha_1 & \frac{\alpha_2+\alpha_3}{2} \\ \frac{\alpha_2+\alpha_3}{2} & \alpha_4 \end{bmatrix}, \tag{46}$$

the condition (41) holds if and only if $\check{M}_0$ is positive semidefinite. The inequalities on α_2 and α_3 follow from the application of the following elementary lemma that is frequently used in the remainder of this paper.

Lemma 19. *A 2×2 symmetric matrix $\begin{bmatrix} u & v \\ v & w \end{bmatrix}$ is positive semidefinite if and only if $v^2 \le uw$ and $u+w \ge 0$.*

Proof. A symmetric matrix Σ is positive semidefinite if and only if $\det\Sigma \ge 0$ and $\operatorname{tr}\Sigma \ge 0$. (Product and sum of the two real eigenvalues.) □

□

Remark 20. In the case of a proportional impedance, the consistency (40) and passivity (41) conditions are the (DG1) and (DG2) properties stated in [67] and needed for the error analysis.

Therefore, after examination of the admissibility conditions there are two remaining DoF, α_2 and α_3, so that

$$\boldsymbol{v}^g := \begin{bmatrix} \alpha_3\boldsymbol{n}\otimes\boldsymbol{n} & \frac{1-\alpha_3}{a_0}\boldsymbol{n} \\ (1-\alpha_2)a_0\boldsymbol{n}^\intercal & \alpha_2 \end{bmatrix}\boldsymbol{v},\ M_0(\boldsymbol{n}) = c_0\begin{bmatrix} (1-\alpha_2)a_0\boldsymbol{n}\otimes\boldsymbol{n} & \alpha_2\boldsymbol{n} \\ \alpha_3\boldsymbol{n}^\intercal & \frac{1-\alpha_3}{a_0} \end{bmatrix}. \tag{47}$$

Further constraints can be obtained by considering the continuity conditions (42) and (43):

$$\lim_{a_0\to 0}\alpha_2 = -1, \qquad \lim_{a_0\to 0}\alpha_3 = 1, \qquad \lim_{a_0\to\infty}\alpha_2 = 1, \qquad \lim_{a_0\to\infty}\alpha_3 = -1, \tag{48}$$

$$\lim_{a_0\to 0}(1-\alpha_2)a_0 = 0,\ \lim_{a_0\to 0}(1-\alpha_3)\frac{1}{a_0} \ge 0,\ \lim_{a_0\to\infty}(1-\alpha_2)a_0 \ge 0,\ \lim_{a_0\to\infty}(1-\alpha_3)\frac{1}{a_0} = 0. \tag{49}$$

The line (48) suggests defining $\alpha := \alpha_2$ with $\alpha_3 = -\alpha$, which leads to the α-flux

$$\boldsymbol{v}^g := \begin{bmatrix} -\alpha\boldsymbol{n}\otimes\boldsymbol{n} & \frac{(1+\alpha)}{a_0}\boldsymbol{n} \\ (1-\alpha)a_0\boldsymbol{n}^\intercal & \alpha \end{bmatrix}\boldsymbol{v},\ M_0(\boldsymbol{n}) = c_0\begin{bmatrix} (1-\alpha)a_0\boldsymbol{n}\otimes\boldsymbol{n} & \alpha\boldsymbol{n} \\ -\alpha\boldsymbol{n}^\intercal & \frac{1+\alpha}{a_0} \end{bmatrix}. \tag{50}$$

Any flux of this form is admissible, as long as $\alpha \in [-1,1]$. To respect the remaining continuity conditions (49), one can choose $\alpha = \beta_0 := (a_0-1)/(a_0+1)$, which yields the β_0-flux

$$\boldsymbol{v}^g := \begin{bmatrix} -\beta_0 \boldsymbol{n}\otimes\boldsymbol{n} & (1-\beta_0)\boldsymbol{n} \\ (1+\beta_0)\boldsymbol{n}^\intercal & \beta_0 \end{bmatrix} \boldsymbol{v},\ M_0(\boldsymbol{n}) = c_0 \begin{bmatrix} (1+\beta_0)\boldsymbol{n}\otimes\boldsymbol{n} & \beta_0\boldsymbol{n} \\ -\beta_0\boldsymbol{n}^\intercal & 1-\beta_0 \end{bmatrix}, \tag{51}$$

an apparent computational interest of which is the boundedness of its components with respect to a_0. In summary, application of the admissibility and continuity conditions leads to (51), an expression that, to the best of the authors' knowledge, was first proposed by Ventribout [49, § 1.3.2] with a view on application to optimal control. Further insights into the benefit of choosing $\alpha = \beta_0$ can be obtained by deriving a CFL stability condition.

For simplicity, let us consider the explicit Euler scheme

$$\boldsymbol{v}_h^{n+1} - \boldsymbol{v}_h^n + \Delta t \tilde{\mathcal{A}}_h \boldsymbol{v}_h^n + \Delta t \mathcal{A}_h^{\{0\}} \boldsymbol{v}_h^n = 0, \tag{52}$$

with constant time step Δt and CFL number defined as $\mathrm{CFL} := \Delta t c_0 h^{-1}$. To highlight the IBC contribution, the decomposition $\mathcal{A}_h \boldsymbol{v}_h = \tilde{\mathcal{A}}_h \boldsymbol{v}_h + \mathcal{A}_h^{\{0\}} \boldsymbol{v}_h$ is used, where $\mathcal{A}_h^{\{0\}} : V_h \to V_h$ is the boundary term of $\mathcal{A}_h$ given by, assuming that the IBC is applied on the whole of Γ (i.e. $\Gamma_z = \partial\Omega$),

$$(\mathcal{A}_h^{\{0\}} \boldsymbol{v}_h, \boldsymbol{w}_h)_{L^2(\Omega)} = \frac{1}{2}(M_0(\boldsymbol{n})\boldsymbol{v}_h - A(\boldsymbol{n})\boldsymbol{v}_h, \boldsymbol{w}_h)_{L^2(\partial\Omega)}, \tag{53}$$

so that

$$(\tilde{\mathcal{A}}_h \boldsymbol{v}_h, \boldsymbol{w}_h)_{L^2(\Omega)} := \sum_{T\in\mathcal{T}_h} (\mathcal{A}\boldsymbol{v}_h, \boldsymbol{w}_h)_{L^2(T)} - \sum_{F\in\mathcal{F}_h^i} (A(\boldsymbol{n}_F)[\![\boldsymbol{v}_h]\!], \{\boldsymbol{w}_h\})_{L^2(F)} + \frac{1}{2}\sum_{F\in\mathcal{F}_h^i} (|A(\boldsymbol{n}_F)|[\![\boldsymbol{v}_h]\!], [\![\boldsymbol{w}_h]\!])_{L^2(F)}. \tag{54}$$

Using a discrete energy method (see Appendix C), the following sufficient stability condition can be derived.

Proposition 21. *Assume $\nabla \boldsymbol{u_0} = 0$ (uniform base flow) and $V_h = \mathbb{P}_n^0(\mathcal{T}_h)^{n+1}$ (finite volume discretization). A sufficient L^2 stability condition for (52) is $\mathrm{CFL} \le 2^{-1} C_{\mathrm{DG}}^{-2} \left(1 + \frac{|\boldsymbol{u_0}|}{c_0}\right)^{-1}$ and*

$$\begin{cases} \alpha_1 + \alpha_4 \ge C_{\mathrm{tr}}^2 \mathrm{CFL}(\alpha_1^2 + (\alpha_3-1)^2 + \alpha_4^2 + (\alpha_2-1)^2) \\ (\alpha_2+\alpha_3)^2 \le 4\left(\alpha_1 - C_{\mathrm{tr}}^2\mathrm{CFL}(\alpha_1^2+(\alpha_3-1)^2)\right)\left(\alpha_4 - C_{\mathrm{tr}}^2\mathrm{CFL}(\alpha_4^2+(\alpha_2-1)^2)\right), \end{cases} \tag{55}$$

where the positive constants C_{DG} and C_{tr}, defined in Lemmas 31 and 33, are non-dimensional and do not depend upon the initial data or the impedance.

Remark 22. Recall that, to be admissible, the matrix $M_0(\boldsymbol{n})$ given by (45) must obey Proposition 18. In particular, the passivity condition (41) requires the conditions $\alpha_1 + \alpha_4 \ge 0$ and $(\alpha_2+\alpha_3)^2 \le 4\alpha_1\alpha_4$ that are *less* stringent than (55).

The interest of Proposition 21 lies in the condition (55) that gives the influence of the numerical flux on the CFL number. Let us highlight three particular cases of practical interest by considering the α-flux ((39), (50)) with $\alpha \in [-1, 1]$, which has been derived above.

- (1-flux) If $\alpha = 1$ ($\alpha_1 = 0$), then $\tilde{p}^g = \tilde{p}$ and the flux does not control $\boldsymbol{u}_h \cdot \boldsymbol{n}$ at the impedance boundary since $(M_0(\boldsymbol{n})\boldsymbol{v}_h, \boldsymbol{v}_h)_{\mathbb{R}^{n+1}} = 2c_0 a_0^{-1} \tilde{p}_h^2$. A stability condition, namely $\mathrm{CFL} \le C_{\mathrm{tr}}^{-2}\alpha_4/(1+\alpha_4^2)$, can be obtained from (55) if and only if $\alpha_2 = -1$ and $\alpha_3 = 1$. But since $\alpha_2 = \alpha = 1$, the scheme is not provably stable with the proposed energy analysis.
- (-1-flux) If $\alpha = -1$ ($\alpha_4 = 0$), then $\boldsymbol{u}^g = (\boldsymbol{u}\cdot\boldsymbol{n})\boldsymbol{n}$ and the numerical flux does not control $\tilde{p}_h$ since $(M_0(\boldsymbol{n})\boldsymbol{v}_h, \boldsymbol{v}_h)_{\mathbb{R}^{n+1}} = 2c_0 a_0 (\boldsymbol{u}_h \cdot \boldsymbol{n})^2$. Similarly, a stability condition cannot be obtained from Proposition 21 since that would require $\alpha_2 = 1$ and $\alpha_3 = -1$, values at odds with the definition of the α-flux with $\alpha = -1$.
- (β_0-flux) The α-flux satisfies $(M_0(\boldsymbol{n})\boldsymbol{v}_h, \boldsymbol{v}_h)_{\mathbb{R}^{n+1}} = c_0 a_0 (1-\alpha)(\boldsymbol{u}_h\cdot\boldsymbol{n})^2 + c_0 a_0^{-1}(1+\alpha)\tilde{p}_h^2$ and thus control both $\boldsymbol{u}_h\cdot\boldsymbol{n}$ and $\tilde{p}_h$ if $\alpha \in (-1, 1)$. Under this assumption, the stability condition is given by (55) with $\alpha_1 = (1-\alpha)a_0$, $\alpha_4 = (1+\alpha)a_0^{-1}$, and $\alpha_2 = \alpha = -\alpha_3$. The β_0-flux ((39), (51)) yields

  $$\mathrm{CFL} \le \frac{1}{C_{\mathrm{tr}}^2} \min\left[\frac{1}{1+\beta_0^2}, \frac{1}{2(1+\beta_0)}, \frac{1}{2(1-\beta_0)}\right], \tag{56}$$

  which shows that the CFL number has a positive upper bound with respect to a_0, namely $\mathrm{CFL} \le 4^{-1} C_{\mathrm{tr}}^{-2}$. By contrast, consider the 0-flux ($\alpha_2 = \alpha_3 = 0$) which yields

  $$\mathrm{CFL} \le \frac{1}{C_{\mathrm{tr}}^2} \frac{a_0}{1+a_0^2},$$

  so that the CFL number decreases to 0 as $a_0 \to \infty$ or $a_0 \to 0$. This recovers a result of Ventribout [49, § 2.3].

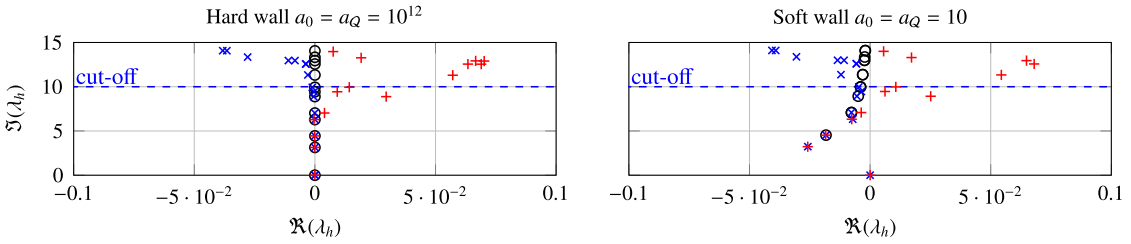

Fig. 2. Eigenvalues $\lambda_h \in \sigma(-\mathcal{A}_h)$ for the acoustical cavity $\Omega = (0,1)^2$ with $c_0 = 1$, $z_0 = 1$, and impedance $\mathcal{Z}(\boldsymbol{u}\cdot\boldsymbol{n}) = a_0\boldsymbol{u}\cdot\boldsymbol{n} + a_{\mathcal{Q}}\dot{\boldsymbol{u}}\cdot\boldsymbol{n}$ on $\partial\Omega$. DG6 ($N_K = 8$ triangles, 504 DoF). (×): $\mathcal{Z}$-flux ((39), (59)). (+): flux ((39), (60)) with $\alpha = \beta_0$. (○): $\lambda = \mathrm{j}\omega = \pm\mathrm{j}c_0\sqrt{k_1^2 + k_2^2}$ with two monodimensional dispersion relations $\Delta_{1D}(k_i, \hat{z}(\mathrm{j}\omega), \omega) = 0$ (only covers eigenfunctions with separated variables).

In conclusion, among the admissible α-fluxes ((39), (50)) with $\alpha \in [-1, 1]$, the β_0-flux ((39), (51)) is the optimal choice since its components are bounded with respect to $a_0 \in [0, \infty]$, it controls both $\tilde{p}_h$ and $\boldsymbol{u}_h\cdot\boldsymbol{n}$, and delivers the CFL stability condition (56). Extension of this result to nonlinear scattering operators $\mathcal{B}$ is done next in Sec. 4.4.

4.4. Weak enforcement of nonlinear impedance boundary conditions

Let us now consider the generic, possibly nonlinear, IBC under the three forms defined in Sec. 2.2

$$\tilde{p} = a_0\boldsymbol{u}\cdot\boldsymbol{n} + a_{\mathcal{Q}}\mathcal{Q}(\boldsymbol{u}\cdot\boldsymbol{n}) \quad (a) \qquad \boldsymbol{u}\cdot\boldsymbol{n} = a_0\tilde{p} + a_{\mathcal{Q}}\mathcal{Q}(\tilde{p}) \quad (b) \qquad \tilde{p} - \boldsymbol{u}\cdot\boldsymbol{n} = \mathcal{B}(\tilde{p} + \boldsymbol{u}\cdot\boldsymbol{n}) \quad (c), \tag{57}$$

where $a_0 > 0$, $a_{\mathcal{Q}} \geq 0$, $\mathcal{Q}$ is an admissible impedance operator (see Definition 1), and $\mathcal{B}$ is an admissible scattering operator (see Definition 6). Following the method of Sec. 4.3, Secs. 4.4.1 and 4.4.2 derive the admissible numerical flux for each form ((57a), (57b), (57c)), namely the $\mathcal{Z}$-flux ((39), (59)), $\mathcal{Y}$-flux ((39), (61)), and the $\mathcal{B}$-flux ((39), (63)), and establish the superiority of the $\mathcal{B}$-flux.

Remark 23. For the analysis presented below, the IBCs (57) are only assumed to be admissible. In particular, they need not be given by one of the models covered in Sec. 3, so that Secs. 3 and 4.4 are independent.

4.4.1. Numerical flux based on the impedance or the admittance

To weakly enforce the IBC (57a) (impedance operator $z_0^{-1}\mathcal{Z}(\boldsymbol{u}\cdot\boldsymbol{n}) = a_0\boldsymbol{u}\cdot\boldsymbol{n} + a_{\mathcal{Q}}\mathcal{Q}(\boldsymbol{u}\cdot\boldsymbol{n})$), the ghost state is sought as

$$A(\boldsymbol{n})\boldsymbol{v}^g = M_0(\boldsymbol{n})\boldsymbol{v} + \boldsymbol{m}_{\mathcal{Q}}(\boldsymbol{n})\mathcal{Q}(\boldsymbol{u}\cdot\boldsymbol{n}), \tag{58}$$

where $M_0(\boldsymbol{n})$ is given by (45) and $\boldsymbol{m}_{\mathcal{Q}}(\boldsymbol{n}) = c_0[\gamma_1\boldsymbol{n}^\mathsf{T}, \gamma_2]^\mathsf{T}$. Proposition 25 shows that the only admissible expression is

$$A(\boldsymbol{n})\boldsymbol{v}^g = c_0\begin{bmatrix} 2a_0\boldsymbol{n}\otimes\boldsymbol{n} & -\boldsymbol{n} \\ \boldsymbol{n}^\mathsf{T} & 0 \end{bmatrix}\boldsymbol{v} + c_0\begin{bmatrix} 2a_{\mathcal{Q}}\boldsymbol{n} \\ 0 \end{bmatrix}\mathcal{Q}(\boldsymbol{u}\cdot\boldsymbol{n}), \tag{59}$$

where there are no remaining DoF. The $\mathcal{Z}$-flux ((39), (59)) fulfills the pressure-release continuity condition (43) but not the hard-wall one (42) since there is a singularity as $a_i \to \infty$. Moreover, note that $(M_0(\boldsymbol{n})\boldsymbol{v}_h, \boldsymbol{v}_h)_{\mathbb{R}^{n+1}} = 2c_0a_0(\boldsymbol{u}_h\cdot\boldsymbol{n})^2$ so that there is no control of $\tilde{p}_h^2$ at the impedance boundary, a phenomenon already encountered in Sec. 4.3.

Example 24. One may think that the result of Proposition 25 is unnecessarily stringent, i.e. that the admissibility conditions proposed in Definition 16 are too constraining, but it can be verified numerically that it is not so. Let us consider the acoustical cavity $\Omega = (0,1)^2$ with $c_0 = 1$, $z_0 = 1$, and impedance $\mathcal{Z}(\boldsymbol{u}\cdot\boldsymbol{n}) = a_0\boldsymbol{u}\cdot\boldsymbol{n} + a_{\mathcal{Q}}\dot{\boldsymbol{u}}\cdot\boldsymbol{n}$ applied to the whole of $\partial\Omega$. Two dispersion relations $\Delta_{1D}(k_i, \hat{z}(\mathrm{j}\omega), \omega)$ can be derived for eigenfunctions with separated variables $\tilde{p}(\boldsymbol{x}) = \tilde{p}_1(x_1)\tilde{p}_2(x_2)$ with $\tilde{p}_i(x_i) = (A_ie^{\mathrm{j}k_ix_i} + B_ie^{-\mathrm{j}k_ix_i})$ (note that it does not provide all the eigenvalues if $\hat{z}(s) \neq +\infty$). Fig. 2 plots the eigenvalues computed with a sixth-order DG method (see Appendix D) and flux

$$A(\boldsymbol{n})\boldsymbol{v}^g = c_0\begin{bmatrix} (1-\alpha)a_0\boldsymbol{n}\otimes\boldsymbol{n} & \alpha\boldsymbol{n} \\ -\alpha\boldsymbol{n}^\mathsf{T} & \frac{1+\alpha}{a_0} \end{bmatrix}\boldsymbol{v} + c_0\begin{bmatrix} (1-\alpha)a_{\mathcal{Q}}\boldsymbol{n} \\ -(1+\alpha)\frac{a_{\mathcal{Q}}}{a_0} \end{bmatrix}\mathcal{Q}(\boldsymbol{u}\cdot\boldsymbol{n}), \tag{60}$$

with reduces to the α-flux ((39), (50)) if $a_{\mathcal{Q}} = 0$. The value $\alpha = -1$ yields stable eigenvalues that match the exact ones until a cut-off frequency. However, for $\alpha = \beta_0$, eigenfunctions have a less pronounced decay and can even be unstable. Hence *the impedance model $\mathcal{Z}$ is passive, but passivity is lost at the semi-discrete level.* This conforms with the fact that the flux ((39), (60)) is consistent for any α but passive if and only if $\alpha = -1$ from Proposition 25.

Proposition 25. *The numerical flux function ((39), (58)) is admissible if and only if the ghost state is given by (59).*

Proof. Consistency and passivity conditions are checked. (Consistency) The condition (40) yields $\alpha_1 = (1-\alpha_2)a_0$, $\alpha_4 = (1-\alpha_3)/a_0$, $\gamma_1 = (1-\alpha_2)a_1$, and $\gamma_2 = -(1-\alpha_3)\frac{a_{\mathcal{Q}}}{a_0}$. (Passivity) Let $\boldsymbol{v}_h \in V_h$. We have

$$(A(\boldsymbol{n})\boldsymbol{v}_h^g, \boldsymbol{v}_h)_{\mathbb{R}^{n+1}} = (M_0(\boldsymbol{n})\boldsymbol{v}_h, \boldsymbol{v}_h)_{\mathbb{R}^{n+1}} + c_0(1-\alpha_2)a_{\mathcal{Q}}\mathcal{Q}(\boldsymbol{u}_h\cdot\boldsymbol{n})\boldsymbol{u}_h\cdot\boldsymbol{n} - c_0(1-\alpha_3)\frac{a_{\mathcal{Q}}}{a_0}\mathcal{Q}(\boldsymbol{u}_h\cdot\boldsymbol{n})\tilde{p}_h.$$

The passivity condition (41) holds true for any $\boldsymbol{v}_h$ and $\mathcal{Q}$ if and only if $(M_0(\boldsymbol{n})\boldsymbol{v}_h, \boldsymbol{v}_h)_{\mathbb{R}^{n+1}} \geq 0$, $(1-\alpha_2)a_{\mathcal{Q}} \geq 0$, and $\alpha_3 = 1$. Lemma 19 gives $\alpha_2 = -1$ and enables to conclude. □

The admittance case (57b) is identical, as an application of the admissibility conditions shows that the only admissible ghost state of the form $A(\boldsymbol{n})\boldsymbol{v}^g = M_0(\boldsymbol{n})\boldsymbol{v} + \boldsymbol{m}_{\mathcal{Q}}(\boldsymbol{n})\mathcal{Q}(\tilde{p})$ is given by

$$A(\boldsymbol{n})\boldsymbol{v}^g = c_0\begin{bmatrix} 0_{n,n} & \boldsymbol{n} \\ -\boldsymbol{n}^\intercal & 2a_0 \end{bmatrix}\boldsymbol{v} + c_0\begin{bmatrix} \boldsymbol{0_n} \\ 2a_{\mathcal{Q}} \end{bmatrix}\mathcal{Q}(\tilde{p}), \tag{61}$$

which obeys the hard-wall continuity condition (42) but not the pressure-release one (43). Note that $(M_0(\boldsymbol{n})\boldsymbol{v}_h, \boldsymbol{v}_h)_{\mathbb{R}^{n+1}} = 2c_0a_0\tilde{p}_h^2$ so that there is no control of $(\boldsymbol{u}_h\cdot\boldsymbol{n})^2$ at the impedance boundary. In view of the expressions (59) and (61), the fluxes based on impedance and admittance have symmetrical continuity properties such that the $\mathcal{Z}$ (resp. $\mathcal{Y}$)-flux should be preferred to the $\mathcal{Y}$ (resp. $\mathcal{Z}$)-flux when the impedance is close to a pressure-release wall (resp. hard wall). However, the next section shows these two fluxes are trumped by a flux based on the scattering operator $\mathcal{B}$.

4.4.2. Numerical flux based on the scattering operator

To weakly enforce the IBC under its scattering formulation (57c), the ghost state is sought as

$$A(\boldsymbol{n})\boldsymbol{v}^g = M_0(\boldsymbol{n})\boldsymbol{v} + \boldsymbol{m}_{\mathcal{B}}(\boldsymbol{n})\mathcal{B}(\tilde{p} + \boldsymbol{u}\cdot\boldsymbol{n}), \tag{62}$$

where $M_0(\boldsymbol{n})$ is given by (45) and $\boldsymbol{m}_{\mathcal{B}}(\boldsymbol{n}) = c_0[\gamma_1\boldsymbol{n}^\intercal, \gamma_2]^\intercal$. Proposition 27 below shows that the only admissible ghost state is given by

$$A(\boldsymbol{n})\boldsymbol{v}^g = c_0\begin{bmatrix} \boldsymbol{n}\otimes\boldsymbol{n} & \boldsymbol{0_n} \\ \boldsymbol{0_n}^\intercal & 1 \end{bmatrix}\boldsymbol{v} + c_0\begin{bmatrix} \boldsymbol{n} \\ -1 \end{bmatrix}\mathcal{B}(\tilde{p} + \boldsymbol{u}\cdot\boldsymbol{n}). \tag{63}$$

Note that with this flux there is control of both $\boldsymbol{u}_h\cdot\boldsymbol{n}$ and $\tilde{p}_h$ at the boundary, and the boundary dissipation term is

$$\begin{aligned}\frac{1}{2}\int_0^t (A(\boldsymbol{n})\boldsymbol{v}_h^g, \boldsymbol{v}_h)_{L^2(\Gamma_z)}\,\mathrm{d}\tau = \frac{c_0}{4}\int_0^t \big(\|\tilde{p}_h + \boldsymbol{u}_h\cdot\boldsymbol{n}\|_{L^2(\Gamma_z)}^2 - \|\mathcal{B}(\tilde{p}_h + \boldsymbol{u}_h\cdot\boldsymbol{n})\|_{L^2(\Gamma_z)}^2\big)\,\mathrm{d}\tau \\ + \frac{c_0}{4}\int_0^t \|\tilde{p}_h - \boldsymbol{u}_h\cdot\boldsymbol{n} - \mathcal{B}(\tilde{p}_h + \boldsymbol{u}_h\cdot\boldsymbol{n})\|_{L^2(\Gamma_z)}^2\,\mathrm{d}\tau,\end{aligned} \tag{64}$$

where the two terms on the right-hand side have a clear interpretation. The first one is the dissipation associated with the scattering operator $\mathcal{B}$, see the passivity condition (9), and the second one can be interpreted as a penalization term for the non-respect of the IBC.

Remark 26. The $\mathcal{B}$-flux ((39), (63)) derived from the energy analysis carried out in the proof of Proposition 27 reads

$$(A(\boldsymbol{n})\boldsymbol{v})^* = \frac{c_0}{2}\begin{bmatrix} \boldsymbol{n} \\ 1 \end{bmatrix}(\tilde{p} + \boldsymbol{u}\cdot\boldsymbol{n}) + \frac{c_0}{2}\begin{bmatrix} \boldsymbol{n} \\ -1 \end{bmatrix}\mathcal{B}(\tilde{p} + \boldsymbol{u}\cdot\boldsymbol{n}).$$

It is interesting to note that this flux is exactly that derived using flux vector splitting [70, Chap. 8], which for a linear hyperbolic PDE with constant coefficients amounts to exactly solving the monodimensional Riemann problem at the boundary. Indeed, given Assumption 10 we have at the impedance boundary Γ_z

$$\begin{aligned}A(\boldsymbol{n})\boldsymbol{v} &= A(\boldsymbol{n})^{\oplus}\boldsymbol{v} - A(\boldsymbol{n})^{\ominus}\boldsymbol{v} = \frac{c_0}{2}\begin{bmatrix} \boldsymbol{n}\otimes\boldsymbol{n} & \boldsymbol{n} \\ \boldsymbol{n}^\intercal & 1 \end{bmatrix}\boldsymbol{v} + \frac{c_0}{2}\begin{bmatrix} -\boldsymbol{n}\otimes\boldsymbol{n} & \boldsymbol{n} \\ \boldsymbol{n}^\intercal & -1 \end{bmatrix}\boldsymbol{v} \\ &= \frac{c_0}{2}\begin{bmatrix} \boldsymbol{n} \\ 1 \end{bmatrix}(\tilde{p} + \boldsymbol{u}\cdot\boldsymbol{n}) + \frac{c_0}{2}\begin{bmatrix} \boldsymbol{n} \\ -1 \end{bmatrix}(\tilde{p} - \boldsymbol{u}\cdot\boldsymbol{n}).\end{aligned}$$

Therefore, this flux has a direct interpretation based on characteristics, making it natural to use with a hyperbolic law.

Proposition 27. *The numerical flux ((39), (62)) is admissible if and only if the ghost state is given by (63).*

Proof. (Consistency) Condition (40) leads to $\alpha_1 = \gamma_1 = 1-\alpha_2$ and $\alpha_4 = -\gamma_2 = 1-\alpha_3$ so that there are only two DoF left, α_2 and α_3. (Passivity) Let $\boldsymbol{v}_h \in V_h$. Recall that the passivity property of the scattering operator $\mathcal{B}$ reads (9), which makes the study of passivity more intricate than in the previous sections. The generic expressions of $M_0(\boldsymbol{n})$ and $\boldsymbol{m}_{\mathcal{B}}(\boldsymbol{n})$ give

$$\begin{aligned}\frac{1}{c_0}(A(\boldsymbol{n})\boldsymbol{v}_h^g, \boldsymbol{v}_h)_{\mathbb{R}^{n+1}} &= \frac{1}{c_0}(M_0(\boldsymbol{n})\boldsymbol{v}_h, \boldsymbol{v}_h)_{\mathbb{R}^{n+1}} + \frac{1}{c_0}(\boldsymbol{m}_{\mathcal{B}}(\boldsymbol{n})\mathcal{B}(\tilde{p}_h + \boldsymbol{u}_h\cdot\boldsymbol{n}), \boldsymbol{v}_h)_{\mathbb{R}^{n+1}}\\ &= (1-\alpha_2)(\boldsymbol{u}_h\cdot\boldsymbol{n})^2 + (1-\alpha_3)\tilde{p}_h^2 + (\alpha_2+\alpha_3)\tilde{p}_h\boldsymbol{u}_h\cdot\boldsymbol{n}\\ &\quad - \mathcal{B}(\tilde{p}_h + \boldsymbol{u}_h\cdot\boldsymbol{n})\big((1-\alpha_3)\tilde{p}_h - (1-\alpha_2)\boldsymbol{u}_h\cdot\boldsymbol{n}\big).\end{aligned}$$

Using the identity $ab = \frac{1}{2}a^2 + \frac{1}{2}b^2 - \frac{1}{2}(a-b)^2$ on $\mathcal{B}(\tilde{p}_h + \boldsymbol{u}_h\cdot\boldsymbol{n})\big((1-\alpha_3)\tilde{p}_h - (1-\alpha_2)\boldsymbol{u}_h\cdot\boldsymbol{n}\big)$ and collecting the terms yields

$$\begin{aligned}\frac{1}{c_0}(A(\boldsymbol{n})\boldsymbol{v}_h^g, \boldsymbol{v}_h)_{\mathbb{R}^{n+1}} &= \frac{1}{2}(\tilde{p}_h + \boldsymbol{u}_h\cdot\boldsymbol{n})^2 - \frac{1}{2}\mathcal{B}(\tilde{p}_h + \boldsymbol{u}_h\cdot\boldsymbol{n})^2\\ &\quad + \frac{1}{2}\Big((1-\alpha_3)\tilde{p}_h - (1-\alpha_2)\boldsymbol{u}_h\cdot\boldsymbol{n} - \mathcal{B}(\tilde{p}_h + \boldsymbol{u}_h\cdot\boldsymbol{n})\Big)^2 - \frac{1}{2}(\alpha_2\boldsymbol{u}_h\cdot\boldsymbol{n} - \alpha_3\tilde{p}_h)^2.\end{aligned}$$

Since this quantity must be non-negative for every admissible scattering operator $\mathcal{B}$ and every $\boldsymbol{v}_h \in V_h$, the passivity condition (41) is achieved if and only if $\alpha_2 = \alpha_3 = 0$. □

In summary, even for a generic nonlinear scattering operator $\mathcal{B}$, the $\mathcal{B}$-flux ((39), (63)) keeps the properties mentioned when studying the proportional case, such as the control of both $\boldsymbol{u}_h\cdot\boldsymbol{n}$ and $\tilde{p}_h$ at the boundary. Note that this conclusion has been reached without considering *how* $\mathcal{B}$ is computed, i.e. the analysis is so far independent of Sec. 3. However, to conclude this section, it is insightful to derive a CFL stability condition, as in Sec. 4.3. For this, let us consider the following reflection coefficient, inspired by the representation of physical models derived in Sec. 3.2,

$$\hat{\beta}(s) = \int_{\xi^{\min}}^{\xi^{\max}} \frac{1}{s+\xi}\mathrm{d}\mu(\xi), \tag{65}$$

where μ is a measure on $(\xi^{\min}, \xi^{\max})$ with $0 \le \xi^{\min} < \xi^{\max} < \infty$. A sufficient condition for $\hat{\beta}$ to be bounded-real is $\|\mu\|_{L^1}\|\frac{\mu}{\xi^2}\|_{L^1} \le 1$, see Appendix C. The corresponding semi-discrete formulation results from a coupling between the additional variables φ_h and the acoustic field $\boldsymbol{v}$ (space and time variables are explicitly stated to avoid ambiguity)

$$\begin{cases}\partial_t\varphi_h(t,\boldsymbol{x},-\xi) &= -\xi\varphi_h(t,\boldsymbol{x},-\xi) + \tilde{p}_h(t,\boldsymbol{x}) + \boldsymbol{u}_h(t,\boldsymbol{x})\cdot\boldsymbol{n}(\boldsymbol{x}) \quad (x\in\partial\Omega,\ \xi\in[\xi^{\min},\xi^{\max}])\\ \partial_t\boldsymbol{v}_h(t) &= -\tilde{\mathcal{A}}_h\boldsymbol{v}_h(t) - \mathcal{A}_h^{\{0\}}\boldsymbol{v}_h(t) - \mathcal{A}_h^{\{\beta\}}\beta\star(\tilde{p}_h + \boldsymbol{u}_h\cdot\boldsymbol{n})(t).\end{cases} \tag{66}$$

The spatial discretization is given by (53), (54) with an additional boundary contribution $\mathcal{A}_h^{\{\beta\}}$ in the decomposition of $\mathcal{A}_h$ compared to that of Sec. 4.3 given by, assuming that $\Gamma_z = \partial\Omega$,

$$(\mathcal{A}_h^{\{\beta\}}v_h, \boldsymbol{w}_h)_{L^2(\Omega)} := \frac{1}{2}(\boldsymbol{m}_{\mathcal{B}}(\boldsymbol{n})v_h, \boldsymbol{w}_h)_{L^2(\partial\Omega)} = -\frac{c_0}{2}(v_h, (w_h^p - \boldsymbol{w}_h^u\cdot\boldsymbol{n}))_{L^2(\partial\Omega)}. \tag{67}$$

The result, stated in Proposition 28, is a natural extension of Proposition 21 and more specifically of (56). It shows that, with an explicit time integration, the maximum frequency $(2\pi)^{-1}\xi_{\max}$ of the scattering operator stiffens the system; in practice, $\xi_{\max}$ must be chosen consistently with the dissipation and dispersion properties of the spatial discretization, as advocated in Sec. 3.3.1. Numerical applications based on the scattering operator are considered in Secs. 5 and 6.

Proposition 28. *Assume $\nabla\boldsymbol{u_0} = 0$ (uniform base flow), $V_h = \mathbb{P}_n^0(\mathcal{T}_h)^{n+1}$ (finite volume discretization), and $\hat{\beta}$ bounded-real such that $\|\mu\|_{L^1}\|\frac{\mu}{\xi^2}\|_{L^1} \le 1$. A sufficient L^2 stability condition for (66) is*

$$\mathrm{CFL} \le \min\left(\frac{1}{2C_{\mathrm{DG}}^2}\left(1 + \frac{|\boldsymbol{u_0}|}{c_0}\right)^{-1}, \frac{1}{2C_{\mathrm{tr}}^2}, \frac{c_0}{h\,\xi^{\max}}\right), \tag{68}$$

where the positive constants C_{DG} and C_{tr}, defined in Lemmas 32 and 33, are non-dimensional and do not depend upon the initial data or the impedance.

Fig. 3. Impedance tube used in Sec. 5: $L_x = 1\,\mathrm{m}$, $L_y = {}^{L_x}/_{100}$, and mesh with 240 triangles.

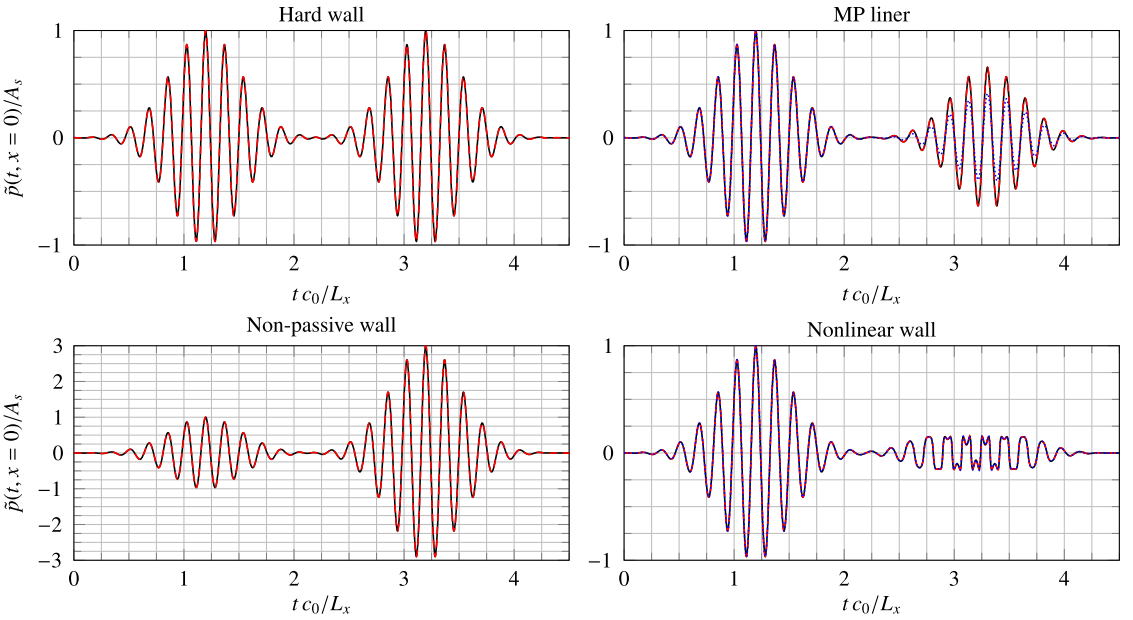

Fig. 4. Acoustic pressure $\tilde{p}$ at $x = 0$ (see Fig. 3). Gaussian-modulated sinusoidal source centered at 2 kHz of amplitude $A_s = \sqrt{2}\frac{p_{\mathrm{ref}}}{z_0}10^{\frac{\mathrm{SPL}}{20}}$ ($L_x = 1\,\mathrm{m}$, $L_y = {}^{L_x}/_{100}$, $c_0 = 344.32\,\mathrm{m.s^{-1}}$, $z_0 = 405.26\,\mathrm{kg.m^{-2}.s^{-1}}$, $p_{\mathrm{ref}} = 2 \times 10^{-5}\,\mathrm{Pa}$, and $\mathrm{SPL} = 192.15\,\mathrm{dB}$). (——) Exact solution (69). (- - - -) DG4-RKF84-$\mathcal{B}$-flux ((39), (63)) and CFL = 0.85. [Top left] Hard wall $\mathcal{B} = \mathcal{I}$. [Bottom left] Non-passive wall $\mathcal{B} = 3\mathcal{I}$. [Bottom right] Nonlinear model (23) with $(a_0, C_{\mathrm{nl}}) = (0, 1)$. (.....) DG4-RKF84-$\mathcal{Z}$-flux ((39), (59)). [Top right] Linear TDIBC $\tilde{\beta}_A$, see Fig. 7 and Table 2. (- - - -) DG4-RKF84-$\mathcal{B}$-flux, $N_\psi = 4$, and $\mathrm{PPW}_{\tilde{\tau}}(2\,\mathrm{kHz}) = 9.64$. (.....) DG4-RKF84-$\mathcal{B}$-flux, $N_\psi = 2$, and $\mathrm{PPW}_{\tilde{\tau}}(2\,\mathrm{kHz}) = 4.82$.

5. Numerical validation with nonlinear impedance tube

This section validates the proposed $\mathcal{Z}$-flux ((39), (59)) and $\mathcal{B}$-flux ((39), (63)), and illustrates the computational advantage of the latter. It is enough to consider the so-called impedance tube since the IBC (2) is monodimensional (i.e. only the normal component $\boldsymbol{u} \cdot \boldsymbol{n}$ is needed at the boundary, which stems from the locally reacting hypothesis). Let us briefly recall the impedance tube exact solution, expressed in the notations of Fig. 3. At $x = 0$ the incoming characteristic is given by $(\tilde{p} + u)(t, 0) = \phi_s(t)$ where ϕ_s is causal (i.e. $\phi_s(t) = 0$ for $t < 0$). The nonlinear IBC (8) is enforced at $x = L_x$. Assuming null initial conditions $\tilde{p}(0, x) = u(0, x) = 0$, the exact solution is

$$\tilde{p}(t,x) = \frac{1}{2}\phi_s\left(t - \frac{x}{c_0}\right) + \frac{1}{2}\mathcal{B}(\phi_s)\left(t - \frac{2L_x - x}{c_0}\right),\ u(t,x) = \frac{1}{2}\phi_s\left(t - \frac{x}{c_0}\right) - \frac{1}{2}\mathcal{B}(\phi_s)\left(t - \frac{2L_x - x}{c_0}\right). \tag{69}$$

Note that the solution, derived with an elementary application of the method of characteristics, is naturally expressed with the nonlinear scattering operator $\mathcal{B}$. If the IBC is linear, then $\mathcal{B}(v) = \beta \star v$ and the analytical solution can also be derived using the Laplace transform. As detailed in Sec. 3, the computation of $\mathcal{B}(\phi_s)$ may involve delayed ODEs.

The LEEs (1) are discretized using a fourth-order DG method (see Appendix D) and the RKF84 eight-stage fourth-order $2N$-storage Runge–Kutta method [71, Tab. A.9]. The mesh of 240 triangles (2400 nodes) is shown in Fig. 3. The source is imposed using the numerical flux $(A(\boldsymbol{n}_F)\boldsymbol{v})^*_s$ (see Sec. 4.1) and the IBC is weakly enforced with the $\mathcal{Z}$-flux ((39), (59)) or the $\mathcal{B}$-flux ((39), (63)). Fig. 4 shows the exact and computed solutions at the inlet $x = 0$ for four impedance models and a Gaussian source centered at 2 kHz. For the sake of clarity, the impedance tube is chosen long enough to avoid overlapping between the incident and reflected waves. For each of the four models the exact solution matches the computed one, which validates the proposed numerical flux functions.

The top right graph covers the linear TDIBC $\tilde{\beta}_A$ given in Table 2 and plotted in Fig. 4 that models the MP liner studied in Sec. 6. The computation of $\tilde{\beta}_A \star v$ through (34) involves a transport equation whose N_ψ-point discretization is characterized by its number of points per wavelength (33): here, $N_\psi = 4$ is sufficient. The bottom left graph covers the *non-passive* scattering operator $\mathcal{B} = 3\mathcal{I}$, outside of the scope of the analysis presented in this paper. However, the $\mathcal{B}$-flux does enable to compute this case, by contrast to the $\mathcal{Z}$-flux with which no stable computations could be obtained, even with a reduced

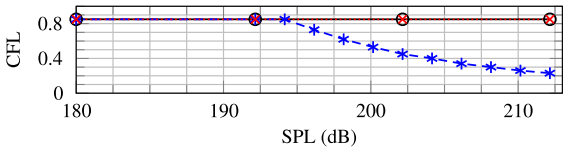

Fig. 5. Maximum CFL number against SPL for the impedance tube of Fig. 4. (—o—) Hard wall $\mathcal{B} = I$ and DG4-RKF84-$\mathcal{B}$-flux. (- -*- -) Nonlinear model (23) with $(a_0, C_{\text{nl}}) = (0, 1)$ and DG4-RKF84-$\mathcal{Z}$-flux. (····×····) Same nonlinear model with DG4-RKF84-$\mathcal{B}$-flux.

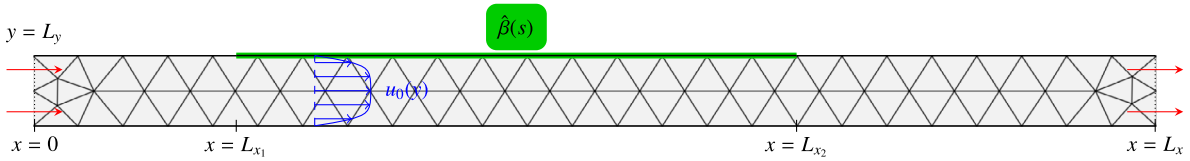

Fig. 6. Flow duct considered in Sec. 6 (aspect ratio of the GIT). Mesh of 106 triangles used in Fig. 14. Pressure measurements are taken on the lower wall $y = 0$. See Table 1 for geometrical dimensions corresponding to the GIT and GFIT.

Table 1
Geometrical dimensions of the GIT and GFIT. The acoustical cut-off frequency is computed through $f_{\text{cut-off}} = c_0(2L_y)^{-1}$, with $c_0 = \sqrt{\gamma r T} \simeq 344.32\,\text{m.s}^{-1}$ ($T = 295\,\text{K}$, $\gamma = 1.4$, and $r = 287.058\,\text{J.kg}^{-1}.\text{K}^{-1}$).

	L_{x_1} (mm)	L_{x_2} (mm)	L_x (mm)	L_y (mm)	$f_{\text{cut-off}}$ (kHz)
GIT [18]	203	609	812.8	51	3.38
GFIT [72]	203.2	812.8	1016	63.5	2.71

CFL number and different meshes. Finally, the bottom right shows the harmonic distortion, a genuinely nonlinear feature, yielded by the algebraic nonlinear model (23) with $C_{\text{nl}} = 1$. As expected, both the $\mathcal{Z}$ and $\mathcal{B}$ fluxes lead to the same solution.

In Fig. 4, the CFL number has been kept at 0.85, its maximum value with a hard wall, for all cases. However, the analysis of Sec. 4 has shown that the $\mathcal{B}$-flux is to be favored over the $\mathcal{Z}$-flux. Fig. 5 illustrates this point with the nonlinear model used in Fig. 4. With the $\mathcal{Z}$-flux, the maximum CFL number that leads to a stable computation decreases as the incident SPL increases, since the resistance increases. By contrast, the $\mathcal{B}$-flux enables to keep the same CFL number, which can be understood from the passivity condition (9) that implies that $\mathcal{B}$ is a contraction. The value $C_{\text{nl}} = 1$ has been chosen arbitrarily, to highlight the nonlinear effect; as the nonlinear coefficient C_{nl} (resp. contraction coefficient C_c) goes to infinity (resp. zero), the SPL value above which the CFL drops with the $\mathcal{Z}$-flux goes to zero. Although this example is elementary, it illustrates the advantage of the nonlinear scattering formulation. A more advanced but linear application is presented in the next section.

6. Numerical application in linear duct aeroacoustics

In this section, numerical simulations of two flow ducts are compared with experimental data, a summary of which is given in Sec. 6.1. Sec. 6.2 describes the employed numerical methodology. Comparison with experimental data is done in the last two sections, Secs. 6.3 and 6.4.

6.1. Experimental methodology and data

The study focuses on two ducts designed by the National Aeronautics and Space Administration (NASA), namely the Grazing Incidence Tube (GIT) and Grazing Flow Impedance Tube (GFIT). A short summary of the experiments reported in [18] and [72] is provided below.

Experimental setup. The GIT and GFIT share a similar geometry, described in Fig. 6 and Table 1. The acoustical source is placed upstream of the entry plane $x = 0$, where a reference microphone is positioned on the lower wall. The source is monochromatic, with a frequency chosen below the lowest cut-off frequency so that only plane waves propagate in the duct. A near-anechoic termination is placed at the exit plane $x = L$. The sound absorbing material sample is mounted on the top wall between L_{x1} and L_{x_2}, while microphones are located on the lower wall. A Pitot probe system enables to measure the base flow u_0 at given cross-sections. See [18, Fig. 2] and [72, Fig. 5] for visualizations of the ducts.

Impedance identification methodology. At each source frequency f_s, pressure measurements are taken on the lower wall $y = 0$ and used to identify the impedance value $\hat{z}_{\text{id}}(\text{j}2\pi f_s)$. The inverse problem relies on the 2D convected Helmholtz equation $(\partial_t + u_0\partial_x)^2 p - c_0^2 \Delta p = 0$ derived from the LEEs (1) by taking a uniform base flow $\boldsymbol{u_0} = c_0 M_{\text{avg}} \boldsymbol{e_x}$, where M_{avg} is the measured average Mach number. Since the base flow is assumed uniform, the IBC used for the identification is *not* (3), as considered in this paper, but the standard Ingard–Myers boundary condition with uniform impedance and straight boundary: [18, Eq. 2]

$$-\hat{z}_{\mathrm{id}}(s)\partial_n\hat{p} = \frac{s}{c_0}\hat{p} + 2M_{\mathrm{avg}}\partial_x\hat{p} + \frac{c_0 M_{\mathrm{avg}}^2}{s}\partial_x^2\hat{p}.$$

Although in principle more accurate results could be obtained by using corrected versions of the Ingard–Myers boundary condition (see Remark 11), the identified impedance $\hat{z}_{\mathrm{id}}$ has proven satisfactory. Note that in addition to $\hat{z}_{\mathrm{id}}$ another impedance is identified, namely the exit impedance enforced at the outlet $x = L$: this impedance is close to 1 since the exit is nearly anechoic in the experiments.

Experimental data. The material considered in the GFIT experiment is a single degree of freedom micro-perforated liner (MP) made from a honeycomb core (thickness $l_c = 38.1\,\mathrm{mm}$, cell diameter $d_c = 9.5\,\mathrm{mm}$) sandwiched between a perforated facesheet (thickness $l_p = 0.8\,\mathrm{mm}$, hole diameter $d_p = 0.3\,\mathrm{mm}$, and porosity $\sigma_p = 5\,\%$) and a rigid backplate. Impedance identifications have been done at an incident SPL of 120 dB (chosen to minimize nonlinear effects), average Mach numbers in {0,0.180,0.271}, and frequencies ranging from 0.4 kHz to 2.6 kHz by steps of 0.2 kHz. The GIT experiment focused on a ceramic tubular liner (CT57) made from a ceramic tubular core ($l_c = 85.6\,\mathrm{mm}$, $d_c = 0.6\,\mathrm{mm}$, $\sigma_c = 57\,\%$) and a rigid backplate. The experimental data, partially reported in [18, Tabs. 1–9], covers an incident SPL of 130 dB, average Mach numbers in {0,0.079,0.172,0.255,0.335,0.400}, and frequencies ranging from 0.5 kHz to 3 kHz by steps of 0.1 kHz. The 0.5 kHz data is excluded since it is less reliable [18].

6.2. Numerical methodology

Discretization. The discretization of the LEEs (1) is identical to that of Sec. 5. In all of the computations, the CFL number is kept at 0.85, its maximum value with a hard wall (i.e. the TDIBC does not reduce the time step). At the entry plane $x = 0$, a plane wave source is imposed using the flux $(A(\boldsymbol{n}_F)\boldsymbol{v})_s^*$, while a non-reflecting boundary condition, exact only for plane waves, is imposed at $x = L_x$ using $(A(\boldsymbol{n}_F)\boldsymbol{v})_{\mathrm{out}}^*$ (see Sec. 4.1). Note that no exit impedance is considered, by contrast with the impedance identification methodology used in [18,72]. The TDIBC is given by (34) and is weakly enforced with the $\mathcal{B}$-flux ((39), (63)) derived in Sec. 4.4.

Base flow. The chosen base flow $\boldsymbol{u_0} = c_0 M_0(y)\boldsymbol{e}_x$ is the hyperbolic velocity profile [17, Eq. 2.4a]

$$\begin{aligned} M_0(r) &= M_c \tanh(\delta^{-1}(1-|r|)) + M_c\big[1-\tanh(\delta^{-1})\big]\big[\delta^{-1}(1+\tanh(\delta^{-1})) + 1 + |r|\big](1-|r|) \\ M_c &= M_{\mathrm{avg}}\big[\delta\ln(\cosh(\delta^{-1})) + [1-\tanh(\delta^{-1})][(6\delta)^{-1}(1+\tanh(\delta^{-1})) + 2/3]\big]^{-1}, \end{aligned} \tag{70}$$

where $r \in [-1, 1]$. This velocity profile has two parameters: the average Mach number M_{avg} and the nondimensional boundary layer thickness $\delta \in (0, 1]$. For $\delta = 1$, the velocity profile is almost identical to the Poiseuille profile $M_0(r) = \frac{3}{2}M_{\mathrm{avg}}(1-r^2)$. More accurate alternatives to this velocity profile include using a turbulent eddy viscosity model where M_0' is known analytically [73, Eq. 3–4], or, when possible, an interpolation of the experimental flow. Using these other velocity profiles does not significantly alter the presented results, but imply the use of a more refined mesh, hence why (70) is chosen herein.

In both experiments, the identified impedance values exhibit a dependency on the grazing base flow. In Secs. 6.3 and 6.4, to account for this dependency, we follow a simple approach inspired by the experimental study [10], whose result has been recalled in Sec. 3.1. The grazing flow is considered as an additional parameter, so that the physical quantities found in the acoustical model (17), such as l_p or l_c for instance, are tweaked when a base flow is present. This empirical approach has been found to be sufficient to match the experimental results.

Post-processing. A polychromatic source $p_s(t) = \sum_{f_s \in I}\sin(2\pi f_s t)$ is used, and each frequency is then separated at the post-processing stage using a sixth-order recursive band-pass filter designed and applied using the MATLAB® Signal Processing Toolbox™ (functions `designfilt` and `filter`). The filtered pressure signals are then used to compute root-mean-square (RMS) values p_{RMS} at each frequency and microphone locations along the bottom wall. The decibel (dB) values are computed with $p_{\mathrm{dB}} = 20\log_{10}(p_{\mathrm{RMS}}) + C$, where the constant C is chosen so that $p_{\mathrm{dB}}(x = 0)$ matches the experimental value at the reference microphone. (Since the numerical scheme is linear, decibel values are indeed defined up to an additive constant.) The simulation is performed over 80 periods of the lowest frequency and convergence of the RMS value is checked.

6.3. Grazing Flow Impedance Tube (GFIT)

Following the three-step methodology described in Sec. 3.3.1 discrete models $\tilde{\beta}$ are built to match the values identified in the GFIT at $M_{\mathrm{avg}} = 0$ and $M_{\mathrm{avg}} = 0.271$, see Table 2.

$M_{avg} = 0$ case. The physical model (17) with coefficients given by (19), (21) provides a fair initial point for the nonlinear least-squares optimization of step 1, the output of which is plotted in Fig. 7. The optimized model accounts for the resistance increase at 0.4 kHz and exhibits a high frequency behavior close to that of the non-optimized model (not plotted), with anti-resonances located around the approximate values $f_n = {}^{nc_0}/_{2l_c}$. The output of step 2, i.e. the discrete oscillatory-diffusive representation of the physical model obtained using a linear least-squares optimization, is therefore satisfactory. In step 3, it is used as an initial guess to build the final discrete model $\tilde{\beta}_A$ (the time delay $\tilde{\tau}$ is not optimized) shown in Fig. 7. A large number of poles, namely three pairs of oscillatory poles s_n and two high frequency diffusive poles ξ_k, have been

Table 2
TDIBCs (31) obtained in Sec. 6. Only poles in the upper half-plane $\{s \,|\, \Im(s) \geq 0\}$ are given (the full set is obtained by complex conjugation).

$(\tilde{s}_n, -\tilde{\xi}_k)_{n,k}$ (rad.s^{-1})	$\tilde{r}_{1,n}, \tilde{\mu}_{1,k}$	$\tilde{r}_{2,n}, \tilde{\mu}_{2,k}$
$\tilde{\beta}_A$	$\tilde{\beta}_\infty = 1$	$\tilde{\tau} = 2.074709\text{e}{-04}$ s
−9.425004e+04	4.399745e+05	−3.301477e+05
−1.005288e+05	−4.844596e+05	3.648366e+05
−6.590198e+03+8.091231e+03i	−3.316669e+03+1.245272e+03i	3.034471e+03−1.360501e+03i
−3.313575e+03+3.441899e+04i	−2.597563e+03+2.012662e+03i	2.246072e+03−1.972699e+03i
−2.074806e+03+6.332235e+04i	−2.161554e+03+1.610479e+03i	1.750988e+03−1.684290e+03i
$\tilde{\beta}_B$	$\tilde{\beta}_\infty = 1$	$\tilde{\tau} = 1.698885\text{e}{-04}$ s
−4.397915e+04	−3.896423e+04	9.305033e+03
−9.339632e+03+8.499373e+03i	−2.058287e+03−2.722431e+03i	−1.203382e+03−2.923788e+03i
−1.645826e+04+3.974646e+04i	−7.781838e+03−3.535171e+03i	−8.796038e+02+3.204374e+02i
−2.106499e+04+7.256816e+04i	−1.507929e+04−1.588215e+04i	−1.536644e+03+7.662377e+02i
$\tilde{\beta}_C$	$\tilde{\beta}_\infty = 1$	$\tilde{\tau} = 3.100751\text{e}{-06}$ s
−5.748740e+03+4.228554e+03i	−1.010084e+05+2.101821e+05i	1.005155e+05−2.103401e+05i
$\tilde{\beta}_D$	$\tilde{\beta}_\infty = 0.5$	$\tilde{\tau} = 4.799390\text{e}{-04}$ s
−3.816516e+03+4.734560e+03i	−7.194232e+02−5.447907e+02i	1.625807e+03+9.996580e+01i
−2.765741e+04+2.000290e+04i	−7.179701e+03−7.336684e+03i	1.614688e+04+1.930627e+04i
$\tilde{\beta}_E$	$\tilde{\beta}_\infty = 0.7$	$\tilde{\tau} = 5.099183\text{e}{-04}$ s
−9.424902e+04+3.641784e+04i	−7.932877e+04−1.495889e+05i	5.737738e+04+8.853810e+04i
$\tilde{\beta}_F$	$\tilde{\beta}_\infty = 5.888134\text{e}{-01}$	$\tilde{\tau} = 5.217335\text{e}{-04}$ s
−6.414157e	9.506538e+04	−1.096633e+04
−2.051627e+04	−1.320127e+05	1.486746e+04
−4.849574e+03+6.072352e+03i	−1.457643e+03+3.397179e+04i	5.526842e+02+7.586494e+02i
−6.618336e+03+1.885015e+04i	3.599154e+03+3.495625e+03i	−4.862369e+02+5.032293e+02i

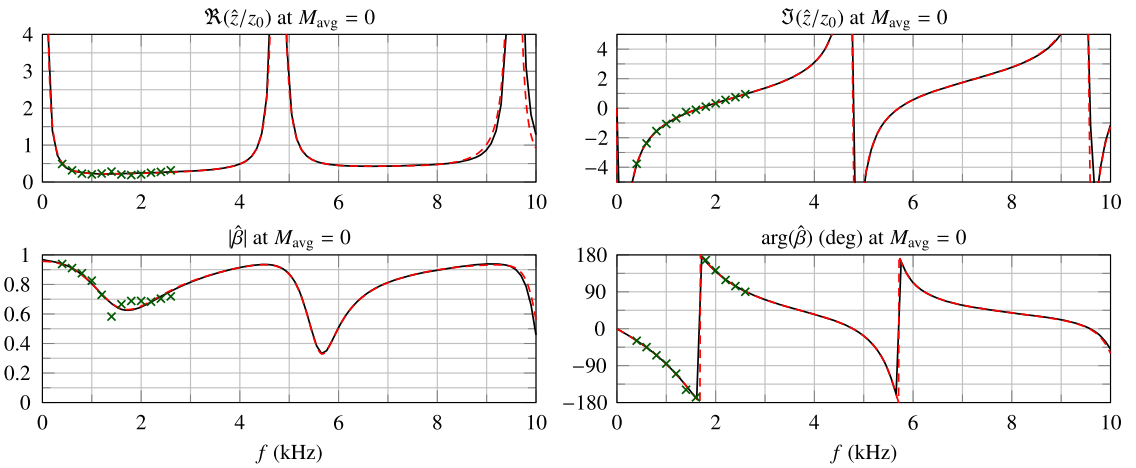

Fig. 7. Impedance $\hat{z}$ and reflection coefficient $\hat{\beta}$. (×) $\hat{z}_{\text{id}}/z_0$ identified with the methodology described in Sec. 6.1. MP liner in the GFIT at $M_{\text{avg}} = 0$ and 120 dB [72, Fig. 12]. (———) $\hat{z}_{\text{MP}}/z_0$ (17) with optimized coefficients $\sigma_p^{-1} a_0 = 2.221 \times 10^{-14}$, $\sigma_p^{-1} a_{1/2} = 2.518 \times 10^{-3}$ s$^{1/2}$, $\sigma_p^{-1} a_1 = 3.408 \times 10^{-5}$ s, $\sigma_c^{-1} = 1.107$, $b_0 = 1.750 \times 10^{-2}$, $b_{1/2} = 2.321 \times 10^{-4}$ s$^{1/2}$, and $b_1 = 1.037 \times 10^{-4}$ s; time delay $\tau = 2b_1 = 2.075 \times 10^{-4}$ s. (– – – –) TDIBC $\hat{\tilde{\beta}}_A$: $N_\varphi = 8$ poles ($N_\xi = 2$, $N_s = 6$), $(2\pi)^{-1} \max(\xi_k, |s_n|) = 1.008 \times 10^1$ kHz, and $\tilde{\tau} = 2.075 \times 10^{-4}$ s. (This curve assumes that the time delay term $e^{-2\pi \mathrm{j} f \tilde{\tau}}$ is perfectly approximated.)

chosen to build a broadband approximation. The corresponding SPLs along the lower wall are given in Fig. 8 for two choices of N_ψ to illustrate the impact of the delay discretization: a value of $N_\psi = 4$ is sufficient here. The agreement with experimental pressure measurements is satisfactory, the largest error occurring at 1.4 kHz. However, based on the plot of $|\hat{\beta}_{\text{id}}|$ given at the bottom left of Fig. 7, this point appears to be an outlier. To confirm this, the SPLs obtained with the identified impedance values are also given. They are computed using *six* proportional-integral-derivative (PID) impedance models $\hat{z}_{\text{PID},i}(s) = d_{0,i} s^{-1} + d_{1,i} + d_{2,i} s$, implemented as (34) with $\tilde{\tau} = 0$, each chosen so that $\hat{z}_{\text{PID},i}(\mathrm{j}2\pi f_i) = \hat{z}_{\text{id}}(\mathrm{j}2\pi f_i)$. The plot shows that at 1.4 kHz the tuned PID model also exhibits a significant error.

$M_{avg} = 0.271$ *case.* The identified values exhibit a strong resistance increase compared to the no flow case. Here, step 1 requires some care: the optimization of the physical model coefficients (17) is strongly dependent on the initial point, in stark contrast to the other three cases considered in this paper. A contributing factor to this sensitivity is the lack of anti-resonance in the experimental data, which stops at 2.6 kHz. Fig. 9 plots an optimized model that exhibits two anti-resonances, obtained by doubling l_c in the initial guess ((17), (19), (21)). Additional experimental data would be needed

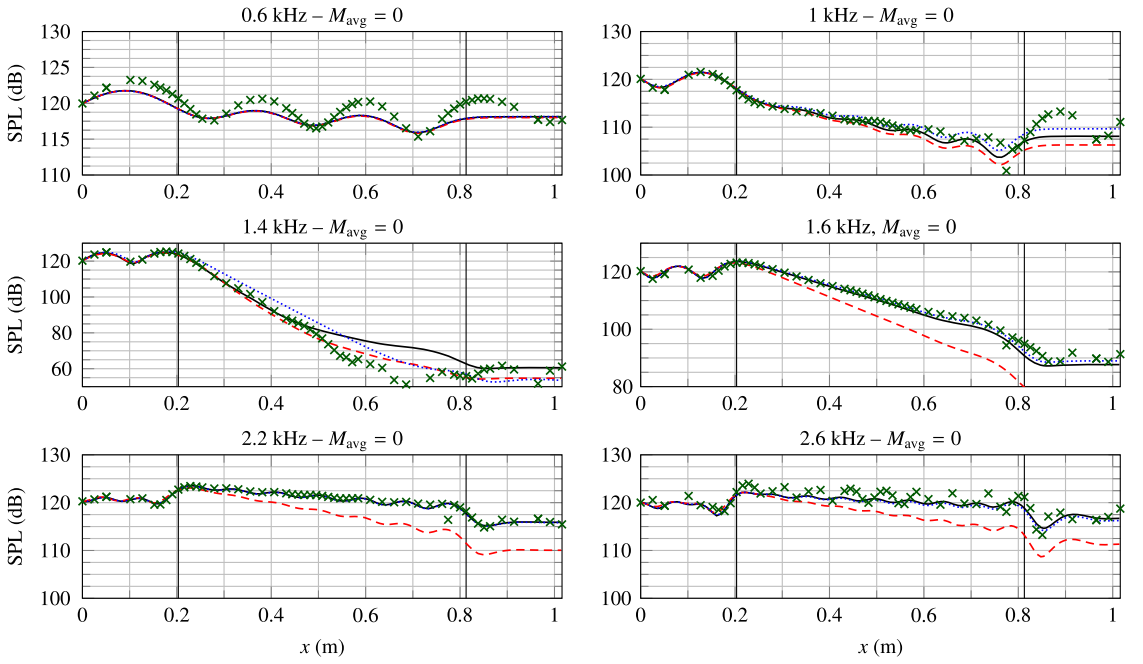

Fig. 8. RMS values of acoustic pressure p_{RMS} on the lower wall $y = 0$ (see Fig. 6). DG4-RKF84-$\mathcal{B}$-flux on 110 triangles (1100 nodes), CFL = 0.85. (———) TDIBC $\tilde{\beta}_A$ with $N_\psi = 4$ so that $PPW_{\tilde{\tau}}(2.6\,kHz) = 7.42$. (– – – –) TDIBC $\tilde{\beta}_A$ with $N_\psi = 2$ so that $PPW_{\tilde{\tau}}(2.6\,kHz) = 3.71$. (·····) Six proportional-integral-derivative TDIBCs $\tilde{\beta}_{PID}$, each matching the identified impedance at one frequency only. (×) MP liner in the GFIT at $M_{avg} = 0$ and 120 dB [72].

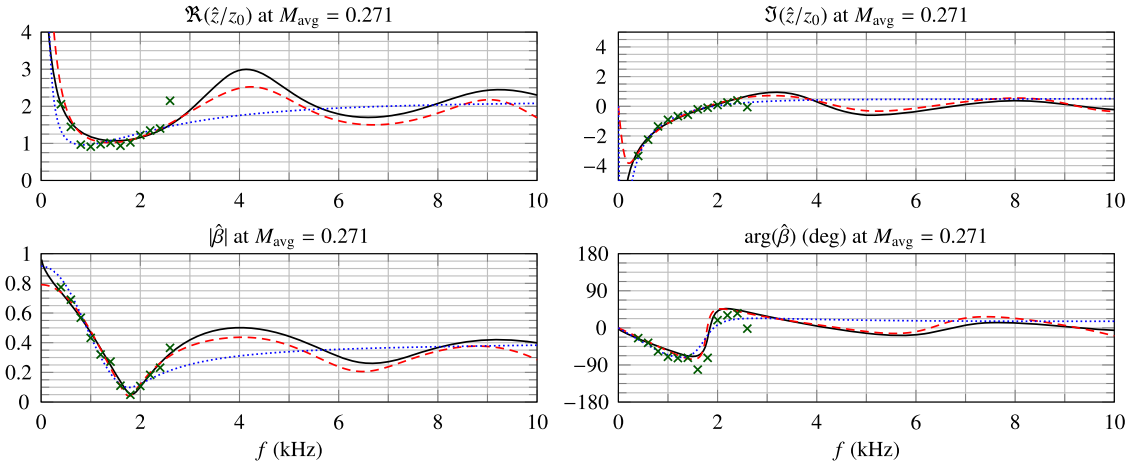

Fig. 9. Impedance $\hat{z}$ and reflection coefficient $\hat{\beta}$. (×) $\hat{z}_{id}/z_0$. MP liner in the GFIT at $M_{avg} = 0.271$ and 120 dB [72]. (———) $\hat{z}_{MP}/z_0$ (17) with optimized coefficients $\sigma_p^{-1}a_0 = 2.220 \times 10^{-14}$, $\sigma_p^{-1}a_{1/2} = 2.220 \times 10^{-14}\,s^{1/2}$, $\sigma_p^{-1}a_1 = 2.220 \times 10^{-14}\,s$, $\sigma_c^{-1} = 2.116$, $b_0 = 2.220 \times 10^{-14}$, $b_{1/2} = 7.67 \times 10^{-3}\,s^{1/2}$, and $b_1 = 8.494 \times 10^{-5}\,s$; $\tau = 1.699 \times 10^{-4}\,s$. (– – – –) TDIBC $\hat{\tilde{\beta}}_B$: $N_\varphi = 7$ poles ($N_\xi = 1$, $N_s = 6$), $(2\pi)^{-1}\max(\xi_k, |s_n|) = 1.203 \times 10^1$ kHz, and $\tilde{\tau} = 1.699 \times 10^{-4}\,s$. (·····) TDIBC $\hat{\tilde{\beta}}_C$: $N_\varphi = 2$ poles ($N_\xi = 0$, $N_s = 2$), $(2\pi)^{-1}\max(\xi_k, |s_n|) = 1.136$ kHz, and $\tilde{\tau} = 3.101 \times 10^{-6}\,s$. (The last two curves assume that the time delay term $e^{-2\pi j f \tilde{\tau}}$ is perfectly approximated.)

to validate this model above 2.6 kHz. This sensitivity is also exhibited by step 3. If the time delay $\tilde{\tau}$ is optimized, it is greatly reduced (i.e. $\tilde{\tau} \ll \tau$) thus modifying the high frequency behavior. To illustrate this point, Fig. 9 shows two discrete models. The model $\tilde{\beta}_C$ is obtained by keeping l_c to its physical value in the initial guess of step 1, choosing only one pair of oscillatory poles s_n in step 2, and optimizing on $\tilde{\tau}$ in step 3. It provides an adequate approximation of the experimental data but a poor high frequency behavior, linked to its negligible delay $\tilde{\tau} \simeq \tau/54$. The model $\tilde{\beta}_B$ is obtained by using the physical model shown in Fig. 9 during step 1, choosing three pairs of oscillatory poles s_n and one high frequency diffusive pole ξ_k in step 2, and keeping $\tilde{\tau}$ constant in step 3.

Fig. 10 plots the computed SPL distributions. The dotted curves enable to check the relevance of the identified impedance values. The strongest disparities are obtained below 1 kHz where the measurements suggest the presence of a longitudinal resonance not modeled with our non-reflecting outlet, also noticeable in the no flow case, see Fig. 8. At these low frequen-

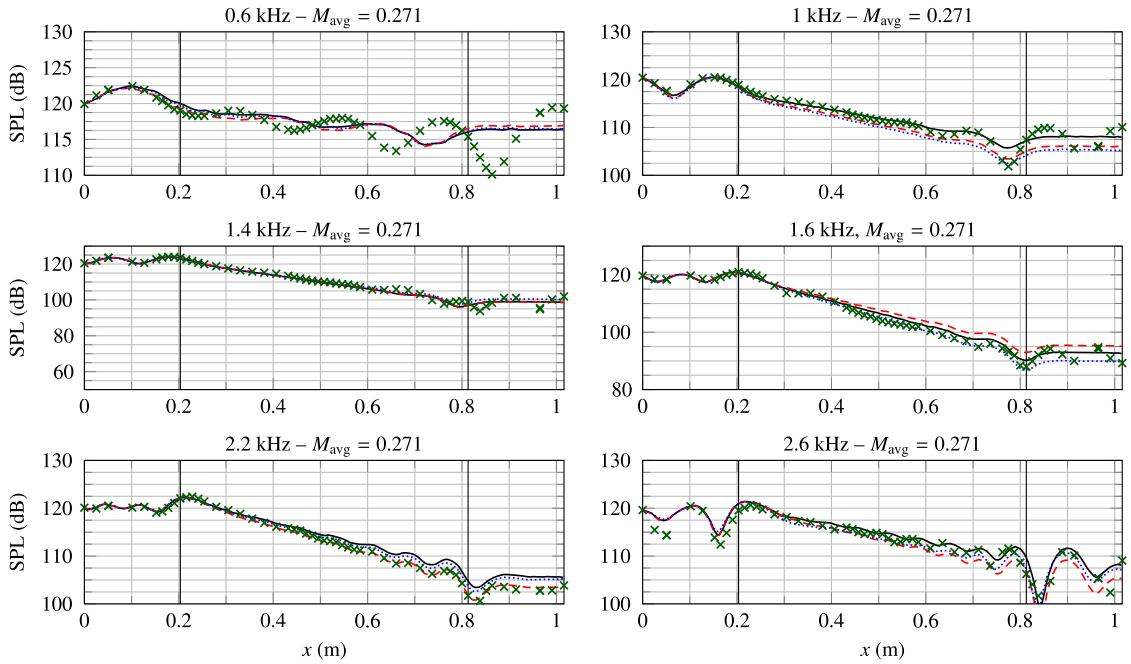

Fig. 10. RMS values of acoustic pressure p_{RMS} on the lower wall $y = 0$. DG4-RKF84-$\mathcal{B}$-flux on 326 triangles (3260 nodes), CFL = 0.85. Base flow (70) with $M_{\text{avg}} = 0.271$ and $\delta = 0.2$. (———) TDIBC $\tilde{\beta}_B$ with $N_\psi = 3$ so that $\text{PPW}_{\tilde{\tau}}(2.6\,\text{kHz}) = 6.79$. (– – – –) TDIBC $\tilde{\beta}_C$ with $N_\psi = 2$ so that $\text{PPW}_{\tilde{\tau}}(2.6\,\text{kHz}) = 248$. (·····) Six TDIBCs $\tilde{\beta}_{\text{PID}}$ with $\delta = 0.25$. (×) MP liner in the GFIT at $M_{\text{avg}} = 0.271$ and 120 dB [72].

cies, the fidelity of the SPLs obtained with $\tilde{\beta}_B$ and $\tilde{\beta}_C$ is therefore bound to be limited. Although the TDIBC B is significantly more expensive than C, both lead to similar SPLs with no significant discrepancies. The time delay of $\tilde{\beta}_C$ is negligible on the considered frequency range so that the minimal value $N_\psi = 2$ is already too large, as shown by the value of $\text{PPW}_{\tilde{\tau}}$.

6.4. Grazing Incidence Tube (GIT)

$M_{avg} = 0$ *case.* Step 1 delivers an adequate set of coefficients for the physical model (17), see Fig. 11. The model $\tilde{\beta}_D$ is obtained by choosing the first two pairs of oscillatory poles s_n in step 2 and optimizing the time delay $\tilde{\tau}$ in step 3 (although it can be kept constant as well). The slight decay of the physical model at high frequency is linked to a small but non-null diffusive part that can be captured by adding diffusive poles ξ_k to $\tilde{\beta}_D$ [5, § VI.B]. However, this is not needed here in view of the computed SPLs shown in Fig. 12. Compared to the MP liner considered in Sec. 6.3, both a higher delay and a higher maximum frequency lead to a sensible increase in N_ψ.

$M_{avg} = 0.4$ *case.* The identified impedance values display a very low resistance within $[0.7, 1.1]$ kHz and the shape of $|\hat{\beta}_{\text{id}}|$ suggests the presence of noise in the data, see the bottom left of Fig. 13, as one may expect due to the high value of M_{avg}. The output of step 1 is sensitive to the chosen experimental points since the physical model (17) cannot fit both the low and high resistance regions, namely $[0.7, 1.1]$ kHz and $[2.3, 3]$ kHz. However, step 1 is not sensitive to the initial guess provided that the chosen data points cover the anti-resonance. Additionally, the 1 kHz value is best removed since it leads to an instability with the LEEs as shown in the dotted curve at the top right of Fig. 14, and investigated in [74, § VI.B.2]. (Including the 1 kHz point in the optimization process has been found to systematically lead to an unstable pole, i.e. $\Re(s_n) > 0$ or $\xi_k < 0$.) Due to the shortcomings of the physical model, step 3 has a tendency to overfit the experimental data, so that we do not optimize on the delay $\tilde{\tau}$ during step 3.

The discrete model $\tilde{\beta}_E$, plotted in Fig. 13, is obtained by using only 2 oscillatory poles s_n and excluding the data points in/at $[0.7, 0.8]$, $[1, 1.4]$, 1.8, and $[2.1, 2.3]$ kHz. Fig. 14 shows that $\tilde{\beta}_E$ compares favorably to the experimental pressure measurements. The increased resistance at 1 kHz compared with the identified value reduces the instability, although not enough to fit the experiment. The discrepancy at 3 kHz, since it is also obtained with the identified value, could be explained by the presence of higher-order modes in the experiment, which can be assessed using the cut-off frequency of a hard walled duct with uniform flow, given by $c_0(2L_y)^{-1}\sqrt{1 - M_{\text{avg}}^2} = 3.01$ kHz.

The discrete model $\tilde{\beta}_F$ is obtained by excluding the data points in/at $[0.7, 1.2]$, 1.8, and $[2.1, 2.3]$ kHz. Compared to $\tilde{\beta}_E$, the addition of one pair of oscillatory poles s_n and two high frequency diffusive poles ξ_k leads to an overfit that significantly alter the high frequency behavior, see Fig. 13. However, the corresponding SPLs are satisfactory, especially at 3 kHz. Since the delay of both models is close, they share a common value of N_ψ.

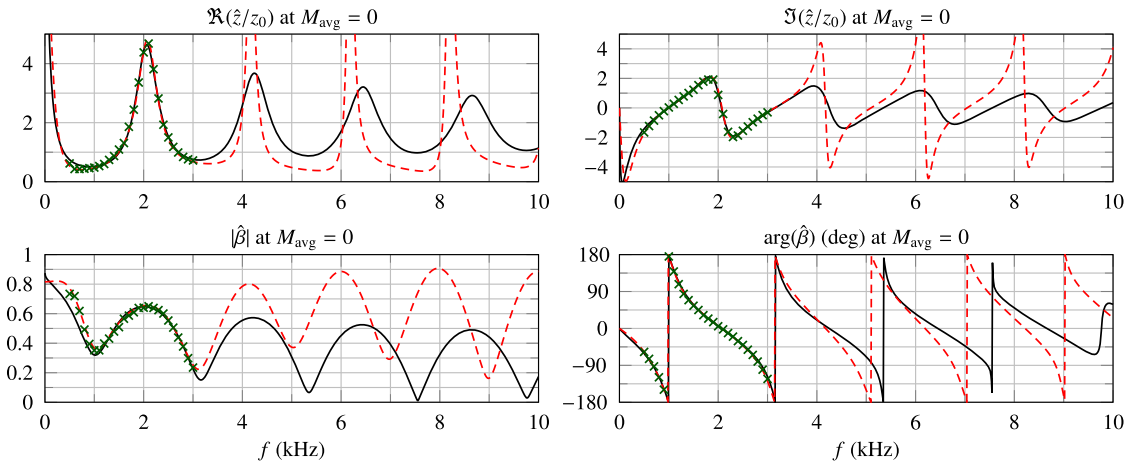

Fig. 11. Impedance $\hat{z}$ and reflection coefficient $\hat{\beta}$. (×) $\hat{z}_{\text{id}}/z_0$. CT57 liner in the GIT at $M_{\text{avg}} = 0$ and 130 dB [18]. (———) $\hat{z}_{\text{CT}}/z_0$ (17) with optimized coefficients $\sigma_c^{-1} = 1.728$, $b_0 = 1.161 \times 10^{-1}$, $b_{1/2} = 3.413 \times 10^{-3}\,\text{s}^{1/2}$, and $b_1 = 2.207 \times 10^{-4}\,\text{s}$; $\tau = 4.412 \times 10^{-4}\,\text{s}$. (– – – –) TDIBC $\hat{\tilde{\beta}}_D$: $N_\varphi = 4$ poles ($N_\xi = 0$, $N_s = 4$), $(2\pi)^{-1} \max(\xi_k, |s_n|) = 5.432\,\text{kHz}$, and $\tilde{\tau} = 4.799 \times 10^{-4}\,\text{s}$. (This curve assumes that the time delay term $e^{-2\pi \mathrm{j} f \tilde{\tau}}$ is perfectly approximated.)

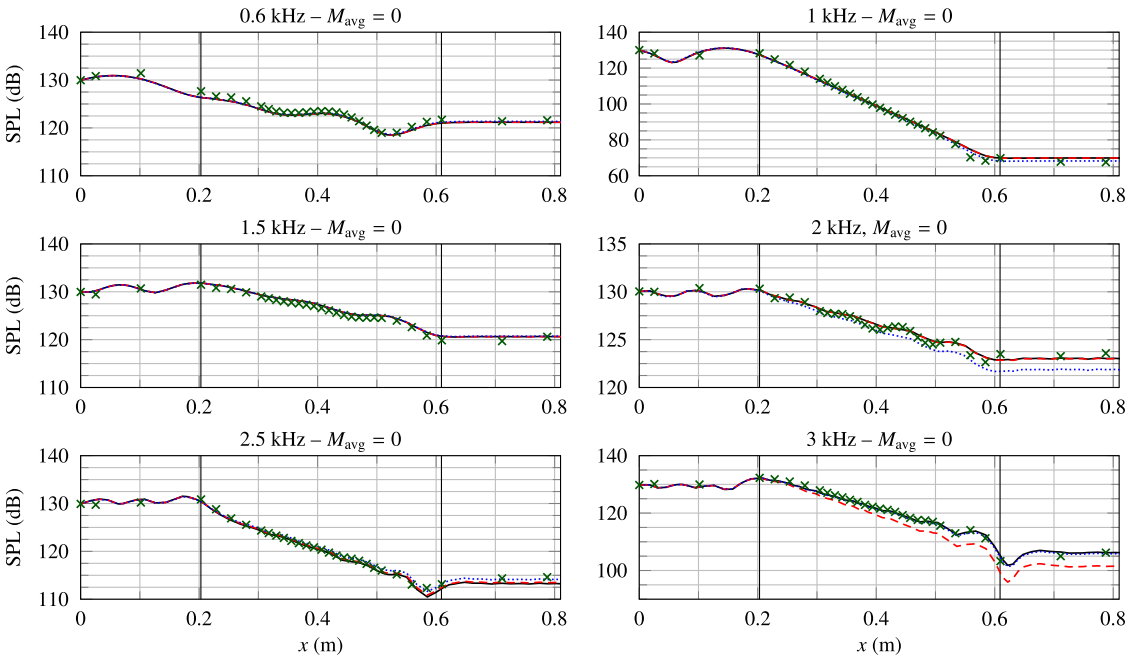

Fig. 12. RMS values of acoustic pressure p_{RMS} on the lower wall $y = 0$. DG4-RKF84-$\mathcal{B}$-flux on 52 triangles (520 nodes), CFL = 0.85. (———) TDIBC $\tilde{\beta}_D$ with $N_\psi = 8$ so that $\text{PPW}_{\tilde{\tau}}(3\,\text{kHz}) = 5.56$. (– – – –) TDIBC $\tilde{\beta}_D$ with $N_\psi = 6$ so that $\text{PPW}_{\tilde{\tau}}(3\,\text{kHz}) = 4.17$. (·····) Six TDIBCs $\tilde{\beta}_{\text{PID}}$ with CFL = 0.84. (×) CT57 liner in the GIT at $M_{\text{avg}} = 0$ and 130 dB [18, Tab. 3].

7. Conclusion and perspectives

The semi-discrete energy analysis presented in Sec. 4 has shown the computational advantage of using the scattering operator over the impedance and admittance operators when solving the linearized Euler equations. In the analysis, the IBC has only been assumed to be admissible in the sense of Definitions 1 and 6. The derived numerical flux, the so-called $\mathcal{B}$-flux ((39), (63)), has been interpreted in Remark 26 as that obtained from solving the monodimensional Riemann problem at the impedance boundary, which is standard in computational fluid dynamics. In practice, if the scattering operator cannot be computed efficiently or is not available, then the impedance (resp. admittance) is to be preferred a priori if the material is close to a pressure-release wall (resp. hard wall). A consistent but not passive numerical flux has been exhibited in Example 24, which justifies the need for such a careful analysis of the numerical flux and highlights the fact that the sole definition of the discrete model is not enough to fully define a TDIBC.

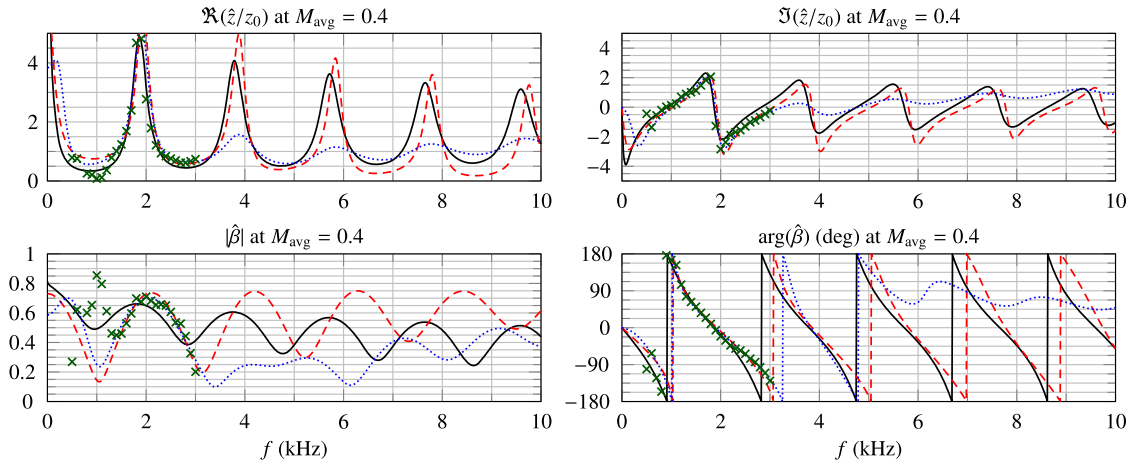

Fig. 13. Impedance $\hat{z}$ and reflection coefficient $\hat{\beta}$. (×) $\hat{z}_{\text{id}}/z_0$. CT57 liner in the GIT at $M_{\text{avg}} = 0.4$ and 130 dB [18]. (——) $\hat{z}_{\text{CT}}/z_0$ (17) with optimized coefficients $\sigma_c^{-1} = 1.398$, $b_0 = 1.442 \times 10^{-1}$, $b_{1/2} = 1.956 \times 10^{-3}\ \text{s}^{1/2}$, and $b_1 = 2.550 \times 10^{-4}$ s; $\tau = 5.099 \times 10^{-4}$ s. (– – – –) TDIBC $\hat{\tilde{\beta}}_E$: $N_\varphi = 2$ poles ($N_\xi = 0$, $N_s = 2$), $(2\pi)^{-1} \max(\xi_k, |s_n|) = 1.608 \times 10^1$ kHz, and $\tilde{\tau} = 5.099 \times 10^{-4}$ s. (·····) TDIBC $\hat{\tilde{\beta}}_F$: $N_\varphi = 6$ poles ($N_\xi = 2$, $N_s = 4$), $(2\pi)^{-1} \max(\xi_k, |s_n|) = 3.180$ kHz, and $\tilde{\tau} = 5.217 \times 10^{-4}$ s. (The last two curves assume that the time delay term $e^{-2\pi \mathrm{j} f \tilde{\tau}}$ is perfectly approximated.)

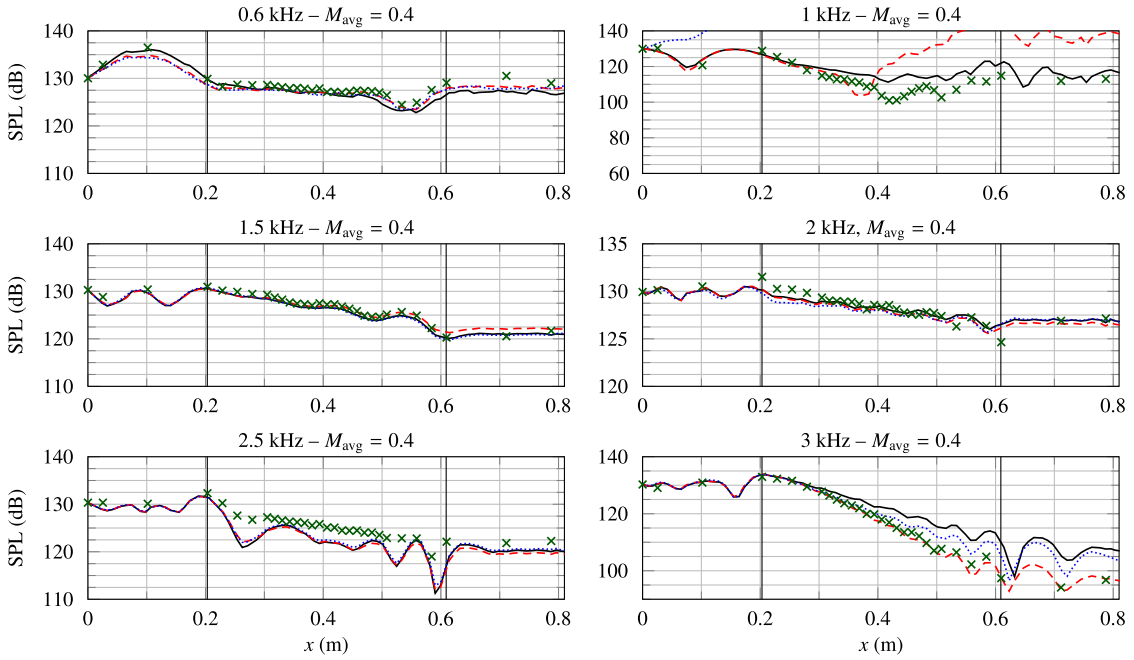

Fig. 14. RMS values of acoustic pressure p_{RMS} on the lower wall $y = 0$. DG4-RKF84-$\mathcal{B}$-flux on 106 triangles (1060 nodes), CFL = 0.85. Base flow (70) with $M_{\text{avg}} = 0.4$ and $\delta = 0.2$. (——) TDIBC $\tilde{\beta}_E$ with $N_\psi = 8$ so that $\text{PPW}_{\tilde{\tau}}(3\,\text{kHz}) = 5.23$. (– – – –) TDIBC $\tilde{\beta}_F$ with $N_\psi = 8$ so that $\text{PPW}_{\tilde{\tau}}(3\,\text{kHz}) = 5.11$. (·····) Six TDIBCs $\tilde{\beta}_{\text{PID}}$ with $\delta = 0.26$. (×) CT57 liner in the GIT at $M_{\text{avg}} = 0.4$ and 130 dB [18, Tab. 8].

An example of nonlinear scattering operator, derived from a physical perforation impedance model in Sec. 3, has been shown in Sec. 5 to deliver a stability CFL number independent of the incident sound pressure level, by contrast with a formulation based on the impedance operator. The analytical solution (69), sufficient for validating of a nonlinear TDIBC, has been recalled.

Within the linear realm, the oscillatory-diffusive representation of a physical reflection coefficient model, applicable to acoustical liners, has been given in Sec. 3 and has led to the definition of the time-delayed broadband discrete model (31) that bears some similarities with discrete models postulated in the literature. In order to perform time integration with a Runge–Kutta method, a purely time-local formulation (34), based on a realization of the time delay through a transport equation, has been applied to two flow ducts in Sec. 6.

More marginally, Sec. 2 and Appendix A have recalled the interest of using the Laplace transform over the Fourier transform to deal with the admissibility conditions of impedance models.

The limitations of this work suggest ideas for future studies; five of them are listed below, the first three being numerical. First, a similar energy analysis could be applied to Ingard–Myers type IBCs in order to gain theoretical insights into their discretizations. Second, the presented nonlinear numerical application could be extended to a differential impedance operator $\mathcal{Z}$. In such a case, the computational challenge lies in the efficient computation of $\mathcal{B}$, which must avoid computing $(z_0^{-1}\mathcal{Z}+\mathcal{I})^{-1}$ since it may involve a nonlinear stiff ODE. Third, the present study can be seen as a first step towards the analysis of the enforcement of a TDIBC with the Euler or Navier–Stokes equations. Challenges include the filtering of the perturbation as well as the treatment of the diffusion term at the impedance boundary. The last two suggestions are physical. Fourth, the present work shows that TDIBCs benefit from physical knowledge about the impedance. This calls for additional investigations into the suitability of available models in the presence of grazing flow and broadband sources, as well as the inclusion of uncertainties during both identification and simulation. Last, the physical relevance of using a nonlinear impedance model with the LEEs could be investigated, by comparison with experimental data gathered in an impedance tube at high SPL.

Acknowledgements

This research has been financially supported by the French ministry of defense (Direction Générale de l'Armement) and ONERA (the French Aerospace Lab). The authors are grateful to Dr. Michael Jones (NASA) for providing the CT57 and MP experimental data, Dr. Sébastien Pernet (ONERA) for his insights into the analysis of Discontinuous Galerkin methods, and Dr. Hugues Deniau (ONERA) for invaluable exchanges on computational fluid dynamics.

Appendix A. Difference between Fourier and Laplace transforms for impedance models and admissibility conditions

Many works related to impedance boundary conditions use the Fourier transform, at least formally. The objective of this appendix is to briefly present why the Laplace transform should be preferred to the Fourier transform when dealing with causal functions. The Fourier transform is defined over the set of tempered distributions $\mathcal{S}'(\mathbb{R})$ (i.e. generalized functions with at most polynomial growth at infinity) [4, Chap. V] [51, Chap. 7] [50, § 1.8]. This implies that the use of the Fourier transform is not always possible, as it does not apply to an exponentially growing function like $t \mapsto H(t)e^t$ for instance. The Laplace transform is defined over the set of causal distributions $\mathcal{D}'_+(\mathbb{R})$ with at most finite exponential growth at infinity [4, Chap. VI] [51, Chap. 8] [50, Chap. II]. A practical consequence of these definitions is that the Laplace transform is always a holomorphic *function* of an open right half-plane while the Fourier transform may only be a tempered *distribution*. As a result, using the Fourier transform is usually more cumbersome. Let us illustrate this point on two examples encountered in acoustics.

Fourier transform of physical impedance models

The Laplace transform $\hat{z}$ of a physical impedance model is a holomorphic function of the open right half-plane $\{\Re(s) > 0\}$, see e.g. the examples of Sec. 3.1. Since it is a positive-real function, the Fourier transform $\mathcal{F}(z)$ exists and belongs to $\mathcal{S}'(\mathbb{R})$ [50, § 3.5]. However, the mere substitution of $\mathrm{j}\omega$ ($\omega \in \mathbb{R}$) for s in the expression of $\hat{z}(s)$ does *not* yield the Fourier transform, i.e. $\mathcal{F}(z)(\omega) \neq \hat{z}(\mathrm{j}\omega)$. Mathematically, this is due to the fact that the limit $\lim_{\sigma\to 0}\hat{z}(\sigma+i\omega)$ may only exist in the space of tempered distribution $\mathcal{S}'(\mathbb{R})$.

The impedance model $\hat{z}(s) = 1/s$, which arises in the modeling of ground layers [5, Eq. 24], is a textbook example of this phenomenon. The function $\omega \mapsto 1/\mathrm{j}\omega$ exhibits a non-integrable singularity at $\omega = 0$. As a result it is not a distribution and thus cannot be a Fourier transform. Taking the limit in $\mathcal{S}'(\mathbb{R})$ yields the standard expression

$$\mathcal{F}(z)(\omega) = \mathrm{pv}\left(\frac{1}{\mathrm{j}\omega}\right) + \pi\,\delta,$$

where pv denotes the Cauchy principal value. It is important to note that $\mathcal{F}^{-1}\left[\mathrm{pv}\left(\frac{1}{\mathrm{j}\omega}\right)\right](t) = \frac{1}{2}\mathrm{sign}(t)$ is not causal: the term "$\pi\,\delta$" is needed for causality. Similarly, consider the impedance of a lossless cavity (see Sec. 3.1) $\hat{z}(s) = \coth(b_1 s)$ with $b_1 > 0$. Again, the function $\omega \mapsto \coth(\mathrm{j}b_1\omega) = -\mathrm{j}\cot(b_1\omega)$ has non-integrable singularities at the anti-resonant angular frequencies $\omega_n = n\pi/b_1$ and therefore cannot be a Fourier transform. The Fourier transform is given by

$$\mathcal{F}(z)(\omega) = \mathrm{pv}\left(\coth(\mathrm{j}b_1\omega)\right) + \frac{\pi}{b_1}\sum_{n=-\infty}^{+\infty}\delta\left(\omega - \frac{n\pi}{b_1}\right),$$

where the infinite sum converges in $\mathcal{S}'(\mathbb{R})$. Note that the π/b_1-periodic distribution $\mathcal{F}^{-1}\left[\mathrm{pv}\left(\coth(\mathrm{j}b_1\omega)\right)\right]$ is not causal, as illustrated by its Fourier series expansion

$$\mathrm{pv}\left(\coth(\mathrm{j}b_1\omega)\right) = \sum_{n=-\infty}^{\infty} c_n e^{\mathrm{j}2nb_1\omega},$$

with $c_0 = 0$, $c_n = -1$, and $c_{-n} = -c_n$ for $n \geq 1$.

Admissibility conditions

In Sec. 2.2, admissibility conditions have been formulated using the Laplace transforms $\hat{z}$, $\hat{y}$, and $\hat{\beta}$, see Propositions 3 and 8. These conditions are straightforward to verify in practice using the expressions of physical models. However, formulating the same admissibility conditions using the Fourier transform is more involved. Let us illustrate this point by considering the causality condition for a tempered distribution $z \in \mathcal{S}'(\mathbb{R})$. The distribution z is causal if and only if its Fourier transform $\mathcal{F}(z)$ satisfies a so-called dispersion relation [50, Thm. 3.10], which links its real and imaginary parts. By contrast, the distribution z is causal if and only if its Laplace transform $\hat{z}$ is bounded by a polynomial in $|s|$ in the open right half-plane $\{\Re(s) > 0\}$ [4, Thm. VI.5] [50, Thm. 2.5] [51, § 8.4]. As shown by the example below, a formal use of the Fourier transform can lead to mistakes.

Example 29. Let us consider the kernel given by $z(t) = \delta(t) + \delta(t+\tau)$ with $\tau > 0$. Since $\tau > 0$, z is not causal. A simple examination shows that the Laplace transform $\hat{z}(s) = 1 + e^{+s\tau}$ is not positive-real since $\Re(1 + e^{+s\tau}) < 0$ for some $s \in \mathbb{C}_0^+$ with a sufficiently large real part. This is consistent with the fact, recalled in Sec. 2.2, that a real (continuous) LTI system cannot be both anticausal and passive. Note that a formal use of the Fourier transform can lead to a mistake, since this kernel satisfies both $\hat{z}(\mathrm{j}\omega) = \overline{\hat{z}(-\mathrm{j}\omega)}$ and $\Re(\hat{z}(\mathrm{j}\omega)) \geq 0$ for any $\omega \in \mathbb{R}$ but is not passive.

Appendix B. Discontinuous Galerkin estimates

This appendix gathers the few technical results needed for the stability analysis presented in Sec. 4. The background material for the analysis can be found in [66], [65], and [67]. As stated in Sec. 4, $(\mathcal{T}_h)_h$ is a sequence of meshes indexed by $h := \max_{T\in\mathcal{T}_h} h_T$, where h_T denotes the diameter of the element $T \in \mathcal{T}_h$. For simplicity, each mesh $\mathcal{T}_h$ is assumed to be simplicial [65, Def. 1.53] [66, Def. 1.11], geometrically conformal [65, Def. 1.55] (also "matching" [66, Def. 1.36]), shape-regular [66, Def. 1.38] [65, Def. 1.107], and the mesh sequence $(\mathcal{T}_h)_h$ is assumed to be quasi-uniform [65, Def. 1.140] [66, § 3.1.2]. The key result needed is the standard trace inequality, which is recalled below.

Lemma 30 *(Discrete trace inequality). Let $(\mathcal{T}_h)_h$ be a quasi-uniform sequence of simplicial, geometrically conformal, and shape-regular meshes. For any dimension $n \in \mathbb{N}^*$ and degree $k \in \mathbb{N}^*$, there is a constant $C_{\mathrm{tr}} > 0$ such that $\forall h > 0$, $\forall T \in \mathcal{T}_h$, for any face F_T,*

$$\forall \boldsymbol{v}_h \in \mathbb{P}_n^k(\mathcal{T}_h)^{n+1},\ h^{1/2}\|\boldsymbol{v}_h\|_{L^2(F_T)} \leq C_{\mathrm{tr}}\|\boldsymbol{v}_h\|_{L^2(T)}. \tag{B.1}$$

The constant C_{tr} only depends upon n, k, and the mesh regularity parameter $\rho_1 := \inf_h \inf_{T\in\mathcal{T}_h} \frac{r_T}{h_T}$ with r_T the radius of the largest ball inscribed in T.

Proof. Let $h > 0$ and $T \in \mathcal{T}_h$. Since $\mathcal{T}_h$ is a simplicial, geometrically conformal, and shape-regular mesh, we have [66, Eq. (1.39)] $h_T^{1/2}\|\boldsymbol{v}_h\|_{L^2(F_T)} \leq C_{\mathrm{tr,s}}\|\boldsymbol{v}_h\|_{L^2(T)}$, where $C_{\mathrm{tr,s}}$ only depends upon ρ_1, n, and k. By definition, the quasi-uniformity of $\mathcal{T}_h$ gives a constant $C > 0$ such that $Ch \leq \min_{T\in\mathcal{T}_h} h_T$. □

The estimation of the impedance boundary terms in $\mathcal{A}_h$ ((53), (67)) relies on the two following lemmas. Note that these lemmas imply a departure from the framework developed in [67], since the condition (DG3a) does not hold.

Lemma 31. *For any $\boldsymbol{v}_h \in \mathbb{P}_n^k(\mathcal{T}_h)^{n+1}$, $\|\mathcal{A}_h^{\{0\}}\boldsymbol{v}_h^n\|_{L^2(\Omega)} \leq C_{\mathrm{tr}} 2^{-1/2} c_0^{1/2} h^{-1/2} (N(\boldsymbol{n})\boldsymbol{v}_h, \boldsymbol{v}_h)_{L^2(\partial\Omega)}^{1/2}$, where*

$$N(\boldsymbol{n}) := c_0 \begin{bmatrix} (\alpha_1^2 + (\alpha_3 - 1)^2)\boldsymbol{n}\otimes\boldsymbol{n} & \boldsymbol{0}_{\boldsymbol{n}} \\ \boldsymbol{0}_{\boldsymbol{n}}^{\mathsf{T}} & \alpha_4^2 + (\alpha_2 - 1)^2 \end{bmatrix},$$

and $C_{\mathrm{tr}} > 0$ is defined in Lemma 30.

Proof. Let $\boldsymbol{w}_h := ((\boldsymbol{w}_h^u)^{\mathsf{T}}, w_h^{\tilde{p}})^{\mathsf{T}} \in \mathbb{P}_n^k(\mathcal{T}_h)^{n+1}$. The definition of $\mathcal{A}_h^{\{0\}}$ yields

$$(\mathcal{A}_h^{\{0\}}\boldsymbol{v}_h^n, \boldsymbol{w}_h)_{L^2(\Omega)} := \frac{1}{2}(M_0(\boldsymbol{n})\boldsymbol{v}_h - A(\boldsymbol{n})\boldsymbol{v}_h, \boldsymbol{w}_h)_{L^2(\partial\Omega)} = \frac{c_0}{2}\int_{\partial\Omega} \begin{pmatrix} \alpha_1\boldsymbol{u}_h\cdot\boldsymbol{n} \\ (\alpha_2-1)\tilde{p} \\ (\alpha_3-1)\boldsymbol{u}_h\cdot\boldsymbol{n} \\ \alpha_4\tilde{p} \end{pmatrix} \cdot \begin{pmatrix} \boldsymbol{w}_h^u\cdot\boldsymbol{n} \\ \boldsymbol{w}_h^u\cdot\boldsymbol{n} \\ w_h^{\tilde{p}} \\ w_h^{\tilde{p}} \end{pmatrix} \mathrm{d}\boldsymbol{x}.$$

The Cauchy–Schwarz inequality then gives $(\mathcal{A}_h^{\{0\}}\boldsymbol{v}_h^n, \boldsymbol{w}_h)_{L^2(\Omega)} \leq \frac{c_0^{1/2}}{\sqrt{2}}(N(\boldsymbol{n})\boldsymbol{v}_h, \boldsymbol{v}_h)_{L^2(\partial\Omega)}^{1/2}\|\boldsymbol{w}_h\|_{L^2(\partial\Omega)}$ and the conclusion follows from Lemma 30. □

Lemma 32. *For any* $\boldsymbol{v}_h \in \mathbb{P}_n^k(\mathcal{T}_h)^{n+1}$,

$$\|\mathcal{A}_h^{\{0\}}\boldsymbol{v}_h + \mathcal{A}_h^{\{\beta\}}\beta(\tilde{p}_h + \boldsymbol{u}_h\cdot\boldsymbol{n})\|_{L^2(\Omega)} \le C_{\mathrm{tr}}2^{-1/2}c_0h^{-1/2}\|\tilde{p}_h - \boldsymbol{u}_h\cdot\boldsymbol{n} - \beta(\tilde{p}_h + \boldsymbol{u}_h\cdot\boldsymbol{n})\|_{L^2(\partial\Omega)},$$

where $C_{\mathrm{tr}} > 0$ *is defined in Lemma 30.*

Proof. Let $\boldsymbol{w}_h := ((\boldsymbol{w}_h^u)^\intercal, w_h^{\tilde{p}})^\intercal \in \mathbb{P}_n^k(\mathcal{T}_h)^{n+1}$. The definition of $\mathcal{A}_h^{\{0\}} + \mathcal{A}_h^{\{\beta\}}$ and the Cauchy–Schwarz inequality yield

$$\begin{aligned}
&(\mathcal{A}_h^{\{0\}}\boldsymbol{v}_h, \boldsymbol{w}_h)_{L^2(\Omega)} + (\mathcal{A}_h^{\{\beta\}}\beta(\tilde{p}_h + \boldsymbol{u}_h\cdot\boldsymbol{n}), \boldsymbol{w}_h)_{L^2(\Omega)}\\
&\qquad := \frac{1}{2}(M_0(\boldsymbol{n})\boldsymbol{v}_h - A(\boldsymbol{n})\boldsymbol{v}_h, \boldsymbol{w}_h)_{L^2(\partial\Omega)} + \frac{1}{2}(\boldsymbol{m}_{\mathcal{B}}(\boldsymbol{n})\beta(\tilde{p}_h + \boldsymbol{u}_h\cdot\boldsymbol{n}), \boldsymbol{w}_h)_{L^2(\partial\Omega)}\\
&\qquad = \frac{c_0}{2}(\tilde{p}_h - \boldsymbol{u}_h\cdot\boldsymbol{n} - \beta(\tilde{p}_h + \boldsymbol{u}_h\cdot\boldsymbol{n}), w_h^{\tilde{p}} - \boldsymbol{w}_h^u\cdot\boldsymbol{n})_{L^2(\partial\Omega)}\\
&\qquad \le \frac{c_0}{\sqrt{2}}\|\tilde{p}_h - \boldsymbol{u}_h\cdot\boldsymbol{n} - \beta(\tilde{p}_h + \boldsymbol{u}_h\cdot\boldsymbol{n})\|_{L^2(\partial\Omega)}\|\boldsymbol{w}_h\|_{L^2(\partial\Omega)},
\end{aligned}$$

and the conclusion follows from Lemma 30. □

The non-boundary terms of $\mathcal{A}_h$, gathered in $\tilde{\mathcal{A}}_h$, are covered by the last lemma below.

Lemma 33. *For any* $\boldsymbol{v}_h \in \mathbb{P}_n^k(\mathcal{T}_h)^{n+1}$,

$$\|\tilde{\mathcal{A}}_h\boldsymbol{v}_h\|_{L^2(\Omega)} \le C_{\mathrm{DG}}h^{-1/2}\||\boldsymbol{u_0}| + c_0\|_{L^\infty(\Omega)}^{1/2}|\boldsymbol{v}_h|_{\mathrm{upw}} + \|A(\nabla_h)\boldsymbol{v}_h + B\boldsymbol{v}_h\|_{L^2(\Omega)},$$

where $C_{\mathrm{DG}} := (\sqrt{2} + \frac{1}{\sqrt{2}})C_{\mathrm{tr}} > 0$ *with* C_{tr} *defined in Lemma 30.*

Proof. This is a standard estimate that relies on the Cauchy–Schwarz and discrete trace inequalities, see [66, Chap. 3 & 7] and [67]. Let $\boldsymbol{w}_h \in \mathbb{P}_n^k(\mathcal{T}_h)^{n+1}$ with $k \in \mathbb{N}^*$. Each of the three terms in (54) is estimated separately. The first term readily yields

$$\sum_{T\in\mathcal{T}_h}(\mathcal{A}\boldsymbol{v}_h, \boldsymbol{w}_h)_{L^2(T)} = (A(\nabla_h)\boldsymbol{v}_h + B\boldsymbol{v}_h, \boldsymbol{w}_h)_{L^2(\Omega)} \le \|A(\nabla_h)\boldsymbol{v}_h + B\boldsymbol{v}_h\|_{L^2(\Omega)}\|\boldsymbol{w}_h\|_{L^2(\Omega)}.$$

For the last two terms, we use the inequality

$$(A(\boldsymbol{n}_F)\boldsymbol{v}_h, \boldsymbol{w}_h)_{L^2(F)} \le (|A(\boldsymbol{n}_F)|\boldsymbol{v}_h, \boldsymbol{v}_h)_{L^2(F)}^{1/2}(|A(\boldsymbol{n}_F)|\boldsymbol{w}_h, \boldsymbol{w}_h)_{L^2(F)}^{1/2}, \tag{B.2}$$

which follows from the fact that the real symmetric matrix A is diagonalizable with $A = P\Lambda P^\intercal$, where $\Lambda := \mathrm{diag}(\boldsymbol{u_0}\cdot\boldsymbol{n} + c_0, \boldsymbol{u_0}\cdot\boldsymbol{n} - c_0, \boldsymbol{u_0}\cdot\boldsymbol{n}, \cdots, \boldsymbol{u_0}\cdot\boldsymbol{n})$ and P is an orthogonal matrix (recall that $|A| := P|\Lambda|P^\intercal$). (This inequality yields the (DG8) condition in [67].) Using (B.2), the Cauchy–Schwarz inequality, and Lemma 30 give

$$\sum_{F\in\mathcal{F}_h^i}(A(\boldsymbol{n}_F)[\![\boldsymbol{v}_h]\!], \{\boldsymbol{w}_h\})_{L^2(F)} \le \sqrt{2}C_{\mathrm{tr}}h^{-1/2}\Big(\max_{F\in\mathcal{F}_h^i}\rho(|A(\boldsymbol{n}_F)|)\Big)^{1/2}|\boldsymbol{v}_h|_{\mathrm{upw}}\|\boldsymbol{w}_h\|_{L^2(\Omega)},$$

where $\rho(|A(\boldsymbol{n}_F)|)$ denotes the spectral radius. Similarly,

$$\frac{1}{2}\sum_{F\in\mathcal{F}_h^i}(|A(\boldsymbol{n}_F)|[\![\boldsymbol{v}_h]\!], [\![\boldsymbol{w}_h]\!])_{L^2(F)} \le \frac{1}{\sqrt{2}}C_{\mathrm{tr}}h^{-1/2}\Big(\max_{F\in\mathcal{F}_h^i}\rho(|A(\boldsymbol{n}_F)|)\Big)^{1/2}|\boldsymbol{v}_h|_{\mathrm{upw}}\|\boldsymbol{w}_h\|_{L^2(\Omega)}.$$

The final estimate follows from $\max_{F\in\mathcal{F}_h^i}\rho(|A(\boldsymbol{n}_F)|) \le \max_{F\in\mathcal{F}_h^i}(|\boldsymbol{u_0}| + c_0) \le \||\boldsymbol{u_0}| + c_0\|_{L^\infty(\Omega)}$. □

Remark 34. Assuming a uniform base flow ($\nabla\boldsymbol{u_0} \equiv 0$) and a finite volume discretization ($k = 0$), $\|A(\nabla_h)\boldsymbol{v}_h + B\boldsymbol{v}_h\|_{L^2(\Omega)} = 0$, and the estimate of Lemma 33 is reduced to $\|\tilde{\mathcal{A}}_h\boldsymbol{v}_h\|_{L^2(\Omega)} \le C_{\mathrm{DG}}h^{-1/2}(|\boldsymbol{u_0}| + c_0)^{1/2}|\boldsymbol{v}_h|_{\mathrm{upw}}$, which is used in Sec. 4 to derive a sufficient stability condition using an energy method.

Appendix C. Proofs of stability conditions

Proof. (Proposition 21) The proof follows the energy method, in the spirit of the analysis carried out at the continuous and semi-discrete levels in Secs. 2.3 and 4.3. A comprehensive analysis of the energy method to derive CFL-type stability condition for coercive problems can be found in [75]. Note that the stability conditions derived in [75] cannot be directly applied herein since $\mathcal{A}_h$ is not coercive in the sense of [75, Eq. 3.2], see (37). See also [65, Chap. 6], [66, § 7.5.2], and [76, Chap. 7].

Given the expression of the continuous energy (14), we define the discrete energy as $\mathcal{E}_h^n := \|\boldsymbol{v}_h^n\|_{L^2(\Omega)}^2$. By taking the scalar product of (52) with $\boldsymbol{v}_h^n$ and using the identity $ab = \frac{1}{2}a^2 + \frac{1}{2}b^2 - \frac{1}{2}(a-b)^2$, one obtains the standard discrete energy balance [75, Eq. 3.4] $\frac{1}{2}\mathcal{E}_h^{n+1} = \frac{1}{2}\mathcal{E}_h^n + \frac{1}{2}\|\boldsymbol{v}_h^{n+1} - \boldsymbol{v}_h^n\|_{L^2(\Omega)}^2 - \Delta t(\mathcal{A}_h\boldsymbol{v}_h^n, \boldsymbol{v}_h^n)$. The expression of $(\mathcal{A}_h\boldsymbol{v}_h, \boldsymbol{v}_h)_{L^2(\Omega)}$ given by (37) yields

$$\frac{1}{2}\mathcal{E}_h^{n+1} = \frac{1}{2}\mathcal{E}_h^n + \frac{1}{2}\|\boldsymbol{v}_h^{n+1} - \boldsymbol{v}_h^n\|_{L^2(\Omega)}^2 - \frac{\Delta t}{2}(C(\boldsymbol{u_0})\boldsymbol{v}_h^n, \boldsymbol{v}_h^n)_{L^2(\Omega)} - \frac{\Delta t}{2}|\boldsymbol{v}_h^n|_{\mathrm{upw}}^2 - \frac{\Delta t}{2}(M_0(\boldsymbol{n})\boldsymbol{v}_h^n, \boldsymbol{v}_h^n)_{L^2(\partial\Omega)},$$

where each term has a clear interpretation: $\frac{1}{2}\|\boldsymbol{v}_h^{n+1} - \boldsymbol{v}_h^n\|_{L^2(\Omega)}^2$ is the anti-dissipation due to the explicit nature of the time-marching scheme; $-(C(\boldsymbol{u_0})\boldsymbol{v}_h^n, \boldsymbol{v}_h^n)_{L^2(\Omega)}$ is the contribution of a non-constant base flow $\boldsymbol{u_0}$; $-|\boldsymbol{v}_h^n|_{\mathrm{upw}}^2$ is the dissipation due to the upwind flux (would be null with a centered flux); $-(M_0(\boldsymbol{n})\boldsymbol{v}_h^n, \boldsymbol{v}_h^n)_{L^2(\partial\Omega)}$ is the dissipation due to the IBC.

The key step of the proof is to estimate the anti-dissipation term $\frac{1}{2}\|\boldsymbol{v}_h^{n+1} - \boldsymbol{v}_h^n\|_{L^2(\Omega)}^2$. The decomposition of $\mathcal{A}_h$ readily yields the estimate

$$\frac{1}{2}\|\boldsymbol{v}_h^{n+1} - \boldsymbol{v}_h^n\|_{L^2(\Omega)}^2 = \frac{\Delta t^2}{2}\|\mathcal{A}_h\boldsymbol{v}_h^n\|_{L^2(\Omega)}^2 \le \Delta t^2\|\tilde{\mathcal{A}}_h\boldsymbol{v}_h^n\|_{L^2(\Omega)}^2 + \Delta t^2\|\mathcal{A}_h^{\{0\}}\boldsymbol{v}_h^n\|_{L^2(\Omega)}^2,$$

where the energy production that occurs at the impedance boundary is bounded by $\|\mathcal{A}_h^{\{0\}}\boldsymbol{v}_h^n\|_{L^2(\Omega)}^2$. The estimate of this term is provided by Lemma 31, which does not require the finite volume hypothesis. Lemma 33 provides a bound for $\|\tilde{\mathcal{A}}_h\boldsymbol{v}_h^n\|_{L^2(\Omega)}$ that *does* need the finite volume hypothesis. Using both Lemmas 31 and 33, the discrete energy balance becomes

$$\frac{1}{2}\mathcal{E}_h^{n+1} \le \frac{1}{2}\big(1 - \Delta t\min_{x\in\Omega}\lambda_{\min}(\boldsymbol{u_0})\big)\mathcal{E}_h^n - \frac{\Delta t}{2}\big(1 - 2C_{\mathrm{DG}}^2\Delta t(c_0 + |\boldsymbol{u_0}|)h^{-1}\big)|\boldsymbol{v}_h|_{\mathrm{upw}}^2 - \frac{\Delta t}{2}(I(\boldsymbol{n})\boldsymbol{v}_h, \boldsymbol{v}_h)_{L^2(\partial\Omega)},$$

where $I(\boldsymbol{n}) := \frac{1}{2}(M_0(\boldsymbol{n}) + M_0(\boldsymbol{n})^\intercal) - \frac{C_{\mathrm{tr}}^2}{2}\mathrm{CFL}(N(\boldsymbol{n}) + N(\boldsymbol{n})^\intercal)$ so that $(I(\boldsymbol{n})\boldsymbol{v}_h, \boldsymbol{v}_h)_{\mathbb{R}^{n+1}} = (\check{I}(\boldsymbol{n})\check{\boldsymbol{v}}_h, \check{\boldsymbol{v}}_h)_{\mathbb{R}^2}$ with $\check{\boldsymbol{v}}_h := (\boldsymbol{u}_h\cdot\boldsymbol{n}, \tilde{p}_h)^\intercal$ and

$$\check{I}(\boldsymbol{n}) := c_0\begin{bmatrix}\big(\alpha_1 - C_{\mathrm{tr}}^2\mathrm{CFL}(\alpha_1^2 + (\alpha_3-1)^2)\big) & \frac{\alpha_2+\alpha_3}{2} \\ \frac{\alpha_2+\alpha_3}{2} & \alpha_4 - C_{\mathrm{tr}}^2\mathrm{CFL}(\alpha_4^2 + (\alpha_2-1)^2)\end{bmatrix}.$$

The conclusion then follows from Lemma 19. □

The proof of Proposition 28 is similar, but relies on an energy balance for the additional variables φ_h, given herein. (Although energy balances associated with diffusive representation of positive-real functions are available in the literature, this is not the case for bounded-real functions.) Let $\hat{\beta}$ be given by (65) and denote $b = \beta \star a$ for concision. The realization of β is, as seen in Sec. 3.2,

$$\begin{cases}\partial_t\varphi(t,-\xi) &= -\xi\varphi(t,-\xi) + a(t),\ \varphi(0,-\xi) = 0\\ b(t) &= \int_{\xi^{\min}}^{\xi^{\max}}\varphi(t,-\xi)\,\mathrm{d}\mu(\xi),\end{cases} \tag{C.1}$$

The energy of this realization can be defined as

$$\mathcal{E}_\beta(t) := \|\mu\|_{L^1}\int_{\xi^{\min}}^{\xi^{\max}}\|\varphi_h(t,-\xi)\|_{L^2(\partial\Omega)}^2\frac{\mathrm{d}\mu}{\xi}, \tag{C.2}$$

leading to the energy balance

$$\frac{1}{2}b^2 + \frac{1}{2}\frac{\mathrm{d}}{\mathrm{d}t}\mathcal{E}_\beta \le \frac{1}{2}\|\mu\|_{L^1}\|\frac{\mu}{\xi^2}\|_{L^1}a^2 - \frac{\|\mu\|_{L^1}}{2}\int_{\xi^{\min}}^{\xi^{\max}}(-\xi\varphi_h + a)^2\frac{\mathrm{d}\mu}{\xi^2}, \tag{C.3}$$

from which we deduce that a sufficient condition for $\hat{\beta}(s)$ to be bounded-real (i.e. for β to be an admissible scattering operator) is that the measure μ satisfies $\|\mu\|_{L^1}\|\frac{\mu}{\xi^2}\|_{L^1} \le 1$. Using (C.3), we can then prove Proposition 28.

Proof. (Proposition 28) The proof relies on an energy analysis similar to that of Proposition 21 with one additional technicality: the energy is not reduced to $\|\boldsymbol{v}_h\|^2_{L^2(\Omega)}$ but must include a contribution $\mathcal{E}_\beta$ from the diffusive variable φ_h defined as (C.2). For the sake of clarity, we first write down the semi-discrete energy balance before considering its discretization.

(Semi-discrete energy balance) Using the energy balance associated with $\mathcal{E}_\beta$ (C.3), the semi-discrete energy balances reads

$$\begin{cases} \frac{1}{2}\frac{\mathrm{d}}{\mathrm{d}t}\mathcal{E}_\beta & \leq \frac{1}{2}\big((\tilde{p}_h+\boldsymbol{u}_h\cdot\boldsymbol{n})^2-\beta(\tilde{p}_h+\boldsymbol{u}_h\cdot\boldsymbol{n})^2\big)-\frac{\|\mu\|_{L^1}}{2}\int_{\xi^{\min}}^{\xi^{\max}}(-\xi\varphi_h+\tilde{p}_h+\boldsymbol{u}_h\cdot\boldsymbol{n})^2\frac{\mathrm{d}\mu}{\xi^2} \\ \frac{1}{2}\frac{\mathrm{d}}{\mathrm{d}t}\|\boldsymbol{v}_h\|^2_{L^2(\Omega)} & = -\frac{1}{2}(C(\boldsymbol{u_0})\boldsymbol{v}_h,\boldsymbol{v}_h)_{L^2(\Omega)}-\frac{1}{2}|\boldsymbol{v}_h|^2_{\mathrm{upw}}-\frac{1}{2}(M_0(\boldsymbol{n})\boldsymbol{v}_h,\boldsymbol{v}_h)_{L^2(\partial\Omega)}-(\mathcal{A}_h^{\{\beta\}}\boldsymbol{v}_h,\boldsymbol{v}_h)_{L^2(\Omega)}. \end{cases}$$

The identity (64) enables to rewrite the second line to explicit the energy exchange between the diffusive variables φ_h and the acoustic field $\boldsymbol{v}$:

$$\begin{cases} \frac{1}{2}\frac{\mathrm{d}}{\mathrm{d}t}\mathcal{E}_\beta & \leq \frac{1}{2}\big((\tilde{p}_h+\boldsymbol{u}_h\cdot\boldsymbol{n})^2-\beta(\tilde{p}_h+\boldsymbol{u}_h\cdot\boldsymbol{n})^2\big)-\frac{\|\mu\|_{L^1}}{2}\int_{\xi^{\min}}^{\xi^{\max}}(-\xi\varphi_h+\tilde{p}_h+\boldsymbol{u}_h\cdot\boldsymbol{n})^2\frac{\mathrm{d}\mu}{\xi^2} \\ \frac{1}{2}\frac{\mathrm{d}}{\mathrm{d}t}\|\boldsymbol{v}_h\|^2_{L^2(\Omega)} & = -\frac{1}{2}(C(\boldsymbol{u_0})\boldsymbol{v}_h,\boldsymbol{v}_h)_{L^2(\Omega)}-\frac{1}{2}|\boldsymbol{v}_h|^2_{\mathrm{upw}}-\frac{c_0}{4}\big(\|\tilde{p}_h+\boldsymbol{u}_h\cdot\boldsymbol{n}\|^2_{L^2(\partial\Omega)}-\|\beta(\tilde{p}_h+\boldsymbol{u}_h\cdot\boldsymbol{n})\|^2_{L^2(\partial\Omega)}\big) \\ & \quad -\frac{c_0}{4}\|\tilde{p}_h-\boldsymbol{u}_h\cdot\boldsymbol{n}-\beta(\tilde{p}_h+\boldsymbol{u}_h\cdot\boldsymbol{n})\|^2_{L^2(\partial\Omega)}. \end{cases}$$

The semi-discrete energy balance is obtained by integrating the first inequality over $\partial\Omega$, multiplying it by $c_0/2$ and summing it with the second one

$$\begin{aligned} \frac{1}{2}\frac{\mathrm{d}}{\mathrm{d}t}\mathcal{E}_h \leq & -\frac{1}{2}(C(\boldsymbol{u_0})\boldsymbol{v}_h,\boldsymbol{v}_h)_{L^2(\Omega)}-\frac{1}{2}|\boldsymbol{v}_h|^2_{\mathrm{upw}}-\frac{c_0}{4}\|\mu\|_{L^1}\int_{\xi^{\min}}^{\xi^{\max}}\|-\xi\varphi_h+\tilde{p}_h+\boldsymbol{u}_h\cdot\boldsymbol{n}\|^2_{L^2(\partial\Omega)}\frac{\mathrm{d}\mu}{\xi^2} \\ & -\frac{c_0}{4}\|\tilde{p}_h-\boldsymbol{u}_h\cdot\boldsymbol{n}-\beta(\tilde{p}_h+\boldsymbol{u}_h\cdot\boldsymbol{n})\|^2_{L^2(\partial\Omega)}, \end{aligned} \tag{C.4}$$

where the extended energy is defined as $\mathcal{E}_h := \|\boldsymbol{v}_h\|^2_{L^2(\Omega)}+\frac{c_0}{2}\mathcal{E}_\beta$. The third and fourth terms of the right-hand side express the dissipation that occurs at the impedance boundary (here, $\partial\Omega$).

(Discrete energy balance) The explicit Euler discretization of (66) leads to

$$\begin{aligned} & (\boldsymbol{v}_h^{n+1}-\boldsymbol{v}_h^n,\boldsymbol{v}_h^n)_{L^2(\Omega)}+\frac{c_0}{2}\|\mu\|_{L^1}\int_{\xi^{\min}}^{\xi^{\max}}(\varphi_h^{n+1}-\varphi_h^n,\varphi_h^n)_{L^2(\partial\Omega)}\frac{\mathrm{d}\mu}{\xi} \\ & \leq -\frac{\Delta t}{2}(C(\boldsymbol{u_0})\boldsymbol{v}_h^n,\boldsymbol{v}_h^n)_{L^2(\Omega)}-\frac{\Delta t}{2}|\boldsymbol{v}_h^n|^2_{\mathrm{upw}}-\frac{c_0}{4}\Delta t\|\mu\|_{L^1}\int_{\xi^{\min}}^{\xi^{\max}}\|-\xi\varphi_h^n+\tilde{p}_h^n+\boldsymbol{u}_h^n\cdot\boldsymbol{n}\|^2_{L^2(\partial\Omega)}\frac{\mathrm{d}\mu}{\xi^2} \\ & \quad -\frac{c_0}{4}\Delta t\|\tilde{p}_h^n-\boldsymbol{u}_h^n\cdot\boldsymbol{n}-\beta(\tilde{p}_h^n+\boldsymbol{u}_h^n\cdot\boldsymbol{n})\|^2_{L^2(\partial\Omega)}, \end{aligned}$$

and the identity $(a-b)b=\frac{1}{2}a^2-\frac{1}{2}b^2-\frac{1}{2}(a-b)^2$ enables to rewrite this with the discrete extended energy $\mathcal{E}_h^n := \|\boldsymbol{v}_h^n\|^2_{L^2(\Omega)}+\frac{c_0}{2}\|\mu\|_{L^1}\int_{\xi^{\min}}^{\xi^{\max}}\|\varphi_h^n\|^2_{L^2(\partial\Omega)}\frac{\mathrm{d}\mu}{\xi}$:

$$\begin{aligned} \frac{1}{2}\mathcal{E}_h^{n+1} \leq & \frac{1}{2}\mathcal{E}_h^n-\frac{\Delta t}{2}(C(\boldsymbol{u_0})\boldsymbol{v}_h^n,\boldsymbol{v}_h^n)_{L^2(\Omega)}-\frac{\Delta t}{2}|\boldsymbol{v}_h^n|^2_{\mathrm{upw}}-\frac{c_0}{4}\Delta t\|\mu\|_{L^1}\int_{\xi^{\min}}^{\xi^{\max}}\|-\xi\varphi_h^n+\tilde{p}_h^n+\boldsymbol{u}_h^n\cdot\boldsymbol{n}\|^2_{L^2(\partial\Omega)}\frac{\mathrm{d}\mu}{\xi^2} \\ & -\frac{c_0}{4}\Delta t\|\tilde{p}_h^n-\boldsymbol{u}_h^n\cdot\boldsymbol{n}-\beta(\tilde{p}_h^n+\boldsymbol{u}_h^n\cdot\boldsymbol{n})\|^2_{L^2(\partial\Omega)} \\ & +\frac{1}{2}\|\boldsymbol{v}_h^{n+1}-\boldsymbol{v}_h^n\|^2_{L^2(\Omega)}+\frac{c_0}{2}\|\mu\|_{L^1}\int_{\xi^{\min}}^{\xi^{\max}}\frac{1}{2}\|\varphi_h^{n+1}-\varphi_h^n\|^2_{L^2(\partial\Omega)}\frac{\mathrm{d}\mu}{\xi}. \end{aligned}$$

The task is now to estimate the two anti-dissipative terms so that they can be provably controlled by the three dissipative ones. Let us bound the anti-dissipation on $\boldsymbol{v}_h$ with Lemmas 32 and 33:

$$\begin{aligned} \frac{1}{2}\|\boldsymbol{v}_h^{n+1}-\boldsymbol{v}_h^n\|^2_{L^2(\Omega)} &= \frac{\Delta t^2}{2}\|\tilde{\mathcal{A}}_h\boldsymbol{v}_h+\mathcal{A}_h^{\{0\}}\boldsymbol{v}_h+\mathcal{A}_h^{\{\beta\}}\beta(\tilde{p}_h+\boldsymbol{u}_h\cdot\boldsymbol{n})\|^2_{L^2(\Omega)} \\ &\leq \Delta t^2\|\tilde{\mathcal{A}}_h\boldsymbol{v}_h\|^2_{L^2(\Omega)}+\Delta t^2\|\mathcal{A}_h^{\{0\}}\boldsymbol{v}_h+\mathcal{A}_h^{\{\beta\}}\beta(\tilde{p}_h+\boldsymbol{u}_h\cdot\boldsymbol{n})\|^2_{L^2(\Omega)} \end{aligned}$$

$$\leq C_{\mathrm{DG}}^2 \Delta t^2 (c_0 + |\boldsymbol{u_0}|) h^{-1} |\boldsymbol{v}_h|_{\mathrm{upw}}^2 + \frac{C_{\mathrm{tr}}^2}{2} \Delta t^2 c_0^2 h^{-1} \|\tilde{p}_h - \boldsymbol{u}_h \cdot \boldsymbol{n} - \beta(\tilde{p}_h + \boldsymbol{u}_h \cdot \boldsymbol{n})\|_{L^2(\partial\Omega)}^2.$$

Using Lemma 32 and the identity $\frac{1}{2}\|\varphi_h^{n+1} - \varphi_h^n\|_{L^2(\partial\Omega)}^2 = \frac{\Delta t^2}{2}\|-\xi\varphi_h^n + \tilde{p}_h + \boldsymbol{u}_h \cdot \boldsymbol{n}\|_{L^2(\partial\Omega)}^2$, the energy balance becomes

$$\begin{aligned}
\frac{1}{2}\mathcal{E}_h^{n+1} \leq \frac{1}{2}\mathcal{E}_h^n - \frac{\Delta t}{2}(C(\boldsymbol{u_0})\boldsymbol{v}_h^n, \boldsymbol{v}_h^n)_{L^2(\Omega)} - \frac{\Delta t}{2}\left(1 - 2C_{\mathrm{DG}}^2 \Delta t (c_0 + |\boldsymbol{u_0}|) h^{-1}\right) |\boldsymbol{v}_h^n|_{\mathrm{upw}}^2 \\
- \frac{c_0}{4}\Delta t \|\mu\|_{L^1} \int_{\xi^{\min}}^{\xi^{\max}} \|-\xi\varphi_h^n + \tilde{p}_h^n + \boldsymbol{u}_h^n \cdot \boldsymbol{n}\|_{L^2(\partial\Omega)}^2 \left(\frac{1}{\xi} - \Delta t\right) \frac{\mathrm{d}\mu}{\xi} \\
- \left(\frac{c_0}{4}\Delta t - \frac{C_{\mathrm{tr}}^2}{2}\Delta t^2 c_0^2 h^{-1}\right) \|\tilde{p}_h^n - \boldsymbol{u}_h^n \cdot \boldsymbol{n} - \beta(\tilde{p}_h^n + \boldsymbol{u}_h^n \cdot \boldsymbol{n})\|_{L^2(\partial\Omega)}^2,
\end{aligned}$$

which enables to conclude. □

Appendix D. Implementation details

The implemented numerical scheme is a standard DG method. It is nodal in the sense that on each of the N_K triangles the solution $\boldsymbol{v}_h$ is computed through its components in the Lagrange basis associated with the N_p points described in [69, § 6.1]. For a N-th order DG, $N_p = N(N+1)/2$. Let us now assume that the linear TDIBC is given by

$$\tilde{\mathcal{B}}(w)(t) = \tilde{\beta}_\infty w(t) + \mathcal{Q}_1(w)(t) + \mathcal{Q}_2(w)(t - \tilde{\tau}),$$

which corresponds to the TDIBC (31), where w is a shorthand for "$\tilde{p}_h + \boldsymbol{u}_h \cdot \boldsymbol{n}$". The global assembly is performed in three steps.

(1) Spatial discretization. The global DG formulation reads

$$M\dot{\boldsymbol{v}} + K\boldsymbol{v} = F_s \boldsymbol{v}_s + F_{\mathcal{Q}_1}\mathcal{Q}_1(C_{\Gamma_z}\boldsymbol{v}) + F_{\mathcal{Q}_2}\mathcal{Q}_2(C_{\Gamma_z}\boldsymbol{v})(t - \tilde{\tau}), \tag{D.1}$$

where $\boldsymbol{v} := (\boldsymbol{v}_h(\boldsymbol{x}_i^k))_{i,k}$ is the discrete acoustic field ($3N_K N_p$ elements), and M, K, and F are the standard mass, stiffness, and flux DG matrices. The IBC manifests itself through the (rectangular) observation matrix C_{Γ_z} that are associated with the DoF that belong to the impedance boundary Γ_z. The operators $\mathcal{Q}_i$ are applied to each component of the vector $C_{\Gamma_z}\boldsymbol{v}$ of length N_{Γ_z}. Note that, at this stage, the actual definition of the operators $\mathcal{Q}_i$ does not matter.

(2) State-space realization. By construction, the operators $\mathcal{Q}_i$ have a state-space realization with state vector $\boldsymbol{\varphi} := (\varphi_i)_{i \in [\![1, N_\varphi]\!]}$ of length N_φ

$$\begin{aligned}
\dot{\boldsymbol{\varphi}}(t) &= A\boldsymbol{\varphi}(t) + Bw(t) \\
\mathcal{Q}_i(w)(t) &= C_{\mathcal{Q}_i}\boldsymbol{\varphi}(t) + D_{\mathcal{Q}_i} w(t),
\end{aligned} \tag{D.2}$$

where $A = \mathrm{diag}(s_n, -\xi_k)_{n,k}$ is a diagonal $N_\varphi \times N_\varphi$ matrix, $B = (1)_{i \in [\![1, N_\varphi]\!]}$, $C_{\mathcal{Q}_i} = (\tilde{r}_{n,i}, \tilde{\mu}_{k,i})_{n,k}$, and $D_{\mathcal{Q}_i} = 0$. Then, injecting (D.2) into (D.1) leads to the following formulation

$$M\dot{\boldsymbol{v}}(t) + K\boldsymbol{v}(t) = F_s\boldsymbol{v}_s(t) + B_\tau(C_\tau\boldsymbol{v})(t - \tilde{\tau}), \tag{D.3}$$

where $\boldsymbol{v}$ now denotes the extended state $\boldsymbol{v} := ((\boldsymbol{v}_h(\boldsymbol{x}_i^k))_{i,k}, (\boldsymbol{\varphi}^k)_k)$ of length $3N_K N_p + N_\varphi N_{\Gamma_z}$ and the matrices are obtained by concatenation (the same notations M, K, and F_s are used for the sake of concision). For instance, $C_\tau \boldsymbol{v} = (\boldsymbol{\varphi}^k)_k = (\varphi_j^k)_{k,j}$ is of length $N_\varphi N_{\Gamma_z}$. This is a finite-dimensional delay differential equation that can be advanced in time with a variety of methods.

(3) Time delay computation. Following Sec. 3.3.2, each of the $N_\varphi N_{\Gamma_z}$ variables φ_j^k are delayed through a monodimensional DG on $(-l_{\tilde{\tau}}, 0)$ that reads

$$\begin{aligned}
M_{\mathrm{DG1D}}\dot{\boldsymbol{\psi}}_j^k + K_{\mathrm{DG1D}}\boldsymbol{\psi}_j^k &= F_{\mathrm{DG1D}}\varphi_j^k \\
\varphi_j^k(t - \tilde{\tau}) &= C_{\mathrm{DG1D}}\boldsymbol{\psi}_j^k(t),
\end{aligned} \tag{D.4}$$

where $\boldsymbol{\psi}_j^k$ is vector of length N_ψ. Note that (D.4) can be written as (D.2), i.e. it is a state-space realization of the time delay. Combining (D.3) with (D.4) leads to the final global formulation $M\dot{\boldsymbol{v}} + K\boldsymbol{v} = F_s\boldsymbol{v}_s$, where the vector $\boldsymbol{v}$, of length $3N_K N_p + (N_\psi + 1)N_\varphi N_{\Gamma_z}$, now includes the acoustic field $[\boldsymbol{v}_h(\boldsymbol{x}_i^k)]_{i,k}$ as well as the additional variables $(\varphi_j^k)_{k,j}$ and $(\boldsymbol{\psi}_j^k)_{k,j}$.

The addition of a nonlinear term $\mathcal{Q}_{\mathrm{nl}}$ to the discrete model $\tilde{\mathcal{B}}$ does not change the assembly process described above, which yields $M\dot{\boldsymbol{v}} + K\boldsymbol{v} = F_s\boldsymbol{v}_s + F_{\mathcal{Q}_{\mathrm{nl}}}\mathcal{Q}_{\mathrm{nl}}(C_{\mathcal{Q}_{\mathrm{nl}}}\boldsymbol{v})$. In the case of (25), $\mathcal{Q}_{\mathrm{nl}}(w)$ can be directly computed. If it exists, $\mathcal{Q}_{\mathrm{nl}}(w)$ can be replaced by its nonlinear state-space realization.

References

[1] C. Tam, Computational Aeroacoustics: A Wave Number Approach, Cambridge University Press, Cambridge, 2012.
[2] P.M. Morse, K.U. Ingard, Theoretical Acoustics, Princeton University Press, Princeton, 1968.
[3] L.E. Kinsler, A.R. Frey, Fundamentals of Acoustics, second ed., John Wiley & Sons, New York, 1962.
[4] L. Schwartz, Mathematics for the Physical Sciences, Hermann, Paris, 1966.
[5] F. Monteghetti, D. Matignon, E. Piot, L. Pascal, Design of broadband time-domain impedance boundary conditions using the oscillatory-diffusive representation of acoustical models, J. Acoust. Soc. Am. 140 (2016) 1663–1674.
[6] T.H. Melling, The acoustic impedance of perforates at medium and high sound pressure levels, J. Sound Vib. 29 (1973) 1–65.
[7] A. Cummings, Transient and multiple frequency sound transmission through perforated plates at high amplitude, J. Acoust. Soc. Am. 79 (1986) 942–951.
[8] M. Meissner, The influence of acoustic nonlinearity on absorption properties of Helmholtz resonators. Part I. Theory, Arch. Acoust. 24 (1999) 179–190.
[9] Q. Zhang, D.J. Bodony, Numerical investigation and modelling of acoustically excited flow through a circular orifice backed by a hexagonal cavity, J. Fluid Mech. 693 (2012) 367–401.
[10] R. Kirby, A. Cummings, The impedance of perforated plates subjected to grazing gas flow and backed by porous media, J. Sound Vib. 217 (1998) 619–636.
[11] Q. Zhang, D.J. Bodony, Numerical investigation of a honeycomb liner grazed by laminar and turbulent boundary layers, J. Fluid Mech. 792 (2016) 936–980.
[12] S. Laurens, E. Piot, A. Bendali, M. Fares, S. Tordeux, Effective conditions for the reflection of an acoustic wave by low-porosity perforated plates, J. Fluid Mech. 743 (2014) 448–480.
[13] H.H. Hubbard (Ed.), Aeroacoustics of Flight Vehicles: Theory and Practice. Volume 2: Noise Control, NASA, 1991, WRDC 90-3052.
[14] L. Cremer, Theory regarding the attenuation of sound transmitted by air in a rectangular duct with an absorbing wall, and the maximum attenuation constant produced during this process, Acustica 3 (1953) 249–263 (in German).
[15] D.C. Pridmore-Brown, Sound propagation in a fluid flowing through an attenuating duct, J. Fluid Mech. 4 (1958) 393–406.
[16] B. Tester, The propagation and attenuation of sound in lined ducts containing uniform or 'plug' flow, J. Sound Vib. 28 (1973) 151–203.
[17] D. Khamis, E.J. Brambley, Viscous effects on the acoustics and stability of a shear layer over an impedance wall, J. Fluid Mech. 810 (2017) 489–534.
[18] M.G. Jones, W.R. Watson, T.L. Parrott, Benchmark data for evaluation of aeroacoustic propagation codes with grazing flow, in: 11th AIAA/CEAS Aeroacoustics Conference, Monterey, CA, USA, 2005, AIAA Paper 2005-2853.
[19] Y. Özyörük, L.N. Long, M.G. Jones, Time-domain numerical simulation of a flow-impedance tube, J. Comput. Phys. 146 (1998) 29–57.
[20] J. Bin, M.Y. Hussaini, S. Lee, Broadband impedance boundary conditions for the simulation of sound propagation in the time domain, J. Acoust. Soc. Am. 125 (2009) 664–675.
[21] X. Liu, X. Huang, X. Zhang, Stability analysis and design of time-domain acoustic impedance boundary conditions for lined duct with mean flow, J. Acoust. Soc. Am. 136 (2014) 2441–2452.
[22] S. Zhong, X. Zhang, X. Huang, A controllable canonical form implementation of time domain impedance boundary conditions for broadband aeroacoustic computation, J. Comput. Phys. 313 (2016) 713–725.
[23] D. Botteldooren, Finite-difference time-domain simulation of low-frequency room acoustic problems, J. Acoust. Soc. Am. 98 (1995) 3302–3308.
[24] B. Cotté, P. Blanc-Benon, Time-domain simulations of sound propagation in a stratified atmosphere over an impedance ground, J. Acoust. Soc. Am. 125 (2009) EL202–EL207.
[25] C. Richter, Liner Impedance Modeling in the Time Domain with Flow, Ph.D. thesis, Technische Universität Berlin, 2010.
[26] C. Richter, J.A. Hay, N. Schönwald, S. Busse, F. Thiele, et al., A review of time-domain impedance modelling and applications, J. Sound Vib. 330 (2011) 3859–3873.
[27] R. Troian, D. Dragna, C. Bailly, M.-A. Galland, Broadband liner impedance eduction for multimodal acoustic propagation in the presence of a mean flow, J. Sound Vib. 392 (2017) 200–216.
[28] G. Gabard, E. Brambley, A full discrete dispersion analysis of time-domain simulations of acoustic liners with flow, J. Comput. Phys. 273 (2014) 310–326.
[29] R. Astley, R. Sugimoto, P. Mustafi, Computational aero-acoustics for fan duct propagation and radiation. Current status and application to turbofan liner optimisation, J. Sound Vib. 330 (2011) 3832–3845.
[30] C. Scalo, J. Bodart, S.K. Lele, Compressible turbulent channel flow with impedance boundary conditions, Phys. Fluids 27 (2015).
[31] S. Olivetti, R.D. Sandberg, B.J. Tester, Direct numerical simulation of turbulent flow with an impedance condition, J. Sound Vib. 344 (2015) 28–37.
[32] S. Jaensch, C. Sovardi, W. Polifke, On the robust, flexible and consistent implementation of time domain impedance boundary conditions for compressible flow simulations, J. Comput. Phys. 314 (2016) 145–159.
[33] Q. Douasbin, C. Scalo, L. Selle, T. Poinsot, Delayed-time domain impedance boundary conditions (d-tdibc), J. Comput. Phys. 371 (2018) 50–66.
[34] P. Tudisco, R. Ranjan, S. Menon, S. Jaensch, W. Polifke, Application of the time-domain impedance boundary condition to large-eddy simulation of combustion instability in a shear-coaxial high pressure combustor, Flow Turbul. Combust. 99 (2017) 185–207.
[35] Z. Abbas, S. Nicaise, The multidimensional wave equation with generalized acoustic boundary conditions I: Strong stability, SIAM J. Control Optim. 53 (2015) 2558–2581.
[36] P. Grabowski, Stabilization of wave equation using standard/fractional derivative in boundary damping, in: Advances in the Theory and Applications of Non-integer Order Systems: 5th Conference on Non-integer Order Calculus and Its Applications, Springer, Cracow, Poland, 2013.
[37] J.-M. Wang, B.-Z. Guo, M. Krstic, Wave equation stabilization by delays equal to even multiples of the wave propagation time, SIAM J. Control Optim. 49 (2011) 517–554.
[38] S.V. Yuferev, N. Ida, Surface Impedance Boundary Conditions: A Comprehensive Approach, CRC Press, Boca Raton, 2010.
[39] S. Chun, J. Hesthaven, High-order accurate thin layer approximations for time-domain electromagnetics. Part I: General metal backed coatings, J. Comput. Appl. Math. 231 (2009) 598–611.
[40] R. Hiptmair, M. López-Fernández, A. Paganini, Fast convolution quadrature based impedance boundary conditions, J. Comput. Appl. Math. 263 (2014) 500–517.
[41] R. Brockett, Finite Dimensional Linear Systems, John Wiley and Sons, New York, 1970.
[42] R.F. Curtain, H. Zwart, An Introduction to Infinite-Dimensional Linear Systems Theory, Springer, New York, 1995.
[43] D. Dragna, P. Pineau, P. Blanc-Benon, A generalized recursive convolution method for time-domain propagation in porous media, J. Acoust. Soc. Am. 138 (2015) 1030–1042.
[44] C. Lubich, A. Ostermann, Runge–Kutta methods for parabolic equations and convolution quadrature, Math. Comput. 60 (1993) 105–131.
[45] S. Sauter, M. Schanz, Convolution quadrature for the wave equation with impedance boundary conditions, J. Comput. Phys. 334 (2017) 442–459.
[46] S.W. Rienstra, Impedance models in time domain, including the extended Helmholtz resonator model, in: 12th AIAA/CEAS Aeroacoustics Conference, Cambridge, MA, USA, 2006, AIAA Paper 2006-2686.
[47] K.-Y. Fung, H. Ju, Time-domain impedance boundary conditions for computational acoustics and aeroacoustics, Int. J. Comput. Fluid Dyn. 18 (2004) 503–511.
[48] P. Delorme, P. Mazet, C. Peyret, Y. Ventribout, Computational aeroacoustics applications based on a discontinuous Galerkin method, C. R., Méc. 333 (2005) 676–682.

[49] Y. Ventribout, Contrôle des perturbations aéroacoustiques par impédances de parois: application à un modèle de matériaux poreux, Ph.D. thesis, Ecole nationale superieure de l'aéronautique et de l'espace, Toulouse, 2006.
[50] E.J. Beltrami, M.R. Wohlers, Distributions and the Boundary Values of Analytic Functions, Academic Press, New York, 1966.
[51] A. Zemanian, Distribution Theory and Transform Analysis, McGraw-Hill, 1965.
[52] R. Lozano, B. Brogliato, O. Egeland, B. Maschke, Dissipative Systems Analysis and Control: Theory and Applications, Springer-Verlag, London, 2000.
[53] S. Benzoni-Gavage, D. Serre, Multi-dimensional Hyperbolic Partial Differential Equations: First-order Systems and Applications, Oxford University Press, Oxford, 2007.
[54] E.J. Brambley, Fundamental problems with the model of uniform flow over acoustic linings, J. Sound Vib. 322 (2009) 1026–1037.
[55] R.H. Cantrell, R.W. Hart, Interaction between sound and flow in acoustic cavities: mass, momentum, and energy considerations, J. Acoust. Soc. Am. 36 (1964) 697–706.
[56] T.W. Gamelin, Complex Analysis, Springer-Verlag, New York, 2001.
[57] S.W. Rienstra, D.K. Singh, Nonlinear asymptotic impedance model for a Helmholtz resonator of finite depth, AIAA J. (2018) 1–11.
[58] B. Lombard, D. Matignon, Diffusive approximation of a time-fractional Burger's equation in nonlinear acoustics, SIAM J. Appl. Math. 76 (2016) 1765–1791.
[59] T. Coleman, Y. Li, An interior trust region approach for nonlinear minimization subject to bounds, SIAM J. Optim. 6 (1996) 418–445.
[60] B. Gustavsen, A. Semlyen, Rational approximation of frequency domain responses by vector fitting, IEEE Trans. Power Deliv. 14 (1999) 1052–1061.
[61] J.-P. Richard, Time-delay systems: an overview of some recent advances and open problems, Automatica 39 (2003) 1667–1694.
[62] F. Monteghetti, G. Haine, D. Matignon, Stability of linear fractional differential equations with delays: a coupled parabolic–hyperbolic PDEs formulation, in: 20th World Congress of the International Federation of Automatic Control (IFAC), 2017.
[63] F.Q. Hu, M. Hussaini, P. Rasetarinera, An analysis of the discontinuous Galerkin method for wave propagation problems, J. Comput. Phys. 151 (1999) 921–946.
[64] M. Zennaro, Natural continuous extensions of Runge–Kutta methods, Math. Comput. 46 (1986) 119–133.
[65] A. Ern, J.-L. Guermond, Theory and Practice of Finite Elements, Springer-Verlag, New York, 2004.
[66] D.A. Di Pietro, A. Ern, Mathematical Aspects of Discontinuous Galerkin Methods, Springer-Verlag, Berlin, Heidelberg, 2012.
[67] A. Ern, J.L. Guermond, Discontinuous Galerkin methods for Friedrichs' systems. I. General theory, SIAM J. Numer. Anal. 44 (2006) 753–778.
[68] H. Brezis, Functional Analysis, Sobolev Spaces and Partial Differential Equations, Springer, New York, 2011.
[69] J.S. Hesthaven, T. Warburton, Nodal Discontinuous Galerkin Methods: Algorithms, Analysis, and Applications, Springer, New York, 2008.
[70] E.F. Toro, Riemann Solvers and Numerical Methods for Fluid Dynamics, third ed., Springer-Verlag, Berlin, Heidelberg, 2009.
[71] T. Toulorge, W. Desmet, Optimal Runge–Kutta schemes for discontinuous Galerkin space discretizations applied to wave propagation problems, J. Comput. Phys. 231 (2012) 2067–2091.
[72] J. Primus, E. Piot, F. Simon, M.G. Jones, W.R. Watson, ONERA–NASA cooperative effort on liner impedance eduction, in: 19th AIAA/CEAS Aeroacoustics Conference, Berlin, Germany, 2013, AIAA Paper 2013-2273.
[73] D. Marx, Y. Aurégan, Effect of turbulent eddy viscosity on the unstable surface mode above an acoustic liner, J. Sound Vib. 332 (2013) 3803–3820.
[74] M.O. Burak, M. Billson, L.-E. Eriksson, S. Baralon, Validation of a time-and frequency-domain grazing flow acoustic liner model, AIAA J. 47 (2009) 1841–1848.
[75] D. Levy, E. Tadmor, From semidiscrete to fully discrete: stability of Runge–Kutta schemes by the energy method, SIAM Rev. 40 (1998) 40–73.
[76] G. Cohen, S. Pernet, Finite Element and Discontinuous Galerkin Methods for Transient Wave Equations, Springer, Dordrecht, 2017.